



10TH International Conference on Sustainable Energy and Environmental Protection:

Materials

(June 27TH - 30TH, 2017, Bled, Slovenia)

(Conference Proceedings)

Editors:

Emeritus Prof. dr. Jurij Krope
Prof. dr. Abdul Ghani Olabi
Prof. dr. Darko Goričanec
Prof. dr. Stanislav Božičnik



University of Maribor Press



University of Maribor Press



University of Maribor Press

10TH International Conference on Sustainable Energy and Environmental Protection

Materials

(June 27TH – 30TH, 2017, Bled, Slovenia)

(Conference Proceedings)

Editors:

Emeritus Prof. dr. Jurij Krope

Prof. dr. Abdul Ghani Olabi

Prof. dr. Darko Goričanec

Prof. dr. Stanislav Božičnik

June 2017

- Title:** 10TH International Conference on Sustainable Energy and Environmental Protection (June 27TH – 30TH, 2017, Bled, Slovenia) (Conference Proceedings)
- Subtitle:** Materials
- Editors:** Emeritus Prof. Jurij Kroppe, Ph.D. (University of Maribor, Slovenia), Prof. Abdul Ghani Olabi, Ph.D. (University of the West of Scotland, UK), Asso. Prof. Darko Goričanec, Ph.D. (University of Maribor, Slovenia), Asso. Prof. Stanislav Božičnik (University of Maribor, Slovenia).
- Review:** Prof. Željko Knez, Ph.D. (University of Maribor, Slovenia), Prof. Niko Samec, Ph.D. (University of Maribor, Slovenia).
- Technical editors :** Jan Perša (University of Maribor Press), Armin Turanović (University of Maribor Press).
- Design and layout:** University of Maribor Press
- Conference:** 10TH International Conference on Sustainable Energy and Environmental Protection
- Honorary Committee:** Abdul Ghani Olabi, Ph.D. (Honorary President, University of the West of Scotland, United Kingdom), Igor Tičar, Ph.D (Rector of the University of Maribor, Slovenia), Niko Samec Ph.D. (Pro-rector of University of Maribor, Slovenia), Zdravko Kravanja, Ph.D. (Dean of the Faculty of Chemistry and Chemical Engineering, University of Maribor, Slovenia).
- Organising Committee:** Jurij Kroppe, Ph.D. (University of Maribor, Slovenia), Darko Goričanec, Ph.D. (University of Maribor, Slovenia), Stane Božičnik, Ph.D. (University of Maribor, Slovenia), Peter Trop, Ph.D. (University of Maribor, Slovenia), Danijela Urbanč, Ph.D. (University of Maribor, Slovenia), Sonja Roj (University of Maribor, Slovenia), Željko Knez, Ph.D. (University of Maribor, Slovenia), Bojan Štumberger, Ph.D. (University of Maribor, Slovenia), Franci Čuš, Ph.D. (University of Maribor, Slovenia), Miloš Bogataj, Ph.D. (University of Maribor, Slovenia), Janez Žlak, Ph.D (Mine Trbovlje Hrustnik, Slovenia), LL. M. Tina Žagar (Ministry of Economic Development and Technology), Igor Ivanovski, MSc. (IVD Maribor, Slovenia), Nuša Hojnik, Ph.D. (Health Center Maribor).
- Programme Committee:** Prof. Abdul Ghani Olabi (UK), Emeritus Prof. Jurij Kroppe (Slovenia), Prof. Henrik Lund (Denmark), Prof. Brian Norton (Ireland), Prof. Noam Lior (USA), Prof. Zdravko Kravanja (Slovenia), Prof. Jiri Jaromir Klemes (Hungary), Prof. Stane Božičnik (Slovenia), Prof. Bojan Štumberger (Slovenia), Prof. Soteris Kalogirou (Cyprus), Prof. Stefano Cordiner (Italy), Prof. Jinyue Yan (Sweden), Prof. Umberto Desideri (Italy), Prof. M.S.J. Hashmi (Ireland), Prof. Michele Dassisti (Italy), Prof. Michele Gambino (Italy), Prof. S. Orhan Akansu (Turkey), Dr. David Timoney (Ireland), Prof. David Kennedy (Ireland), Prof. Bekir Sami Yilbas (Saudi Arabia), Dr. Brid Quilty (Ireland), Prof. B. AbuHijleh (UAE), Prof. Vincenc Butala (Slovenia), Prof. Jim McGovern (Ireland), Prof. Socrates Kaplanis (Greece), Dr. Hussam Jouhara (UK), Prof. Igor Tičar (Slovenia), Prof. Darko Goričanec (Slovenia), Dr. Joseph Stokes (Ireland), Prof. Antonio Valero (Spain), Prof. Aristide F. Massardo (Italy), Prof. Ashwani Gupta (USA), Dr. Aoife Foley (UK), Dr. Athanasios Megartīs (UK), Prof. Francesco Di Maria (Italy), Prof. George Tsatsaronis (Germany), Prof. Luis M. Serra (Spain), Prof. Savvas Tassou (UK), Prof. Luigi Alloca (Italy), Prof. Faek Diko (Germany), Dr. F. Al-Mansour (Slovenia), Dr. Artur Grunwald (Germany), Dr. Peter Trop (Slovenia), Prof. Philippe Knauth (France), Prof. Paul Borza (Romania), Prof. Roy Douglas (UK), Prof. Dieter Meissner (Austria), Dr. Danijela Urbanč (Slovenia), Prof. Daniel Favrat (Switzerland), Prof. Erik Dahlquist (Sweden), Prof. Eric Leonhardt (USA), Prof. GianLuca Rospi (Italy), Prof. Giuseppe Casalino (Italy), Prof. J. Dawson (USA), Dr. José Simoes (Portugal), Prof. Kadir Aydin (Turkey), Dr. Khaled Benyounis (Ireland), Prof. Laszlo Garbai (Hungary), Prof. Mariano Martin (Spain), Prof. Masahiro Ishida (Japan), Prof. Michael Seal (USA), Prof. Marco Spinedi (Italy), Prof. Michio Kitano (Japan), Prof. Milovan Jotanović (BiH), Prof. Nafiz Kahraman (Turkey), Prof. Na Zhang (China), Prof. Naotake Fujita (Japan), Prof. Niko Samec (Slovenia), Prof. Oleksandr Zaporozhets (Ukraine), Prof. Osama Al-Hawaj (Kuwait), Prof. Petar Varbanov (Hungary), Prof. Peter Goethals (Belgium), Prof. Qi Zhang (China), Prof. Rik Baert (The Netherlands), Prof. Rolf Ritz (USA), Dr. Stephen Glover (UK), Prof. Signe Kjelstrup (Norway), Dr. Sumsun Naheer (UK), Prof. Sven Andersson (Sweden), Dr. Salah Ibrahim (UK), Prof. Sebahattin Unalan (Turkey), Prof. Sabah Abdul-Wahab Sulaiman (Oman), Prof. Somrat Kerdsuwan (Thailand), Prof. T. Hikmet Karakoç (Turkey), Prof. Tahir Yavuz (Turkey), Prof. Hon Loong Lam (Thailand), LL.M. Tina Žagar (Slovenia), Prof. A.M.Hamoda (Qatar), Prof. Gu Hongchen (China), Prof. Haşmet Turkoglu (Turkey), Dr. Hussam Achour (Ireland), Dr. James Carton (Ireland), Dr. Eivind Johannes (Norway), Prof. Elvis Ahmetović (BiH), Prof.

D.G.Simeonov (Bulgaria), Prof. Abdelakder Outzourhit (Morocco), Prof. Bilge Albayrak Çeper (Turkey), Prof. Bekir Zühtü Uysal (Turkey), Prof. D. Bradley (UK), Dr. Silvia Tedesco (UK), Dr. Valentin Ivanov (Germany), Dr. Vincent Lawlor (Austria), Prof. Yonghua Cheng (Belgium), Prof. Yasufumi Yoshimoto (Japan), Prof. Yahya Erkan Akansu (Turkey), Prof. Yunus Ali Çengel (Turkey), Prof. Zeljko Knez (Slovenia), Prof. Zoltan Magyar (Hungary), Dr. William Smith (Ireland), Dr. Abed Alaswad (UK).

First published in 2017 by
University of Maribor Press
Slomškovo trg 15, 2000 Maribor, Slovenia
tel. +386 2 250 42 42, fax +386 2 252 32 45
<http://press.um.si>, zalozba@um.si

Co-published by
University of Maribor, Faculty of Chemistry and Chemical Engineering
Smetanova ulica 17, 2000 Maribor, Slovenia
tel. +386 (0)2 22 94 400, faks + 386 (0)2 25 27 774
<http://www.fkkt.um.si>, fkkt@um.si

Published: 5. July 2017

© University of Maribor Press

All rights reserved. No part of this book may be reprinted or reproduced or utilized in any form or by any electronic, mechanical, or other means, now known or hereafter invented, including photocopying and recording, or in any information storage or retrieval system, without permission in writing from the publisher.

CIP - Kataložni zapis o publikaciji
Univerzitetna knjižnica Maribor

54:620.1(082)(0.034.2)

INTERNATIONAL Conference on Sustainable Energy and Environmental Protection (10 ; 2017 ; Bled)

Materials [Elektronski vir] : (Conference proceedings) / 10th International Conference on Sustainable Energy and Environmental Protection, (June 27th-30th, 2017, Bled, Slovenia) ; [organised by] University of Maribor [and] University of the West of Scotland ; editors Jurij Krope ... [et al.]. - El. zbornik. - Maribor : University of Maribor Press, 2017

Način dostopa (URL): <http://press.um.si/index.php/ump/catalog/book/247>

ISBN 978-961-286-056-1 (pdf)

doi: 10.18690/978-961-286-056-1

1. Gl. stv. nasl. 2. Krope, Jurij 3. Univerza (Maribor)

COBISS.SI-ID [92431617](https://nbn-resolving.org/urn:nbn:si:coibis-92431617)

ISBN 978-961-286-056-1

DOI: <https://doi.org/10.18690/978-961-286-056-1>

Price: Free copy

For publisher: Prof. Igor Tičar, Ph.D., rector (University of Maribor)

Preface

The 10th International Conference on Sustainable Energy and environmental Protection – SEEP 2017 was organised on June 27th – 30th 2017 in Bled, Slovenia, by:

- Faculty of Chemistry and Chemical Engineering, University of Maribor, Slovenia,
- University of the West of Scotland, School of Engineering and

The aim of SEEP2017 is to bring together the researches within the field of sustainable energy and environmental protection from all over the world.

The contributed papers are grouped in 18 sessions in order to provide access to readers out of 300 contributions prepared by authors from 52 countries.

We thank the distinguished plenary and keynote speakers and chairs who have kindly consented to participate at this conference. We are also grateful to all the authors for their papers and to all committee members.

We believe that scientific results and professional debates shall not only be an incentive for development, but also for making new friendships and possible future scientific development projects.

General chair
Emeritus Prof. dr. Jurij Krope



Plenary Talk on The Relation between Renewable Energy and Circular Economy

ABDUL GHANI OLABI - BIBLIOGRAPHY



Prof Olabi is director and founding member of the Institute of Engineering and Energy Technologies (www.uws.ac.uk/ieet) at the University of the West of Scotland. He received his M.Eng and Ph.D. from Dublin City University, since 1984 he worked at SSRC, HIAST, CNR, CRF, DCU and UWS. Prof Olabi has supervised postgraduate research students (10 M.Eng and 30PhD) to successful completion. Prof Olabi has edited 12 proceedings, and has published more than 135 papers in peer-reviewed international journals and about 135 papers in international conferences, in addition to 30 book chapters. In the last 12 months Prof Olabi has patented 2 innovative projects. Prof Olabi is the founder of the International Conference on Sustainable Energy and Environmental Protection SEEP, www.seepconference.co.uk

He is the Subject Editor of the Elsevier Energy Journal <https://www.journals.elsevier.com/energy/editorial-board/abdul-ghani-olabi>, also Subject editor of the Reference Module in Materials Science and Materials Engineering <http://scitechconnect.elsevier.com/reference-module-material-science/> and board member of a few other journals. Prof Olabi has coordinated different National, EU and International Projects. He has produced different reports to the Irish Gov. regarding: Hydrogen and Fuel Cells and Solar Energy.

CORRESPONDENCE ADDRESS: Abdul Ghani Olabi, Ph.D., Professor, University of the West of Scotland, School of Engineering and Computing, D163a, McLachlan Building, Paisley, United Kingdom, e-mail: Abdul.Olabi@uws.ac.uk.

<https://doi.org/10.18690/978-961-286-056-1> ISBN 978-961-286-056-1
© 2017 University of Maribor Press
Available at: <http://press.um.si>.

Plenary Talk on Energy Footprints Reduction and Virtual Footprints Interactions

JIRÍ JAROMÍR KLEMEŠ & PETAR SABEV VARBANOV

Increasing efforts and resources have been devoted to research during environmental studies, including the assessment of various harmful impacts from industrial, civic, business, transportation and other economy activities. Environmental impacts are usually quantified through Life Cycle Assessment (LCA). In recent years, footprints have emerged as efficient and useful indicators to use within LCA. The footprint assessment techniques has provided a set of tools enabling the evaluation of Greenhouse Gas (GHG) – including CO₂, emissions and the corresponding effective flows on the world scale. From all such indicators, the energy footprint represents the area of forest that would be required to absorb the GHG emissions resulting from the energy consumption required for a certain activity, excluding the proportion absorbed by the oceans, and the area occupied by hydroelectric dams and reservoirs for hydropower.

An overview of the virtual GHG flow trends in the international trade, associating the GHG and water footprints with the consumption of goods and services is performed. Several important indications have been obtained: (a) There are significant GHG gaps between producer's and consumer's emissions – US and EU have high absolute net imports GHG budget. (b) China is an exporting country and increasingly carries a load of GHG emission and virtual water export associated with consumption in the relevant importing countries. (c) International trade can reduce global environmental pressure by redirecting import to products produced with lower intensity of GHG emissions and lower water footprints, or producing them domestically.

To develop self-sufficient regions based on more efficient processes by combining neighbouring countries can be a promising development. A future direction should be focused on two main areas: (1) To provide the self-sufficient regions based on more efficient processes by combining production of surrounding countries. (2) To develop the shared mechanism and market share of virtual carbon between trading partners regionally and internationally.

CORRESPONDENCE ADDRESS: Jiří Jaromír Klemeš, DSc, Professor, Brno University of Technology - VUT Brno, Faculty of Mechanical Engineering, NETME Centre, Sustainable Process Integration Laboratory – SPIL, Technická 2896/2, 616 69 Brno, Czech Republic, e-mail: klemes@fme.vutbr.cz. Petar Sabeв Varbanov, Ph.D., Associate Professor, Brno University of Technology - VUT Brno, Faculty of Mechanical Engineering, NETME Centre, Sustainable Process Integration Laboratory – SPIL, Technická 2896/2, 616 69 Brno, Czech Republic, e-mail: varbanov@fme.vutbr.cz.

JIŘÍ JAROMÍR KLEMEŠ - BIBLIOGRAPHY



Head of “Sustainable Process Integration Laboratory – SPIL”, NETME Centre, Faculty of Mechanical Engineering, Brno University of Technology - VUT Brno, Czech Republic and Emeritus Professor at “Centre for Process Systems Engineering and Sustainability”, Pázmány Péter Catholic University, Budapest, Hungary.

Previously the Project Director, Senior Project Officer and Hon Reader at Department of Process Integration at UMIST, The University of Manchester and University of Edinburgh, UK. Founder and a long term Head of the Centre for Process Integration and Intensification – CPI2, University of Pannonia, Veszprém, Hungary. Awarded by the EC with Marie Curies Chair of Excellence (EXC). Track record of managing and coordinating 91 major EC, NATO and UK Know-How projects. Research funding attracted over 21 M€.

Co-Editor-in-Chief of Journal of Cleaner Production (IF=4.959). The founder and President for 20 y of PRES (Process Integration for Energy Saving and Pollution Reduction) conferences. Chairperson of CAPE Working Party of EFCE, a member of WP on Process Intensification and of the EFCE Sustainability platform.

He authored nearly 400 papers, h-index 40. A number of books published by McGraw-Hill; Woodhead; Elsevier; Ashgate Publishing Cambridge; Springer; WILEY-VCH; Taylor & Francis).

Several times Distinguished Visiting Professor for Universiti Teknologi Malaysia, Xi’an Jiaotong University; South China University of Technology, Guangzhou; Tianjin University in China; University of Maribor, Slovenia; University Technology Petronas, Malaysia; Brno University of Technology and the Russian Mendeleev University of Chemical Technology, Moscow. Doctor Honoris Causa of Kharkiv National University “Kharkiv Polytechnic Institute” in Ukraine, the University of Maribor in Slovenia, University POLITEHNICA Bucharest, Romania. “Honorary Doctor of Engineering Universiti Teknologi Malaysia”, “Honorary Membership of Czech Society of Chemical Engineering”, “European Federation of Chemical Engineering (EFCE) Life-Time Achievements Award” and “Pro Universitaire Pannonica” Gold Medal.

CORRESPONDENCE ADDRESS: Jiří Jaromír Klemeš, DSc, Professor, Brno University of Technology - VUT Brno, Faculty of Mechanical Engineering, NETME Centre, Sustainable Process Integration Laboratory – SPIL, Technická 2896/2, 616 69 Brno, Czech Republic, e-mail: klemes@fme.vutbr.cz.

Plenary Talk on Renewable energy sources for environmental protection

HAKAN SERHAD SOYHAN

Development in energy sector, technological advancements, production and consumption amounts in the countries and environmental awareness give shape to industry of energy. When the dependency is taken into account in terms of natural resources and energy, there are many risks for countries having no fossil energy sources. Renewable and clean sources of energy and optimal use of these resources minimize environmental impacts, produce minimum secondary wastes and are sustainable based on current and future economic and social societal needs. Sun is one of the main energy sources in recent years. Light and heat of sun are used in many ways to renewable energy. Other commonly used are biomass and wind energy. To be able to use these sources efficiently national energy and natural resources policies should be evaluated together with the global developments and they should be compatible with technological improvements. Strategic plans with regard to energy are needed more intensively and they must be in the qualification of a road map, taking into account the developments related to natural resources and energy, its specific needs and defining the sources owned by countries. In this presentation, the role of supply security was evaluated in term of energy policies. In this talk, new technologies in renewable energy production will be shown and the importance of supply security in strategic energy plan will be explained.

CORRESPONDENCE ADDRESS: Hakan Serhad Soyhan, Ph.D., Professor, Sakarya University, Engineering Faculty, Esentepe Campus, M7 Building, 54187 - Esentepe /Sakarya, Turkey, e-mail: hsoyhan@sakarya.edu.tr.

<https://doi.org/10.18690/978-961-286-056-1> ISBN 978-961-286-056-1
© 2017 University of Maribor Press
Available at: <http://press.um.si>.

HAKAN SERHAD SOYHAN - BIBLIOGRAPHY



Professor at Sakarya University, Engineering Faculty. 50 % for teaching and the rest for research activities.

Teaching, courses taught:

Graduate courses:

- Combustion technology;
- Modelling techniques;

Undergraduate courses:

- Combustion techniques;
- Internal combustion engines;
- Fire safety.

Technical skills and competences professional societies:

- 25 journal papers in SCI Index. 23 conference papers;
- Editor at FCE journal. Co-editor at J of Sakarya University;
- Head of Local Energy Research Society (YETA);
- Member of American Society of Mechanical Engineers (ASME);
- Member of Turkish Society of Mechanical Engineers (TSME).

CORRESPONDENCE ADDRESS: Hakan Serhad Soyhan, Ph.D., Professor, Sakarya University, Engineering Faculty, Esentepe Campus, M7 Building, 54187 - Esentepe /Sakarya, Turkey, e-mail: hsoyhan@sakarya.edu.tr.

<https://doi.org/10.18690/978-961-286-056-1> ISBN 978-961-286-056-1

© 2017 University of Maribor Press

Available at: <http://press.um.si>.

Table of Contents

CONFERENCE PROCEEDINGS

Comparison of Building Materials for Low-Rise Buildings Based on Environmental Footprint Maja Žigart, Rebeka Lukman Kovačič, Miroslav Premrov & Vesna Žegarac Leskovar	1
Low Energy Processing of Polymeric Materials Maša Knez Hrnčič, Gregor Kravanja & Željko Knez	13
Perspective $Ba_{0.5}Zr_{0.3}Ln_{0.2}O_{3-\Delta}$ ($Ln = Y, Dy, Sm$ and Nd) Proton-Conducting Electrolytes for Solid Oxide Fuel Cells Julia Lyagaeva, Elena Pikalova, Nikolai Danilov, Dmitry Medvedev, Anatoly Demin & Panagiotis Tsiakaras	23
Methanol an Energy Source Production by Reduction of CO₂ Under Visible Light Irradiation Using Fe₂O₃/TiO₂ Nanotube Immobilized Activated Carbon Fiber Ajit Sharma & Byeong-Kyu Lee	35
Energy Efficient Poly(Lactide) Obtaining by Microwave Synthesis Ivan Ristić, Milovan Jotanović, Tamara Erceg, Ljubiša Nikolić, Suzana Cakić, Vladan Mičić & Stefan Pavlović	43
A Candidate Material for Mercury Control in Energy Production Processes: Carbon Foams Loaded with Gold Cristina Antuña-Nieto, Elena Rodríguez, M. Antonia López-Antón, Roberto García & M. Rosa Martínez-Tarazona	51
Carbon-Based Sorbents Impregnated with Iron Oxides for Removing Mercury in Energy Generation Processes Jaime Trobajo, Elena Rodríguez, Roberto García, M. Antonia López-Antón & M. Rosa Martínez-Tarazona	59
Facile Fabrication of a Mesoporous Iridium Oxide Film for Efficient Electrocatalytic Water Oxidation Debraj Chandra, Tsubasa Sato, Ryouchi Takeuchi, Dong Li, Kenji Saito, Tatsuto Yui & Masayuki Yagi	69

Spray Pyrolysis Synthesis of Mesoporous γ-Alumina Supported Metal and Metal Phosphide Catalysts and Their Catalytic Activity	77
Jinsoo Kim, Kyungmin Im, Jae Hyung Choi, Hoang Vu Ly, Seung-Soo Kim, Chul-Woo Nam, Sung-Don Kim & Hyung-Kyu Park	
Gear Body Structure Design to Lower Vibration Emission	87
Riad Ramadani, Aleš Belšak, Marko Kegl, Jožef Predan & Stanislav Pehan	
Energy Saving Novel Lubricants	101
Darko Lovrec & Vito Tič	

Comparison of Building Materials for Low-Rise Buildings Based on Environmental Footprint

MAJA ŽIGART, REBEKA LUKMAN KOVAČIČ, MIROSLAV PREMROV & VESNA ŽEGARAC
LESKOVAR

Abstract The selection of the building materials has a high impact on production, operational and end of life phase of the building lifecycle and plays an important role in the design of sustainable buildings. The paper presents the environmental impact comparison of four different building construction systems widely used for the construction of energy efficient houses: reinforced concrete, brick, cross-laminated timber and timber-frame panel construction. The basic properties of building elements were determined according to the thermal transmittance equivalent. The analysis of structural elements carried out with the “Baubook construction calculator” revealed the environmental impacts of the individual materials and consequently of particular construction systems. Based on the comparison of selected elements the study draws attention to the critical materials and proposes some additional analyses on order to enable the preparation of general guidelines for the reduction of environmental impacts for sustainable low-rise buildings.

Keywords: • building materials • environmental impact • global warming potential • acidification potential • primary energy •

CORRESPONDENCE ADDRESS: Maja Žigart, Assistant, University of Maribor, Faculty of Civil Engineering, Transportation Engineering and Architecture, Smetanova ulica 17, 2000 Maribor, Slovenia, e-mail: maja.zigart@um.si. Rebeka Lukman Kovačič, Ph.D., Assistant Professor, University of Maribor, Faculty of Energy Technology, Slovenia, e-mail: rebeka.lukman@um.si. Miroslav Premrov, Ph.D., Professor, University of Maribor, Faculty of Civil Engineering, Transportation Engineering and Architecture, Smetanova ulica 17, 2000 Maribor, Slovenia, e-mail: miroslav.premrov@um.si. Vesna Žegarac Leskovar, Ph.D., Associate Professor, University of Maribor, Faculty of Civil Engineering, Transportation Engineering and Architecture, Smetanova ulica 17, 2000 Maribor, Slovenia, e-mail: vesna.zegarac@um.si.

1 Introduction

The European Commission has set a long-term goal of reducing energy use and greenhouse gas (GHG) emissions. In 2014, greenhouse gas emissions in the EU-28 were down by 22.9 % compared with 1990 levels, representing an absolute reduction of 1.136 billion tonnes of CO₂-equivalents [1]. The low-carbon economy roadmap for year 2050 suggests that EU should cut greenhouse gas emissions to 80% below 1990 levels by 2050, whereby the building sector only (housing and office buildings) should contribute to at least 90% of reduction [2]. For the accomplishment of the above stated objectives the new strategies for reduction of environmental impacts caused by buildings should be considered carefully.

The energy use during the building life cycle is apportioned over several phases, including construction, operation, maintenance and demolition phase. Adalberth [3] concluded in his study that for buildings constructed in temperate or cold regions, the major part of the life-cycle energy is used in the operation phase of the building. However, with the development of the improved building thermal envelope, heat recovery ventilation systems, energy-efficient lighting and electrical appliances, the buildings operational energy use and emissions can be reduced to a minimum. The study of Blengini & Di Carlo [4] addresses the significance of considering all of the life cycle phases and also the subsystems in the design process of low-energy buildings. The study of Karimpour et al. [5] shows that when time value of carbon and emission reduction targets are taken into account, the percentage of embodied energy from total life cycle energy increases noticeably. Similar findings were also presented in the review paper Ibn-Mohammed et al. [6] where it was established as increasingly important to acknowledge the significance of embodied emissions if GHG emissions reduction strategies are considered. The analysis of the embodied emissions can serve as a genuine indicator of CO₂ emissions and could be used to evaluate environmental impacts of buildings. Bin Marsono & Balasbaneh [7] compared GWP for seven combinations of exterior and interior walls with various building construction materials for residential buildings in Malaysia, while Monteiro & Freire [8] compared alternative exterior walls of Portuguese single-family house with three impact assessment methods. Both of the studies compared the wall elements with the higher U-values for the buildings located in warmer climates.

Similar to [7, 8] the current study considers the embodied emissions and environmental impacts of the materials in the production phase and compares different types of building envelope elements with the same thermal transmittance suitable for the design of passive houses located in moderate and cold climates. From the structural viewpoint the analysed element types meet the load bearing requirements for low-rise buildings of smaller dimensions. The aim of the study is to help designers in preliminary decisions when selecting individual materials for sustainable low-rise buildings.

The paper is divided in four sections. In Section 1 the background and the objectives of the research work are presented. Section 2 explains the numerical methodology. In Section 3 the results of the study are discussed and analysed. The last section presents the

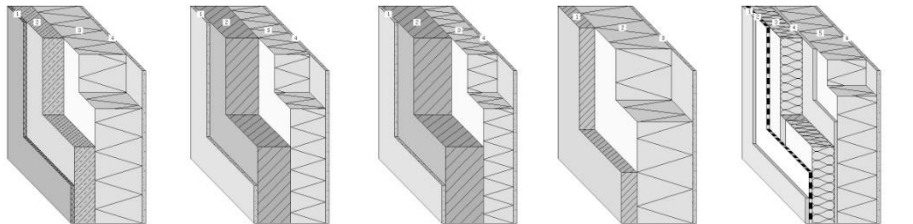
conclusions and applicability of the results to the design process of sustainable low-rise buildings.

2 Methodology

The current study is based on a comparison of four generally used building construction types suitable for the design of low-rise energy-efficient buildings located in Slovenia and other Central-European countries: reinforced concrete (RC), brick (B), cross-laminated timber (CLT) and timber-frame panel (TF) construction. Low-rise buildings are usually built using reinforced concrete bottom plate or linear foundations. In addition to the foundations, also the doors and windows can be the same in differently constructed buildings. Therefore, the major differences in construction materials occur within wall and roof elements, which are treated more specifically in this research. The analysed building wall and roof elements are designed for a modular box with dimensions of 6.5 x 6.5 x 3.0 m, but are tested as singular elements, which satisfy the load-bearing requirements for this type of model house. Different insulation layer thicknesses were selected in order to obtain the heat transfer coefficient $U = 0.10 \text{ W/m}^2\text{K}$ in all of the compared wall/roof cross-sections. The equal U-value of individual elements is selected on behalf of the intention to design the box models with similar energy-efficiency properties with operational energy use being almost equal for all compared cross-sections. The analysis was carried out with the “Baubook construction calculator” [9] on five wall sections and four flat roof sections of different construction types with the aim to compare the environmental impact of various element compositions. The functional unit used in analysis is 1 m² of wall / roof element.

2.1 The elements of the building thermal envelope under consideration

Five types of external wall elements are graphically presented and described in Figure 1. All of the analysed wall types consist of the main structural materials (timber, brick, concrete), insulation materials (rock wool façade insulation) and finishing (gypsum filler, plaster etc.). In the timber-frame panel we also use glass wool insulation with lower density in between the timber-frame structure and sheathing boards on both sides of the timber structure to ensure racking resistance of the wall elements. The brick construction is analysed in two variants, the first with brick of 30 cm width and the second in the width of 38 cm. Both blocks are widely used in the construction of energy-efficient low-rise buildings.

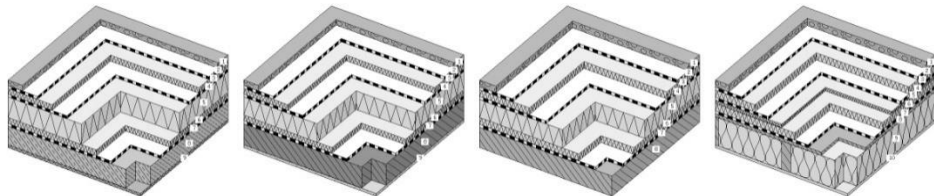


RC	B30	B38	CLT	TF
0.3 cm gypsum filler	1.5 cm lime cement finish plaster (1800 kg/m ³)	1.5 cm lime cement finish plaster (1800 kg/m ³)		1.5 cm gypsum plasterboard (900 kg/m ³) 0.18 cm polyethylene (PE) vapour brake
16 cm reinforced concrete (1% of reinforcement) (2300 kg/m ³)	30 cm vertically perforated brick + thin-bed mortar or glued using PUR (675 kg/m ³)	38 cm vertically perforated brick + thin-bed mortar or glued using PUR (675 kg/m ³)	9.5 cm cross-laminated timber, glued, external use (475 kg/m ³)	16 cm (13%) 8cm timber (475 kg/m ³) - rough, technically dried (87%) glass wool (18 kg/m ³) 1.5 cm gypsum plasterboard (900 kg/m ³)
36 cm rock wool (120 kg/m ³)	32 cm rock wool (120 kg/m ³)	30 cm rock wool (120 kg/m ³)	34 cm rock wool (120 kg/m ³)	25 cm rock wool (120 kg/m ³)
0.19 cm silicate plaster (without synthetic resin additive)	0.19 cm silicate plaster (without synthetic resin additive)	0.19 cm silicate plaster (without synthetic resin additive)	0.19 cm silicate plaster (without synthetic resin additive)	0.19 cm silicate plaster (without synthetic resin additive)

Figure 1. The comparison of the analysed wall elements composition

The thermal envelope composition of the flat roof elements is presented in Figure 2. The compared flat roof structures consist of main structural elements, waterproofing, thermal insulation and finalization. The thermal insulation used for the roof was expanded polystyrene insulation (EPS) with one inclined layer and extruded polystyrene insulation

(XPS) used as a thin protective layer on top of waterproofing layer. Additional glass wool insulation was also used in between the timber frame structure.



RC	B	CLT	TF
6 cm fillings made of sand, gravel, grit (1800 kg/m ³)	6 cm fillings made of sand, gravel, grit (1800 kg/m ³)	6 cm fillings made of sand, gravel, grit (1800 kg/m ³)	6 cm fillings made of sand, gravel, grit (1800 kg/m ³)
0.02 cm PP fleece	0.02 cm PP fleece	0.02 cm PP fleece	0.02 cm PP fleece
6 cm XPS-G 30 (32 kg/m ³)	6 cm XPS-G 30 (32 kg/m ³)	6cm XPS-G 30 (32 kg/m ³)	6 cm XPS-G 30 (32 kg/m ³)
0.78 cm polymer bitumen sealing sheeting	0.78 cm polymer bitumen sealing sheeting	0.78 cm polymer bitumen sealing sheeting	0.78 cm polymer bitumen sealing sheeting
22 cm EPS-W 25 (23 kg/m ³)	20 cm EPS-W 25 (23 kg/m ³)	16 cm EPS-W 25 (23 kg/m ³)	22 cm EPS-W 25 (23 kg/m ³)
6 cm EPS-W 25 (23 kg/m ³)	6 cm EPS-W 25 (23 kg/m ³)	6 cm EPS-W 25 (23 kg/m ³)	6 cm EPS-W 25 (23 kg/m ³)
0.18 cm polyethylene (PE) vapour brake	0.18 cm polyethylene (PE) vapour brake	0.18 cm polyethylene (PE) vapour brake	0.18 cm polyethylene (PE) vapour brake
20 cm reinforced concrete (1% of reinforcement) (2300 kg/m ³)	23 cm prefabricated brick ceiling elements (60/17) and 6 cm concrete plate	18.2 cm cross-laminated timber, glued, external use (475 kg/m ³ - e.g. spruce/fir)	24 cm (13%) 8 cm timber (475 kg/m ³ - e.g. spruce/fir) - rough, technically dried (87%) glass wool MW(GW)-W (18 kg/m ³)
0.3 cm gypsum filler	1.5 cm lime cement finish plaster (1800 kg/m ³)		1.5 cm gypsum plasterboard (900 kg/m ³)

Figure 2. The comparison of the analysed roof elements composition

2.2 Impact assessment categories

To evaluate the environmental performance of various construction elements the current analysis considers the primary energy content of all non-renewable resources (PENRT), the global warming potential (GWP100 total) and acidification potential (AP). The total energy resources required to produce a product or service are collectively referred to as the primary energy content (PE). The PE is specified in MJ and calculated from the lower calorific value of the energy resources deployed. The "PENRT" specifies the primary energy content of all non-renewable resources (crude oil, coal, etc.) including resources for energy-related as well as material uses. The indicator "GWP (total)" includes both the contribution to global warming in terms of greenhouse gas emissions and the quantities of carbon dioxide stored in the biomass. Factors are expressed as global warming potential for time horizon 100 years (GWP100), in kg carbon dioxide/kg emission, in accordance with CML 2001 v3.9. [9] Acidifying substances cause a wide range of impacts on soil, groundwater, surface water, organisms, ecosystems and materials, caused mainly by the interaction of nitrogen oxide (NO_x) and sulphur dioxide gases (SO₂) with other atmospheric constituents. Acidification Potential (AP) for emissions to air is calculated in accordance with CML 2001 v3.9, describing the fate and deposition of acidifying substances. AP is expressed as kg SO₂ equivalents / kg emission. [9], [10].

3 Results and Discussions

The individual environmental impact indicators for different wall types are presented in Figure 3.

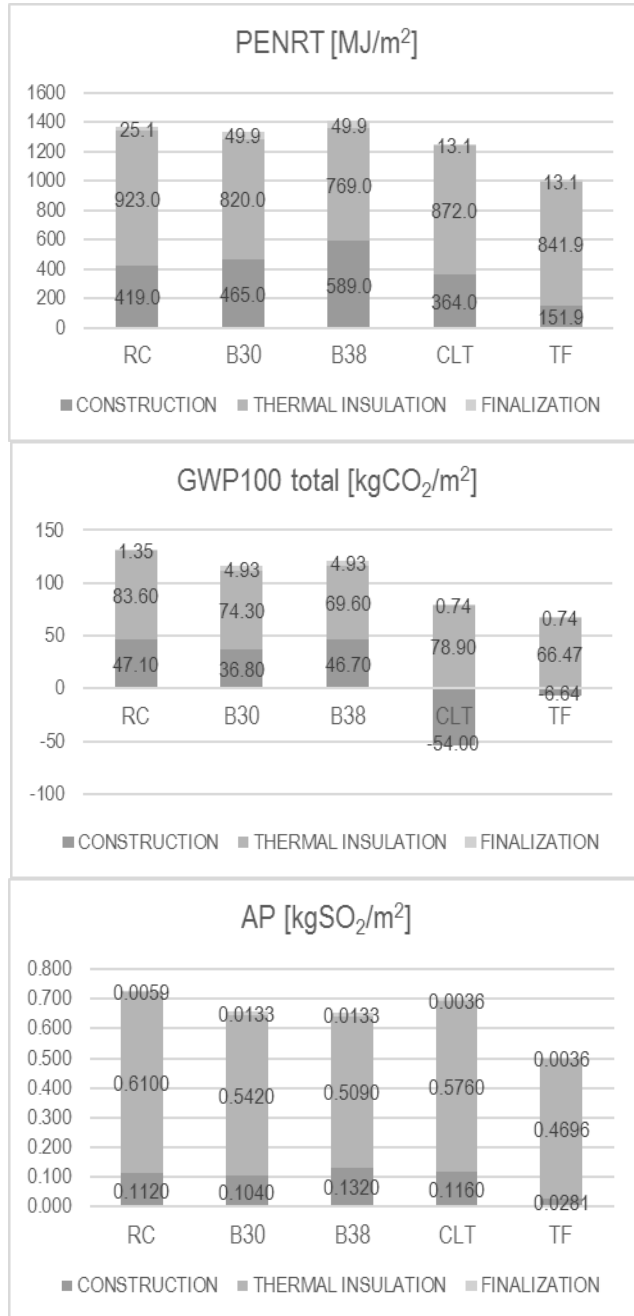


Figure 3. Comparison of environmental impact indicators for different wall sections

The analysis of different wall types taking into account three environmental impact assessment categories reveals that the chosen thermal insulation acts as the weakest material in all wall sections. The latter is especially important for elements with load-bearing material of weak thermal properties, for example reinforced concrete, where the required U-value has to be achieved on account of higher amount of insulation. The whole element composition in that case exhibits bad environmental performance, although the structural material itself is not very problematic from the environmental viewpoint.

Comparing the primary energy content of all non-renewable resources we can see the highest impact of 1408 MJ/m² for the wall with 38 cm brick, followed by the concrete wall composition with 1367 MJ/m². The PENRT decreases for B30 and CLT, while the best evaluation goes to the timber-frame wall composition with the primary energy content of non-renewable sources of 1007 MJ/m². For this wall type it is interesting that the insulation contributes more than 83% to the overall PENRT.

The biggest difference between the compared wall elements is in global warming potential where the timber structures, and especially the cross-laminated timber wall, are showing better environmental performance due to the quantities of carbon dioxide sequestered in the biomass. The CLT panel analysed in our study stores about 54 kg of CO₂ in 1 m² of element.

Regarding the acidification potential the timber-frame panel system exhibits the best assessment again with the AP value of 0.5013 kgSO₂/m². Surprisingly, the CLT system shows relatively high acidification potential of almost 0.70 kgSO₂/m², which is due to the adhesives used in the production process next to the high quantity of thermal insulation.

To understand the obtained results it is necessary to compare the amount and type of individual materials in each of the analysed wall sections. The biggest advantages of timber-frame panel system are, apart from the low thermal conductivity of timber, in the relatively small dimensions and consequently amounts of load bearing structure. Additionally, the possibility of usage of lower density insulation (glass wool) between the load-bearing timber structure contributes to better environmental performance of such element composition, since in comparison with denser rock wool, the glass wool exhibits distinctly better environmental properties [9]. For the heavyweight massive wall elements the volumetric share of structural material is around 30% for concrete and about 47-55% for brick wall, while for the lightweight timber walls this amount is much lower. The volumetric share of structural material in cross-laminated timber wall is 22% and for the timber-frame panel wall just around 12% (timber frame and sheathing boards), whereby the timber structural frame itself represents only a very small share of 5% if 1 m² of wall element is concerned. Additionally, the already mentioned requirements on specific thermal properties contribute the biggest input of negative environmental impacts in wall sections with structural materials of higher thermal conductivity (concrete).

The results for all of the analysed roof elements are presented in Figure 4.

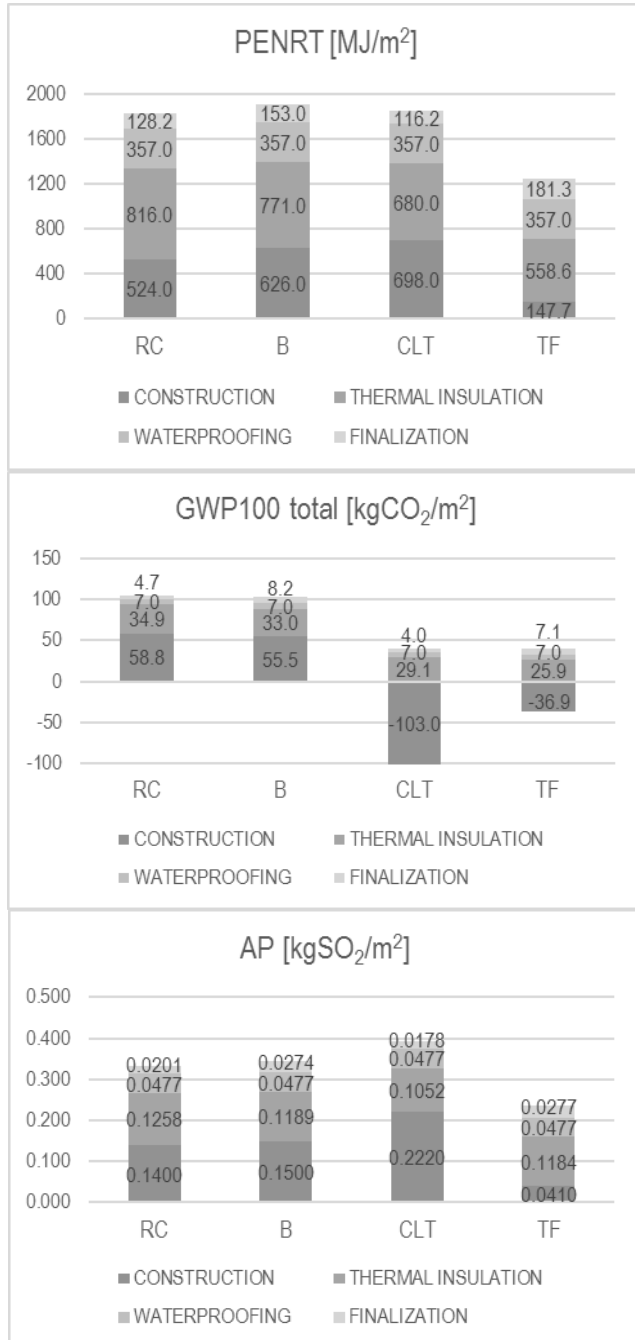


Figure 4. Comparison of environmental impact indicators for different roof sections

The environmental impacts are the lowest for the timber-frame roof construction in all assessment categories, except from the global warming potential category, where the CLT system shows the lowest impact on account of sequestered carbon. The amount of structural material is much higher in CLT roof elements (volumetric share of 34%) than in TF roof element (volumetric share of 6%) which influences positively on the assessment of global warming potential, but just opposite on the assessment of acidification potential. The prefabricated brick ceiling and reinforced concrete roof elements exhibit very similar results in all assessment categories, which is partly also due to the use of concrete in both mentioned roof structures. The observation of all roof elements shows the impact of polystyrene insulation is somewhat lower if compared to wall elements with rock wool insulation. However the impact of waterproofing materials is not negligible at all, especially in regard to very low quantity (1-2% volumetric share) of this material used in the roof compositions.

4 Conclusions

The analysis of the wall and roof elements constructed in different systems reveals the timber-frame construction has the best overall environmental performance. The second best is the cross-laminated timber system with the best performance in the assessment of global warming potential and slightly worse in acidification potential. The results are comparable to the study [7] which shows the timber walls having the lowest GWP for buildings in Malaysia. Also in the study [8] all three LCA methods indicated the timber wall system being the preferable solution with the lowest impacts for most categories, while the concrete and double walls with facing brick showed higher impacts.

However, our study shows that in all construction systems the type and quantity of insulation overtakes a large impact share. In that manner it would be beneficial to consider the use of alternative insulation materials of better environmental performance. Additional analyses of the construction elements composed with other insulation materials should be performed in the frames of further research. The differences between the individual construction systems might become smaller if better insulation materials were used.

It is also important to point out that the construction types undergone the current analysis have been designed for low-rise buildings with smaller spans between the supporting elements. For higher buildings with larger spans the thickness and quantities of structural load-bearing materials would change, therefore some additional analyses should be performed also in order to gather the results for different building geometries.

The results of this study draw attention to the critical materials and provide useful guidelines for designers, architects and developers with a range of options for the selection of a suitable building envelope on the basis of the environmental impact. Additional life-cycle studies are required to present the comparative results for house modules of various dimensions and material types.

Acknowledgements

The authors acknowledge the financial support from the Slovenian Research Agency (research core funding No. P2-0129).

References

- [1] European Commission, Eurostat, Greenhouse gas emission statistics. June 2016.
- [2] European Commission, "Energy Roadmap 2050", European Union, 2012.
- [3] Adalberth, K., "Energy use in four multi-family houses during their life cycle", *International Journal of Low Energy and Sustainable Buildings*, 2000, pp 1-22.
- [4] Blengini, G.A, Di Carlo, T., "The changing role of life cycle phases, subsystems and materials in the LCA of low energy buildings", *Energy and Buildings*, 2010, pp 869-880.
- [5] Karimpour, M., Belusko, M, Xing K., Bruno, F., "Minimising the life cycle energy of buildings: Review and analysis", *Building and Environment*, 2014, pp 106-114.
- [6] Ibn-Mohammed, T., Greenough, R., Taylor, S., Ozawa-Meida, L., Acquaye, A., "Operational vs. embodied emissions in buildings-A review of current trends", *Energy and Buildings*, 2013, pp 232-245.
- [7] Bin Marsono A.K, Balasbaneh, A.T., "Combinations of building construction material for residential building for the global warming mitigation for Malaysia", *Construction and Building Materials*, 2015. pp. 100-108.
- [8] Monteiro H., Freire F., "Life-cycle assessment of a house with alternative exterior walls: Comparison of three impact assessment methods", *Energy and Buildings*, 2012, pp 572-583.
- [9] "Baubook" - Die Datenbank für ökologisches Bauen & Sanieren, Energieinstitut Vorarlberg & Österreichische Institut für Baubiologie und -ökologie GmbH.
- [10] Guinée, J.B., Gorrée, M., Heijungs, R.; Huppes, G., Kleijn, R.; Koning, A. de; Oers, L. van, Wegener Sleswijk, A., Suh, S., Udo de Haes, H.A., Bruijn, H. de, Duin, R. van; Huijbregts, M.A.J. "Handbook on life cycle assessment." Operational guide to the ISO standards. I: LCA in perspective. IIa: Guide. IIb: Operational annex. III: Scientific background. Kluwer Academic Publishers, ISBN 1-4020-0228-9, Dordrecht, 2002, 692 pp

Low Energy Processing of Polymeric Materials

MAŠA KNEZ HRNČIČ, GREGOR KRAVANJA & ŽELJKO KNEZ

Abstract Traditional methods for solids processing involve either high temperatures, necessary for melting or viscosity reduction, or hazardous organic solvents known of their undesirable environmental and biological impact. Establishing new processing pathways featured by lower processing temperatures, omission of organic solvents and reduction of disposal is essential. Sustainable technologies are shifting industrial processes towards applying supercritical fluids for processing of polymeric materials. Beside water and carbon dioxide, noble gases have been demonstrated as a possible and a very suitable replacement of conventional solvents for greener processes with lower energy consumption. Properties of the obtained powder product like particle size, size distribution and morphology depend on phase equilibria and thermodynamic behavior of the system, fluid dynamics, mass transfer and nucleation-growth kinetic.

Different methods developed or modified by the authors of the present contribution were applied for determination of these parameters. Solubility and diffusivity of CO₂ and Ar in polyethylene glycol, diffusion coefficients, density and interfacial tension have been determined in the frame of our previous research.

Application of supercritical fluids in polymer particle formation and foaming processing are presented. PGSSTM (Particles from Gas-Saturated Solutions) is useful for production of polymer powder or entrapping of active ingredients in polymer matrices. Microcellular polymeric foams produced by depressurization in batch mode, using supercritical CO₂ as blowing agent, can provide significant environmental benefits.

Keywords: • polymer processing • solubility • interfacial tension • PGSSTM • low energy •

CORRESPONDENCE ADDRESS: Maša Knez Hrnčič, Ph.D., Assistant Professor, University of Maribor, Faculty of Chemistry and Chemical Engineering, Smetanova ulica 17, 2000 Maribor, Slovenia, e-mail: masa.knez@um.si. Gregor Kravanja, Assistant, University of Maribor, Faculty of Chemistry and Chemical Engineering, Smetanova ulica 17, 2000 Maribor, Slovenia, e-mail: gregor.kravanja@um.si. Željko Knez, Ph.D., Full Professor, University of Maribor, Faculty of Chemistry and Chemical Engineering, Smetanova ulica 17, 2000 Maribor, Slovenia, e-mail: zeljko.knez@um.si.

1 Introduction

Special combination of gas-like viscosity and diffusivity, and liquid-like density and solvating properties of a SCF makes them an excellent solvent for various applications [1]. The processes involving SCF are sustainable, environmentally friendly and cost efficient, and offer the possibility of obtaining new products. Solvent elimination and the recovery of final products are easy (no residue is left and a dry solid product is obtained, just by controlling the pressure), leading to processes with less energy consumption. Beneficial properties of high-pressure or supercritical CO₂ offer significant advantages, such that it has great potential to be utilized as a solvent for the processing of polymers. It is abundant, chemically inert and relatively inexpensive, as well as being non-toxic and non-flammable. In addition, at supercritical conditions CO₂ has been proven to influence the physical properties of micronized materials [2] and it can be easily removed from the product by depressurization since it is gaseous under atmospheric pressure. That means no solvent residues in the final product and consequently lower processing cost.

Supercritical fluids are already applied in several processes developed to the commercial scale. Supercritical CO₂ is overwhelmingly still the solvent of choice for high pressure operations. More than 90% of supercritical fluid extractions have been performed with CO₂ as supercritical solvent because of owing a great ability of easy penetration inside the materials and a high solvent power, but disadvantageously, its use is largely limited to the processing of dry raw materials and compounds of low polarity and low molecular weight. The diversity of polymer properties makes polymers such as cotton, wool, rubber, teflon, and all plastics widely applied in everyday life and also in industrial applications where natural and synthetic polymers with a wide range of stiffness, strength, heat resistance, density, and even varying price are produced. As mentioned above, low cost, low density, ease of processing are just some of the advantages of polymers which make them highly applicable. Several applications of polymeric materials have found its place in the field of energy. Functionalised polymers have been studied as potential material for the development of hydrogen storage in system as fuel sources for fuel cells. Main features of nanoporous polymers for H₂ storage are the light weight, contrarily to the metals, and the complete reversible adsorption-desorption mechanism without appreciable hysteresis [3]. In addition, commercial polymers can be easily modified in order to improve their intrinsic properties to store H₂ or to introduce compounds with these peculiarity. But there is also a disadvantage, poor mechanical properties, which also explains the fact that polymers are highly investigated also in the fields of scientific literature in order to moderate this disadvantage.

Absorption of compressed gas in polymer matrices results in a wide spectrum of possible applications in the field of sustainable polymer processing, for instance production of fibres, micro-particles and foams, polymer impregnation, separation of gas mixtures through polymer membranes, therefore investigation of thermodynamic properties of binary systems polymer/CO₂ is a topic under an intense research [4]. Due to unique properties of such systems, several modifications of polymers are taking place since CO₂ dissolution and polymer swelling can be expected. SCF addition reflects in modification

of several physical properties of polymer, such as glass transition temperature, melting temperature, surface tension, and viscosity, which are changed depending on solubility of SCF in the polymer.

Understanding behavior of different polymers in the presence of a gas in its supercritical state is crucial for establishing polymer processing techniques that use high-pressure or supercritical CO₂ as a solvent [5].

Despite supercritical fluids are already applied in several processes developed to the commercial scale; – from pharmacy, food sciences to the textile industry, there are certain hindrances concerning their wider application, especially in the field of energy, where the real potential of SCFs in the field of energy has still to be thoroughly studied and understood. Due to the environmental concerns related to their use, intensive research has focused on the development of systems with SCFs as refrigerants. SCFs, Their thermodynamical properties, especially of SC CO₂ have been studied for using supercritical CO₂ cycles instead of classical systems: the compression ratio is low, so compressor efficiency is relatively high; volumetric refrigeration capacity is high, which helps reducing the size of the systems. Capturing CO₂, generated from burning conventional fossil fuels, and storing it underground in supercritical state was proposed as a solution to the drastic increase in CO₂ emissions.

An efficient way of using CO₂ is by combining coal technology with crude oil recovery. In recent time, many novel technologies have been proposed and partially introduced for conversion of biomass to energy and chemicals. In addition to change of the phase equilibrium as a consequence of changing process condition; altering of phase diagram of the solvent there is a challenge of difficult prediction and design of process conditions; necessity for addition of organic solvents (called entrainers or cosolvents) to SCF in order to magnify solvent power and high investment cost due to the advanced equipment.

Knowledge about phase equilibria and reaction kinetics is essential to design a process with a well-considered union between economic feasibility and safety. Contributions reporting phase equilibria of systems with CO₂ are offered in particular in scientific literature. Data on thermodynamic and transport properties of systems containing different SCFs is still scarce. Research efforts are aimed to develop and optimize new, easier and quicker methods offering a possibility to determine fundamental data on thermodynamic properties of binary systems of polymers and different gases with a high potential to be used as sub- or supercritical solvents. Supercritical fluids can be used either as a solvent (RESS-Rapid expansion of supercritical solution), an antisolvent (GAS-Gas antisolvent crystallization) or a solute (PGSSTM-Particles from Gas-Saturated Solutions) in the processes of particle size reduction. Some of these applications already found applications in polymer processing branch. For the design of technologies using sub- or supercritical fluids process parameters, such as processing temperature and pressure, type and quantity of solvent, the recirculation rate and energy consumption are highly important. This information can be obtained from phase equilibrium and mass

transfer measurements and from the analysis of the solvent cycle in T - S (temperature – entropy) diagrams.

2 PGSSTM Micronisation Process Using Subcritical and Supercritical Fluids

Technically for batch wise operated PGSSTM plant, the substance to be micronized is filled in an autoclave, later the gas is loaded and the system is equilibrated (gas is solubilized in the substances or mixture of substances). The gas saturated system is expanded via a nozzle. In a continuous operated plant the substance to be powdered (molten or liquid, emulsion or suspension) is feed to static mixer, where it is mixed with sub-critical or super-critical fluid. After mixing the multicomponent system is expanded via nozzle.

Produced particles, which are of micron size, are easily separated from gas stream in a spray tower cyclone. The PGSSTM process could be used for production of particles of pure substances, but the main advantage of process is production of composites of miscible or even immiscible substances. In this way frozen emulsions or liquid filled particles could be produced. As mentioned before, PGSSTM process could operate batch wise or continuously and today several plants from the lab up to industrial scale are in use in different industry.

In PGSSTM process the polymer or the polymer mixture to be powdered must be converted into a sprayable form by liquefaction/dissolution in order to obtain a gas-containing solution which is than rapidly expanded in an expansion unit and the gas is evaporated. Owing to the Joule-Thomson effect and/or the evaporation and the volume-expansion of the gas, the solution cools down below the solidification temperature of the solute, and fine particles are formed. The solute is separated and fractionated from the gas stream by a cyclone and electro-filter.

In PGSSTM process the content of the gas in the heavy phase is of great importance for process design.

2.1 Phase equilibria

When the liquefaction is achieved by melting, the knowledge of the P - T trace of the S-L-V equilibrium curve gives information on the pressure needed to melt the substance to be micronized and form a liquid phase at a given temperature, and to calculate its composition [6, 7, 8].

When the supercritical fluid has a relatively high solubility in the molten heavy component, the S-L-V curve can have a negative dP/dT slope [9]. The second type of three-phase S-L-V curve shows a temperature minimum. In the third type, where the S-L-V curve has a positive dP/dT slope, the supercritical fluid is only slightly soluble in the molten heavy component, and therefore the increase of hydrostatic pressure will raise the

melting temperature and a new type of three-phase curve with a temperature minimum and maximum may occur [10].

In general, for substances for which the liquefaction is achieved by melting the systems with a negative dP/dT slope or with a temperature-minimum in the S-L-V curve could be processed by PGSSTM [7].

Applications of CO₂ in novel engineering concepts include the use of supercritical CO₂ as a swelling agent for polymers to help impregnate the carrier with desirable substances such as bioactive compounds, as well as using CO₂ as a compressed fluid to obtain different polymer morphologies of pure polymers or composites [11]. Apart from an inert nature and easily attainable supercritical conditions, gas-like diffusivity and liquid-like density in the supercritical phase allow replacing conventional, often noxious, solvents with supercritical CO₂. Dissolved CO₂ causes a considerable reduction in the viscosity of molten polymer, a very important property for the applications like polymer modification, formation of polymer composites, polymer blending, microcellular foaming, particle production and polymerization. Properties of the obtained powder product like particle size, size distribution and morphology depend on phase equilibria and thermodynamic behavior of the system, fluid dynamics, mass transfer and nucleation-growth kinetic. Phase equilibria and reaction kinetics, verification of process steps and design of process sequences to produce a product (energy) from raw materials are the main hindrances concerning SCF applications.

2.2 Economy of a micronization process

As mentioned above, in PGSSTM process the substance (polymer) to be powdered must be converted into sprayable form by liquefaction/dissolution. This can be achieved by melting or dissolving of the substance in liquid solvent followed by saturation of the melt or solution with gas, where the formation of fine droplets after spraying through a nozzle are driven by:

- reduced surface (interfacial) tension (mN/m)
- low viscosity (MPa s).

These two parameters crucially influence economy of a micronization process. Basis for scale up and cost estimation for an industrial production are related to the production capacity and depend on the annual hours of operation and the amount of CO₂ required to generate 1 kg of powder Weidner has considered an economic evaluation of PGSS micronization plant with a capacity of 1.5 tons per hour. The process is featured by low operating costs, as low as 0.20 € (around 0.3 USD), including investment, personal, consumables (incl. gas), maintenance and interest. Feasibility of a plant of that size it could be increased by installing a CO₂ recovery [12]. However, processing costs can increase up to 1.2 €/kg in case of short processing time and high GTF (gas, used as a solvent, to feed) ratios. Low GTF ratios contribute significantly to reduce processing costs. For a plant with capacity of 1500 kg/h, processing costs decrease from 1.2 €/kg to

0.4 €/kg at the same operation time. For a plant of the same capacity, extending processing time from 3000 hrs/year up to 8000 hrs/year can reduce operating cost for almost 50 %.

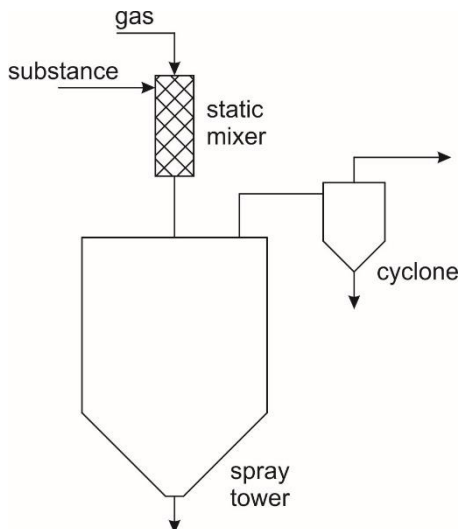


Figure 1. Basic scheme of continuous operated apparatus for PGSSTM micronisation [7].

The powders produced show narrow particle-size distributions, and have improved properties compared to the conventional produced powders [13].

The characteristics (properties) of the substance to be micronised (crystalline-amorphous, pure or composite), the process parameters (pre-expansion pressure, temperature, gas to substance ratio (GSR), viscosity of melt/solution/dispersion) of the PGSSTM process and geometry of the process equipment influence particle size, particle size distribution, bulk density, the morphology (particle shape) and ratios crystalline/amorphous of the processed substances.

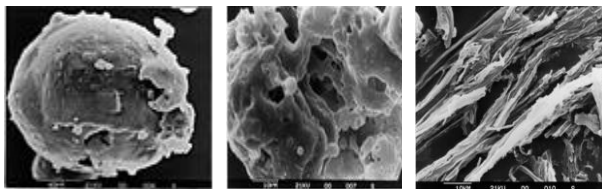


Figure 2. PGSSTM Particles of polyethyleneglycols with different morphology [7].

There are several advantages of PGSSTM process compared to HP crystallization, RESS and anti-solvent processes like moderate operating pressure and temperature, very low gas consumption, separation of formed solid particles from gas stream is easy, production of composites is possible, process could operate batch wise or continuously, scale up is relatively simple and low investment cost.

Disadvantage is that mostly particles of micron size and bigger could be produced, while production of submicron sized particles is nearly impossible.

Due to the low operating costs and low investment costs, the process is applied in different industries.

2.3 PGSS drying

Analysis of PGSS-drying process includes mass and energy balances, phase equilibrium conditions, mass transfer rates and mechanisms. A part of results, obtained in the frame of our research has already been published [11]. Furthermore, a global mass balance can be used to calculate the minimum gas/liquid flow ratio required for producing dry powder [7]. Some differences have been observed in concentration of moisture in powder obtained experimentally and calculated based on the mass balance and the phase equilibrium, which have been attributed to the kinetic factors not considered in mass balance calculations, i.e. the evolution of pressure and temperature along the expansion path. Furthermore a global energy balance was used for estimation of spray tower temperature as a function of pre-expansion conditions, and the results were in agreement with experimentally measured temperatures.

It has been proposed that atomization of the biphasic mixture leaving the static mixture occurs by two simultaneous processes: flash-boiling atomization and effervescent atomization. Based on this mechanism, variation of particle size with process conditions observed in experiments can be explained as a function of CO₂ concentration in the liquid phase: process conditions which cause an increase of CO₂ concentration in the liquid phase, promote a more efficient atomization and therefore a reduction of particle size.

2.4 Polymer and composite foaming with supercritical CO₂

The use of polymer and composite foams is extremely widespread. They found applications in automotive and aircraft industries, for military purposes, for household appliances and furniture, in sports and leisure products and in pharmaceutical and medical fields [4]. Foams are used as insulation materials, lightweight materials for automotive parts and packaging, supports for catalysts, membranes for chemical separations, scaffolds for tissue engineering, tissue regeneration, protein encapsulation and controlled release devices. The large number of applications is due to their properties, especially their high impact strength combined with light weight, which ensures foams a higher mechanical strength-to-weight ratio than other materials [13]. The term polymer composite refers to a material consisting of two immiscible phases of which one is a polymeric material and one is present as a dispersed phase [14]. By using a polymer matrix reinforced with filler (which may be another polymer, ceramic or metallic powder) one can obtain a new material with improved strength, toughness and plasticity, and in the case of biomaterials with better biological response than both base, homogeneous compounds. Moreover, by controlling the volume fractions and the distribution of the reinforcing phase, the properties and design of the composite material can be varied and

tailored to suit the required characteristics. Polymer composites, consisting of inorganic or organic materials incorporated into polymeric matrixes, are the subject of intensive research due to their increasing applications in paint, cosmetic, electronic, optical, mechanical and medical devices [15].

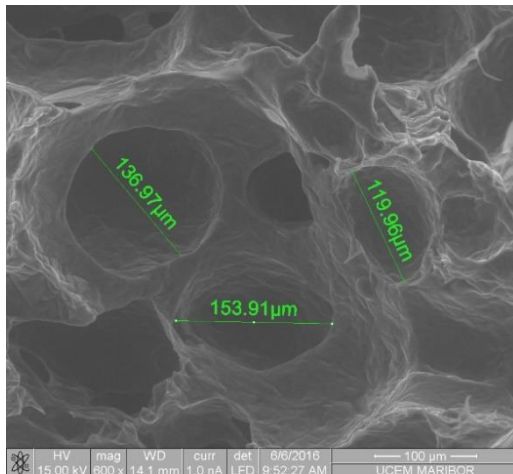


Figure 3. Foam of Brij52 [16].

2.5 Conclusions and outlook

Processing of polymers using sub-critical or super-critical fluid to obtain functional polymers is still subject of intensive research. Regarding industrial applications of supercritical fluids, it may be assumed that there are already several extraction plants on industrial scale in operation, but the number of micronisation units is relatively low.

There is certain time gap before research is converted to industrial application, and based on developments in area of high pressure extraction we could be sure that the number of high pressure micronisation units will increase in the near future.

Main advantage of the use of sub-critical or super-critical fluids for production of fine particles is the tunability of solvent properties.

The unique thermodynamics and fluid dynamic properties of subcritical or supercritical fluids can be used for formation of products with unique customer designed properties for the use in different applications.

Micronisation processes could be easily connected to subcritical or supercritical extraction processes, or to a downstream processing for products of chemical or biochemical synthesis in subcritical or supercritical fluids.

Use of CO₂ also prevents oxidation of products during processing steps, processing of substances using PGSSTM process could be performed even below their melting point.

Water is the cheapest solvent, but due to the high polarity, the use of water as recrystallization solvent is limited and therefore the second cheapest solvent with pressure and temperature unaltered properties is carbon dioxide. Beside the tunability of thermodynamic and fluid dynamic properties and low price of CO₂, CO₂ has also several other advantages [17]. Therefore we can be sure that advances in the field of micronisation and formulation processes using subcritical and supercritical fluids will in the near future open up new ways for substances produced at an industrial scale.

Acknowledgements

The authors would like to acknowledge Slovenian Research Agency (ARRS) for financing research in frame of Programme P2-0046 and current and previous coworkers in research groups in Maribor, Erlangen and Bochum.

References

- [1] Ž. Knez, E. Markočič, M. Leitgeb, M. Primožič, M. Knez Hrnčič and M. Škerget, Industrial applications of supercritical fluids: A review, *Energy*, vol. 77, issue C, pp. 235-243, 2014.
- [2] K. Wenelska, B. Michalkiewicz, X. Chen and E. Mijowska, Pd nanoparticles with tunable diameter deposited on carbon nanotubes with enhanced hydrogen storage capacity, *Energy*, vol. 75, pp. 549–554, Oct. 2014.
- [3] R. Pedicini, B. Schiavo, P. Rispoli, A. Saccà, A. Carbone, I. Gatto and E. Passalacqua, Progress in polymeric material for hydrogen storage application in middle conditions, *Energy*, vol. 64, pp. 607–614, Jan. 2014.
- [4] I. Tsivintzelis, G. Sanxaridou, E. Pavlidou and C. Panayiotou, Foaming of polymers with supercritical fluids: A thermodynamic investigation, *The Journal of Supercritical Fluids*, vol. 110, pp. 240–250, Aug. 2016.
- [5] P. W. Labuschagne, B. Naicker and L. Kalombo, Micronization, characterization and in-vitro dissolution of shellac from PGSS supercritical CO₂ technique, *International Journal of Pharmaceutics*, vol. 499, Issues 1–2, pp. 205–216, 29 Feb. 2016.
- [6] E. Weidner, V. Wiesmet, Ž. Knez and M. Škerget, Phase equilibrium (solid-liquid-gas) in polyethyleneglycol-carbon dioxide systems, *The Journal of Supercritical Fluids*, vol. 10, pp.139–147, 1997.
- [7] Ž. Knez, M. Škerget, M. Knez Hrnčič and D. Čuček, *Supercritical Fluid Technology for Energy and Environmental Applications, Particle Formation Using Sub- and Supercritical Fluids*, Amsterdam: Elsevier Science Ltd, 2014.
- [8] K. Fukne-Kokot, A. König, Ž. Knez and M. Škerget, Comparison of different methods for determination of the S–L–G equilibrium curve of a solid component in the presence of a compressed gas, *Fluid Phase Equilibria*, vol. 173, p.297, 2000.
- [9] K. Fukne-Kokot, M. Škerget, A. König and Ž. Knez, Modified freezing method for measuring the gas solubility along the solid–liquid–gas equilibrium line, *Fluid Phase Equilibria*, vol. 205, pp. 233–247, 2003.
- [10] M. Škerget, Z. Novak-Pintarič, Ž. Knez and Z. Kravanja, Estimation of solid solubilities in supercritical carbon dioxide: Peng–Robinson adjustable binary parameters in the near critical region, *Fluid Phase Equilibria*, vol. 203, Issues 1–2, pp. 111–132, Dec. 2002.

- [11] G. Kravanja, M. Knez Hrnčič, M. Škerget, Ž. Knez, Interfacial tension and gas solubility of molten polymer polyethyleneglycol in contact with supercritical carbon dioxide and argon. *The Journal of supercritical fluids*, vol. 108, pp. 45-55, Feb. 2016.
- [12] E. Weidner, High pressure micronization for food applications, *The Journal of Supercritical Fluids*, vol. 47, pp.556–565, 2009.
- [13] M. Pintado-Sierra, L. Delgado, I. Aranaz, Á. Marcos-Fernández, H. Reinecke, A. Gallardo, D. Zeugolis and C. Elvira, Surface hierarchical porosity in poly(ϵ -caprolactone) membranes with potential applications in tissue engineering prepared by foaming in supercritical carbon dioxide, *The Journal of Supercritical Fluids*, vol. 95, pp. 273–284, 2014.
- [14] D. Raps, N. Hossieny, C.B. Park and V. Altstädt, Past and present developments in polymer bead foams and bead foaming technology, *Polymer*, vol. 56, pp. 5–19, 2015.
- [15] Ž. Knez, E. Markocic, Z. Novak and M. Knez Hrnčic, Processing Polymeric Biomaterials using Supercritical CO₂, *Chemie Ingenieur Technik*, vol. 83 (9), pp. 1371-1380, 2011.
- [16] T. Kegl, G. Kravanja, Ž. Knez and M. Knez Hrnčič, Effect of addition of supercritical CO₂ on transfer and thermodynamic properties of biodegradable polymers PEG 600 and Brij52, *The Journal of Supercritical Fluids*, vol. 122, pp. 10-12, 2017.
- [17] Ž. Knez, High pressure processes technology-Quo vadis?, *Chemical Engineering Research and Design*, vol. 82 (A12), pp. 1541–1548, 2004.

Perspective $BaCe_{0.5}Zr_{0.3}Ln_{0.2}O_{3-\Delta}$ ($Ln = Y, Dy, Sm$ and Nd) Proton-Conducting Electrolytes for Solid Oxide Fuel Cells

JULIA LYAGAEVA, ELENA PIKALOVA, NIKOLAI DANILOV, DMITRY MEDVEDEV,
ANATOLY DEMIN & PANAGIOTIS TSIAKARAS

Abstract The development of highly efficient solid-state electrochemical systems demands the investigation of new electrolyte materials that possess the required set of target properties. The present work highlights the results of phase and structural analysis of $BaCe_{0.5}Zr_{0.3}Ln_{0.2}O_{3-\delta}$ ($Ln = Y, Dy, Sm$ and Nd) proton-conducting oxides as well as their electrical conductivity depending on their composition and sintering conditions. Dy-containing material was found to exhibit high-quality ceramic properties and superior ionic conductivity, which makes it a promising electrolyte for applied purposes. CO_2 and Ar in polyethylene glycol, diffusion coefficients, density and interfacial tension have been determined in the frame of our previous research. Application of supercritical fluids in polymer particle formation and foaming processing are presented. PGSSTM (Particles from Gas-Saturated Solutions) is useful for production of polymer powder or entrapping of active ingredients in polymer matrices. Microcellular polymeric foams produced by depressurization in batch mode, using supercritical CO_2 as blowing agent, can provide significant environmental benefits.

Keywords: • $BaCeO_3$ • $BaZrO_3$ • acceptor doping • proton conductivity • electrochemical impedance spectroscopy •

CORRESPONDENCE ADDRESS: Julia Lyagaeva, Ph.D., Researcher, Institute of High Temperature Electrochemistry, Laboratory of electrochemical devices based on solid oxide proton electrolytes, Academicheskaya str. 20, 620137 Yekaterinburg, Russia, e-mail: yulia.lyagaeva@ya.ru. Elena Pikalova, Ph.D., Senior Researcher, Institute of High Temperature Electrochemistry, Laboratory of Solid Oxide Fuel Cells, Academicheskaya str. 20, 620137 Yekaterinburg, Russia, Leading Researcher, Associate Professor, Ural Federal University, Department of environmental economics, Mira st. 19, 620002, e-mail: e.pikalova@list.ru. Nikolai Danilov, Ph.D. Student, Institute of High Temperature Electrochemistry, Laboratory of electrochemical devices based on solid oxide proton electrolytes, Academicheskaya str. 20, 620137 Yekaterinburg, Russia, e-mail: nickdanilov7@gmail.com. Dmitry Medvedev, Ph.D., Senior Researcher, Institute of High Temperature Electrochemistry, Laboratory of electrochemical devices based on solid oxide proton electrolytes, Academicheskaya str. 20, 620137 Yekaterinburg, Russia, Senior Researcher, Ural Federal University, Department of environmental economics, Mira st. 19, 620002, e-mail: dmitrymedv@mail.ru. Anatoly Demin, Ph.D., Senior Researcher, Institute of High Temperature Electrochemistry, Laboratory of electrochemical devices based on solid oxide proton electrolytes, Academicheskaya str. 20, 620137 Yekaterinburg, Russia, e-mail: a.demin@imte.uran.ru. Panagiotis Tsiakaras, Professor, Laboratory of Alternative Energy Conversion Systems, Department of Mechanical Engineering, School of Engineering, University of Thessaly, Pedion Areos, Volos, Greece, e-mail: tsiak@uth.gr.

1 Introduction

Oxide materials which have high-temperature proton conductivity and also oxygen ionic conductivity have been intensively studied from the viewpoint of their prospective application in various electrochemical devices [1]. These characteristics make them suitable for use in solid oxide fuel cells (SOFCs) where they can attain a greater power output than devices based on unipolar oxygen-ion conductors [2]. To date, model laboratory cells have been able to demonstrate their outstanding output characteristics [3]. However, time-stability and cycling modes still seem to be unsatisfactory and irreproducible.

Optimizing the electrolytes' properties is one possible way of increasing the efficiency and stability of SOFCs. Materials from a series of BaCeO₃–BaZrO₃ solid solutions are currently of great interest due to their high values of ionic conductivity combined with good stability [4]. Within this system, mainly Y-doped representatives were applied as electrolytes for SOFCs [5]. This study aims at the synthesis and characterization of new proton-conducting electrolytes in comparison with the traditional yttrium-doped electrolyte in order to select the most suitable material for application in SOFC technology.

2 Experimental

2.1 Synthesis and sintering procedures

Materials with chemical composition of BaCe_{0.5}Zr_{0.3}Ln_{0.2}O_{3-δ} (or BCZLn, where Ln = Y, Dy, Sm and Nd) were obtained using a citrate-nitrate synthesis technique. Stoichiometric amounts of high purity Ba(NO₃)₂, Ln(NO₃)₃·6H₂O and ZrO(NO₃)₂ were dissolved in distilled water under thorough stirring and the drop-by-drop introduction of citric acid in a mole ratio of it to the metal cations equal to 2:1. The as-obtained transparent solution was treated at 200 °C until the residue self-ignition. The obtained powders were milled and calcined in two stages: at 700 °C for 5 h to remove organic remains and at 1150 °C for 5 h to complete BaCO₃ decomposition. Finally, the milled powders were dry-pressed in disks and sintered at 1450 and 1600 °C for 5 h. Since the presence of Zr⁴⁺ results in a considerable deterioration in the sintering, a small amount of CuO sintering additive (no more than 0.5 wt%) was introduced to improve the materials' sinterability and ensure the formation of dense ceramic electrolytes [6].

2.2 Materials characterization

The phase structure of the as-sintered BCZLn ceramics was studied using a Rigaku diffractometer (D/MAX-2200VL/PC). The details of this analysis were as follows: room temperature, CuK_{α1} radiation monochromatized by Si-monocrystal, a range of 15°≤2θ≤85°, a scan rate of 0.5° min⁻¹ and a step of 0.02°.

To determine the relative density, the dimensions of the as-prepared ceramics were measured after the sintering. The morphology of the sintered samples was investigated using a scanning electron microscope (JSM-5900 LV). The main grain size values were evaluated using software described elsewhere [7].

The electrical conductivity was studied by two-probe impedance spectroscopy using a FRA-1260 with EI-1287 (Solartron Instruments Inc.) in the frequency range of 0.1 Hz–0.5 MHz and with an amplitude of 30 mV. The impedance spectra were collected between 200 and 500 °C in dry and wet air. The dry atmosphere ($p_{\text{H}_2\text{O}} = 1 \cdot 10^{-4}$ atm; where $p_{\text{H}_2\text{O}}$ is the water vapor partial pressure) was created by passing air through a zeolite column, whereas the wet atmosphere ($p_{\text{H}_2\text{O}} = 3 \cdot 10^{-2}$ atm) was obtained by passing air through a water bubbler at 25 °C.

3 Results and Discussion

3.1 Phase structure and microstructure

Figure 1 shows the results of XRD analysis for BCZLn sintered at different temperatures. All the as-prepared materials were single-phase and possessed a cubic perovskite structure (space group Pm3m) except for the BCZNd ceramic sintered at 1600 °C which contained a trace amount of undefined impurity along with the main perovskite phase. On the basis of the comparative analysis of (110) and (200) reflexes located near $2\theta \approx 30^\circ$ and 42° , respectively, it was found that the ceramics sintered at 1450 °C exhibited a partial texturing, the degree of which increased with an increase in the Ln³⁺ ionic radius. The formation of the textured ceramics in similar oxide systems has been reported recently in [8]. A possible cause of such texturing is that the acceptor dopant with high ionic radius, introduced in the B-sublattice of the BaBO₃ perovskite structure (B = Ce, Zr), can also partially substitute the Ba²⁺-ions. As a result, ex-solution of small BaO amount and its reaction with CuO can initiate a top-seeded-melt-growth and, thus, formation of the textured materials [9].

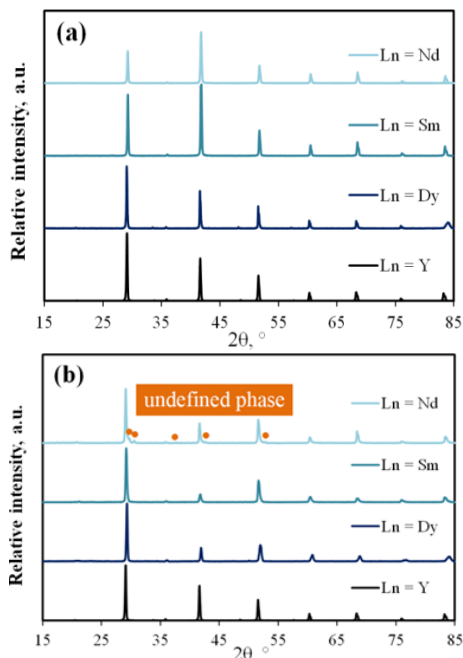


Figure 1. The XRD patterns of the BCZLn ceramics sintered at 1450 °C (a) and 1600 °C (b)

This can also be a possible explanation for absence of a correlation between the Ln^{3+} ionic radius and unit cell parameters (Table 1). It is interesting to note that the ceramics sintered at 1600 °C displayed the typical XRD patterns for normally-oriented crystallites. Probably, an increase in sintering temperature results in a reduction to the degree of Ba-site substitution. This may be the reason for slight changes in lattice parameters of the same materials sintered at different temperatures (Table 1).

The relative densities for all the prepared ceramic samples were found to be greater than 95%. Figure 2 shows the microstructure of the BCZLn ceramics.

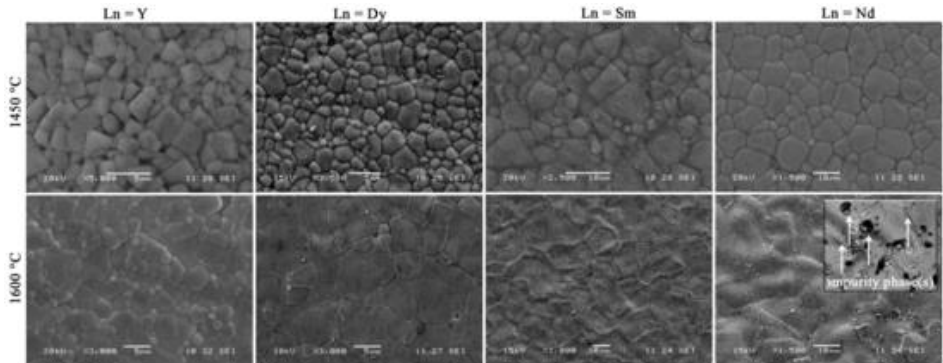


Figure 2. The surface morphology of the BCZLn materials sintered at 1450 and 1600 °C

No open porosity was observed for the samples regardless of the Ln³⁺ nature and sintering conditions. However, both these parameters affect the microstructure, facilitating the grain growth with an increase in the Ln³⁺ ionic radius as well as the sintering temperature (Figure 3).

Table 1. Unit cell parameters of the sintered BCZLn ceramic materials

Ln	$r_{Ln^{3+}}^{VI}$, Å	$a@1450\text{ °C}$, Å	$a@1600\text{ °C}$, Å
Y	0.900	4.351(3)	4.324(1)
Dy	0.912	4.342(4)	4.316(7)
Sm	0.958	4.355(1)	4.347(4)
Nd	0.983	4.337(5)	4.336(2)

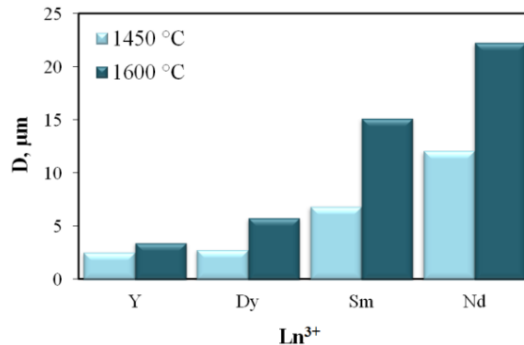


Figure 3. The mean grain size of the BCZLn ceramic materials sintered at 1450 and 1600 °C

Traces of melting processes were noticeable for the BCZSm and BCZNd samples sintered at 1600 °C. This also concurs with the assumption of the liquid-phase appearance in the case of doping by elements with high ionic radii. Moreover, the impurity phase (detected earlier by the XRD analysis) segregates on the grain boundary regions of

BCZNd, which can be clearly seen in the figure obtained by back-scattered electron imaging.

3.2 Electrical properties

3.2.1 Grain conductivity

Electrochemical impedance spectroscopy (EIS) was successfully used to decouple the contributions of grain (σ_g) and grain boundary ($\sigma_{g.b.}$) conductivities of the BCZLn materials. Figure 4 displays the typical impedance data obtained for the Dy-containing sample. As can be seen, the impedance response consists of three clearly distinguishable semicircles: (1) a high-frequency arc with a capacitance of $\sim 10^{-11}$ F cm^{-2} corresponding to the bulk (grain) properties; (2) the second semicircle at medium frequency range with a capacitance of $\sim 10^{-8}$ F cm^{-2} , which is associated with the grain boundaries' characteristics; (3) a low-frequency arc with a capacitance of $\sim 10^{-5}$ F cm^{-2} typical for the electrodes' polarization. An equivalent circuit with three serial RQ elements was used for impedance spectra analysis (Z-view software).

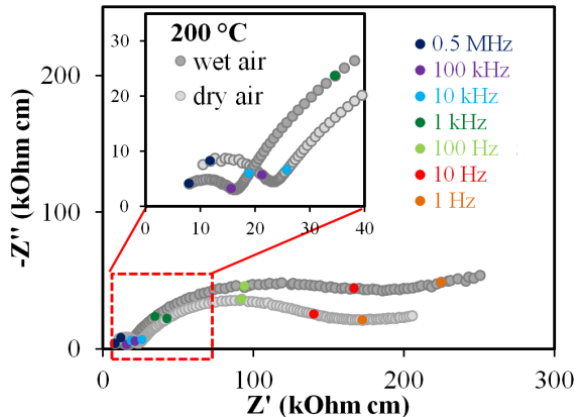


Figure 4. The examples of typical impedance spectra for the BCZDy ceramic sintered at 1450 °C for 5 h

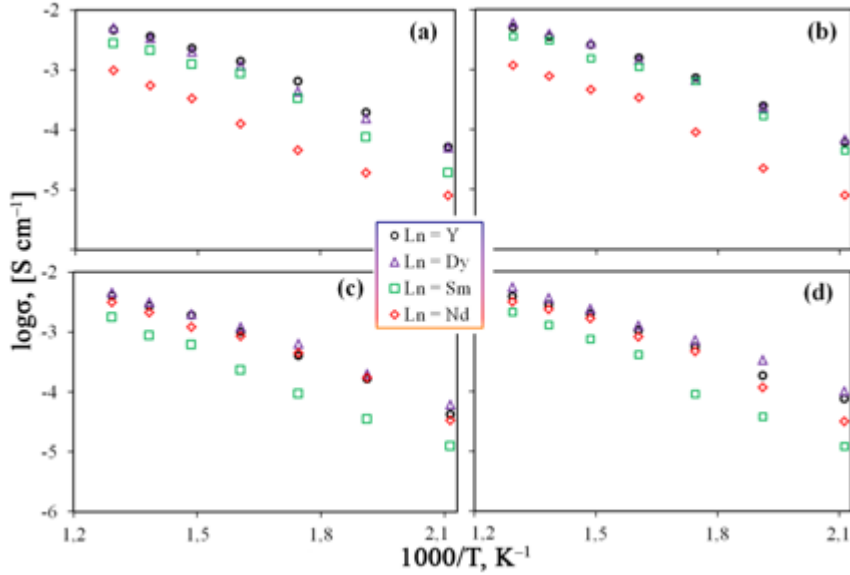


Figure 5. The temperature dependences of grain conductivity obtained in dry air (a,c) and wet air (b,d) for the BCZLn samples sintered at 1450 °C (a,b) and 1600 °C (c,d)

Figure 5 depicts the grain conductivity of BCZLn depending on sintering condition and pH₂O in air. When the ceramic materials are sintered at 1450 °C, the grain conductivity tends to decrease as the Ln³⁺ ionic radius is increased, except BCZDy, which demonstrates superior bulk, grain boundary and total conductivity.

A similar tendency of conductivity deterioration when increasing the Ln³⁺ ionic radii has been reported recently for similar systems [10, 11]. This deterioration may be explained as follows. The acceptor-doping (Ln₂O₃) causes formation of different point defects in the perovskite structure (BaBO₃, B = Ce/Zr):



where Ln'_{Ce,Zr} is the lanthanum-ion occupying the B-position in BaBO₃ and V_O^{••} is the oxygen vacancy. Since the formed oxygen vacancies determine the oxygen-ionic conductivity, it will increase as the V_O^{••} concentration is intensified (when the corresponding mobility will not decrease). In the case of acceptors with small ionic radii the oxygen vacancies' concentration directly depends on the Ln₂O₃ amount:

$$[\text{Ln}'_{\text{Ce,Zr}}] = 1/2[\text{V}_\text{O}^{\bullet\bullet}] \quad (2)$$

However, in the case of acceptors with high ionic radii, Ln^{3+} can partially substitute the Ba-cation even if they are introduced nominally to B-position, as was mentioned above [5]:



In accordance with such a simplified reaction, Ln_2O_3 also acts as a donor dopant (in respect to Ba^{2+}) leading to a reduction in the concentration of oxygen vacancies.

The grain conductivity of BCZY and BCZDy does not change notably on sintering temperature change, but for the other materials it varies, remaining lower compared to the conductivity of the Y- and Dy-containing materials.

The activation energy (E_a) of grain conductivity is rather low (below 0.6 eV, Figure 6). From this viewpoint, all the BCZLn materials exhibit mainly ionic transport under the chosen conditions because higher E_a are typical for electronic (hole) conductivity in cerates and zirconates [1]. In most cases, an increase of pH_2O results in a slight increase in the conductivity and a reduction in the E_a values, indicating the formation of more mobile protonic charge carries as compared to oxygen vacancies:



where $\text{OH}_\text{O}^{\bullet}$ is the proton defect.

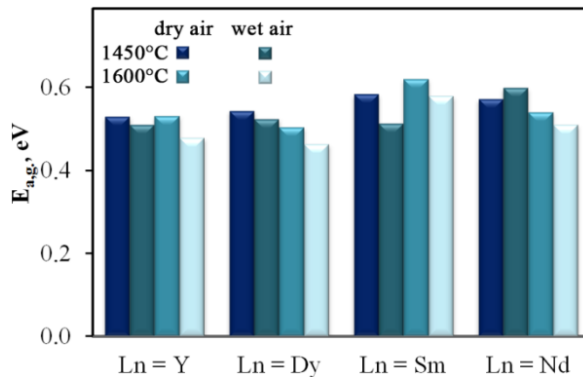


Figure 6. The activation energy of the grain conductivity depending on sintering temperature and air humidity

3.2.2 Grain boundary conductivity

Behavior of grain boundary conductivity is presented in Figure 7. Apart from the chemical composition of the main phase, the structure of the boundaries (grains size, impurity phases) considerably affects the grain boundary transport. The comparative analysis of Figures 3 and 8a demonstrates that the grain size increases and correspondingly grain boundary density decreases when the sintering temperature and Ln³⁺ ionic radius increase. However, dependence of $\sigma_{g.b.}$ on the Ln³⁺ type is more complicated, it increases in the series BCZY – BCZNd – BCZSm – BCZDy. Excluding the BCZDy composition from this series, the increase in grain boundary conductivity from BCZY to BCZSm can also be associated with the size characteristics of the grains. The subsequent drop of $\sigma_{g.b.}$ from BCZSm to BCZNd can be associated with a significant change in chemical composition under the partial substitution of Ba²⁺ by Nd³⁺ ions, which results in an appearance of impurity phases and their segregation near grain boundary regions (Figure 2). The activation energy values confirm the possible influence of impurity phases on the grain boundary transport in the case of BCZNd (Figure 8b).

Focusing on the BCZDy sample, the reason for enhanced electrical (total, grain and grain boundary) conductivity is not yet clear. However, the outstanding properties of proton conductors based on Dy-doped barium cerates and zirconates confirm the presence of regularity. For example, in a recent work of Bu et al. [10], Dy-containing samples were found to exhibit the highest conductivity in dry and wet air; Iwahara et al. [12] reported the highest protonic conductivity of Dy-doped BaCeO₃ in a hydrogen atmosphere. According to Han et al. [13], dysprosium was found to be a promising dopant for the design of new BaZrO₃-based protonic conductors. compared with that of Y-, Yb-, Gd-, Sm- and Nd-doped samples.

4 Conclusion

This work presents the results concerning the preparation as well as structural, microstructural and electrical characterizations of the prospective BaCeO₃–BaZrO₃ proton-conducting electrolytes. The BaCe_{0.5}Zr_{0.3}Ln_{0.2}O_{3-δ} (BCZLn, Ln = Y, Dy, Sm and Nd) materials were successfully prepared by the citrate-nitrate synthesis technique and sintered at 1450 and 1600 °C. All materials (except BCZNd sintered at 1600 °C) were single-phase and exhibited high relative density. The analysis of grain and grain boundary conductivities at relatively low temperatures (200–500 °C) revealed the regularities in the partial Ba²⁺ with Ln³⁺ substitution and grain boundary density.

The BCZDy material demonstrates the highest values in total, grain and grain boundary conductivities in both dry and wet air atmospheres. Therefore, it can be considered as a promising proton-conducting electrolyte for the development of new electrochemical devices operating in an intermediate-temperature range.

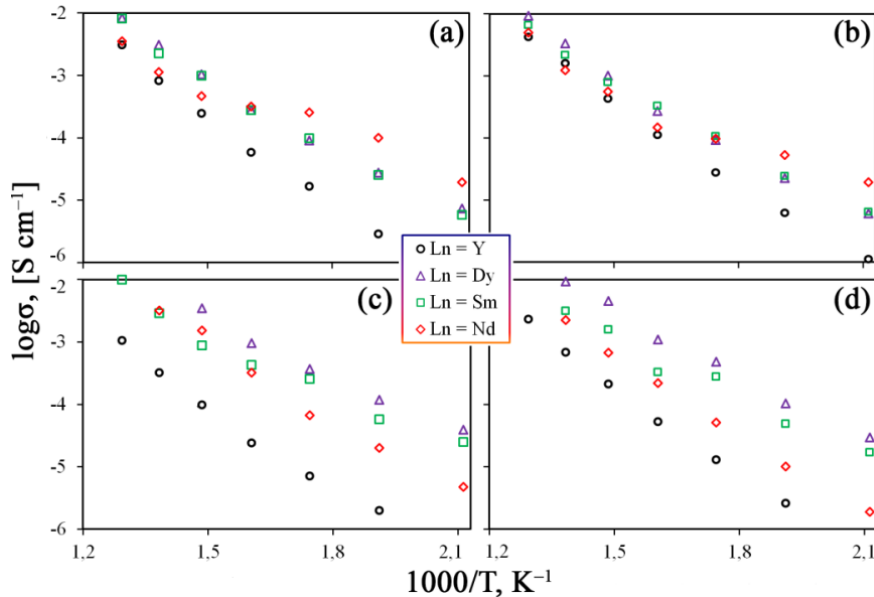


Figure 7. The temperature dependences of grain boundary conductivity obtained in dry air (a,c) and wet air (b,d) for the BCZLn samples sintered at 1450 °C (a,b) and 1600 °C (c,d)

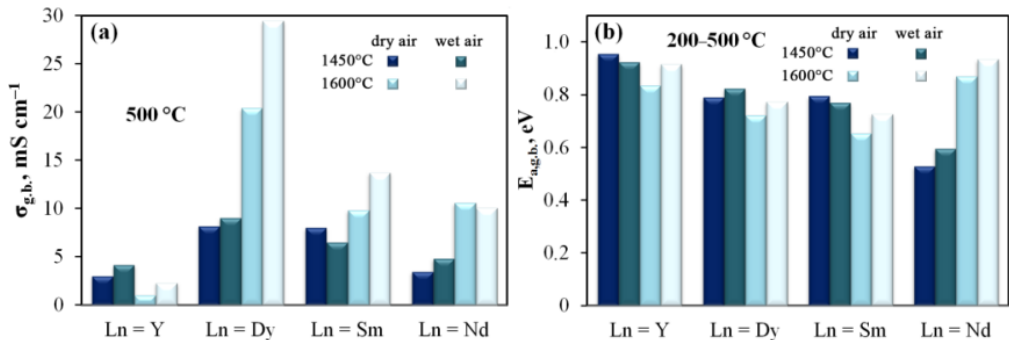


Figure 8. Grain boundary conductivity (a) and corresponding activation energy (b) behaviour for BCZLn depending on sintering temperature and air humidity

Acknowledgements

This work is financially supported by the Ministry of Education and Science of the Russian Federation (Mega-grant, contract no. 14.Z50.31.0001) and the Russian Foundation for Basic Research (grant no. 16-33-00006). Dr D. Medvedev is also grateful to the Council of the President of the Russian Federation (grant no. CII-1885.2015.1).

References

- [1] N. Kochetova, I. Animitsa, D. Medvedev, A. Demin, and P. Tsiakaras, “Recent activity in the development of proton-conducting oxides for high-temperature applications”, *RSC Adv.*, vol. 6, pp. 73222–73268, Aug. 2016.
- [2] A. Demin, P. Tsiakaras, E. Gorbova, and S. Hramova, “A SOFC based on a co-ionic electrolyte”, *J. Power Sources*, vol. 131, pp. 231–236, May 2004.
- [3] C. Duan, J. Tong, M. Shang, S. Nikodemski, M. Sanders, S. Ricote, A. Almonsoori, and R. O’Hayre, “Readily processed protonic ceramic fuel cells with high performance at low temperatures”, *Science*, vol. 349, pp. 1321–1326, Sep. 2015.
- [4] K. D. Kreuer, “Proton-conducting oxides”, *Annu. Rev. Mater. Res.*, vol. 33, pp. 333–359, Apr. 2003.
- [5] D. A. Medvedev, J. G. Lyagaeva, E. V. Gorbova, A. K. Demin, P. Tsiakaras, “Advanced materials for SOFC application: Strategies for the development of highly conductive and stable solid oxide proton electrolytes”, *Progr. Mater. Sci.*, vol. 75, pp. 37–79, Aug. 2016.
- [6] D. A. Medvedev, A. A. Murashkina, and A. K. Demin, “Formation of dense electrolytes based on BaCeO₃ and BaZrO₃ for application in solid oxide fuel cells: the role of solid-state reactive sintering”, *Rev. J. Chem.*, vol. 5, pp. 193–214, July 2015.
- [7] M. Ananyev, D. Medvedev, A. Gavriyuk, S. Mitri, A. Demin, V. Malkov, and P. Tsiakaras, “Cu and Gd co-doped BaCeO₃ proton conductors: Experimental vs SEM image algorithmic-segmentation results”, *Electrochim. Acta*, vol. 125, pp. 371–379, Apr. 2014.
- [8] J. Lyagaeva, D. Medvedev, E. Filonova, A. Demin, and P. Tsiakaras, “Textured BaCe_{0.5}Zr_{0.3}Ln_{0.2}O_{3-δ} (Ln = Yb, Y, Gd, Sm, Nd and La) ceramics obtained by the aid of solid-state reactive sintering method”, *Scripta Mater.*, vol. 109, pp. 34–37, July 2015.
- [9] Y. Chen, X. Cui, and X. Yao, “Peritectic melting of thin films, superheating and applications in growth of REBCO superconductors”, *Progr. Mater. Sci.*, vol. 68, pp. 97–159, March 2015.
- [10] J. Bu, P. G. Jönsson, and Z. Zhao, “Ionic conductivity of dense BaZr_{0.5}Ce_{0.3}Ln_{0.2}O_{3-δ} (Ln = Y, Sm, Gd, Dy) electrolytes”, *J. Power Sources*, vol. 272, pp. 786–793, Sept. 2014.
- [11] J. Lyagaeva, B. Antonov, L. Dunyushkina, V. Kuimov, D. Medvedev, A. Demin, and P. Tsiakaras, “Acceptor doping effects on microstructure, thermal and electrical properties of proton-conducting BaCe_{0.5}Zr_{0.3}Ln_{0.2}O_{3-δ} (Ln = Yb, Gd, Sm, Nd, La or Y) ceramics for solid oxide fuel cell applications”, *Electrochim. Acta*, vol. 192, pp. 80–88, Feb. 2016.
- [12] H. Iwahara, T. Hibino, and M. Yamada, *Proceedings of the 3rd International Symposium on Solid Oxide Fuel Cell*. Pennington, NJ: Electrochemical Society, 1993.
- [13] D. Han, Y. Nose, K. Shinoda, and T. Uda, “Site selectivity of dopants in BaZr_{1-y}M_yO_{3-δ} (M=Sc, Y, Sm, Eu, Dy) and measurement of their water contents and conductivities”, *Solid State Ionics*, vol. 213, pp. 2–7, Oct. 2012.

Methanol an Energy Source Production by Reduction of CO₂ Under Visible Light Irradiation Using Fe₂O₃/TiO₂ Nanotube Immobilized Activated Carbon Fiber

AJIT SHARMA & BYEONG-KYU LEE

Abstract The hydrothermal method was explored to prepare Fe₂O₃/TiO₂ nanotubes (NTs) with the special faces on the surface of activated carbon fibers (ACFs). Based on the SEM and XRD results, the formation process of the hierarchically assembled Fe₂O₃/TiO₂ NTs was deduced. The Fe₂O₃/TiO₂ NTs immobilized ACFs (Fe₂O₃/TiO₂/ACF) catalyst that had reached for CO₂ reduction at 120 mins behaved the best photo-catalytic properties. From the view of photocatalytic reduction, the conduction band (0.75 eV) is negative enough to drive CO₂ reduction, and the valence band (1.82 eV) is positive enough to oxidize H₂O to generate proton, and then the proton is used for CO₂ reduction. From the results, the methanol yield in 120 min over NT-Fe₂O₃/TiO₂/ACF was 628.3 μmol.g⁻¹ and 1103 μmol.g⁻¹ under UV and visible light irradiation, respectively. The NT-Fe₂O₃/TiO₂/ACF was also easily separated from the reaction medium for regeneration and showed good stability after multiple uses.

Keywords: • ACFs • Fe₂O₃/TiO₂ nanotube • CO₂ • photo-reduction • energy source •

CORRESPONDENCE ADDRESS: Ajit Sharma, University of Ulsan, Department of Civil and Environmental Engineering, Nam-gu, Daehak ro 93, Ulsan 680-749, Republic of Korea, e-mail: ajitsharma2003@gmail.com. Byeong-Kyu Lee, University of Ulsan, Department of Civil and Environmental Engineering, Nam-gu, Daehak ro 93, Ulsan 680-749, Republic of Korea, e-mail: bklee@ulsan.ac.kr.

<https://doi.org/10.18690/978-961-286-056-1.4>

ISBN 978-961-286-056-1

© 2017 University of Maribor Press

Available at: <http://press.um.si>.

1 Introduction

Carbon dioxide (CO₂) concentration has been growing since the fossil fuel combustion and respiration [1]. The carbon dioxide is widely recognized as not only one of the main greenhouse gases, but also a potential carbon resource. Anthropogenic CO₂ is emitted through the combustion or burning of waste and fossil fuels such as coal, oil, and natural gas [2]. The main anthropogenic activities include electricity generation and industrial processes that use fuel (petroleum or coal) combustion [3]. Deforestation is also a serious environmental threat in terms of CO₂ emissions [4]. Thus, the conversion of CO₂ into fuels such as methane, methanol, and formic acid has become one of the most attractive technologies to alleviate global warming and the energy crisis. Recently, various photocatalytic materials and nanocomposites (NCs) such as TiO₂, iron oxide nanorods (NRs), SnO₂ NRs/Fe₂O₃ NTs, Fe doped CeO₂ and Ti/ZnO–Fe₂O₃ photocatalytic NC systems have been investigated for their performances in the photocatalytic conversion of CO₂ into fuels [5-9]. In a certain excitation phase, catalytic materials generate electrons, which can move to the conduction band, and holes, which remain in the valence band. The electrons are accelerated or transformed from the surface of the catalyst to reduce or convert CO₂ into fuels and also the remaining holes produced by oxygen via oxidation of water molecules [4-6]. At present, TiO₂-based NCs have attracted intense research interest owing to their unique properties and wide-ranging applications in several research fields such as water treatment, chemical catalysis, surface coating and battery application via photocatalysis [9-10]. The production of fuels from the reduction of CO₂ is a multistep process comprised of sorption, CO₂ activation and dissociation of C-O bond [4-5]. However, recently developed photocatalytic composites that have been tried for CO₂ reduction into fuels show low CO₂ sorption, which is the preliminary phase for conversion of CO₂, leading to a low rate of CO₂ conversion process. Moreover, TiO₂-supported NiO catalyst was used for the production of hydrogen through methane decomposition [11] and CO₂ methanation [12]. In spite of these aforementioned advantages, the reduction of CO₂ still suffers from very low efficiencies for CO₂ conversion due to the fast electron–hole recombination rate in the photocatalysts; a major barrier that needs to be overcome. However, no study has focused on the preparation and photocatalytic activity of bi-metallic nanorod (Fe₂O₃/TiO₂)-impregnated ACFs for fast sorption of CO₂ due to the porous structure of the carbon basal support and high efficiency of CO₂ conversion due to bi-metal nanorod immobilization on the ACF surface under visible phase.

Therefore, in this study, ACFs were used as the substrate to immobilize Fe₂O₃ co-doped TiO₂ nanorod (NT-Fe₂O₃/TiO₂/ACF) to enhance the adsorption capacity of CO₂. The Fe₂O₃ nanorod used as a dopant on the TiO₂ surface also induced the formation of new adsorption sites, in which CO₂ is bonded. Furthermore, Fe₂O₃ co-doped TiO₂ nanorod overcame the fast electron–hole recombination rate problem for the conversion of CO₂ into methanol under visible light phase.

2 Experimental

2.1 Preparation of Fe₂O₃/TiO₂ nanoparticle-deposited ACF

Iron nitrate (Fe(NO₃)₃·9H₂O) was loaded in the titanium tetraisopropoxide (TTIP) solution with addition of ACF during the sol-gel method used to prepare (Fe₂O₃/TiO₂/ACF). In detail, acetic acid (12.05 mL) was added in the TIP (6.21 mL) solution with the addition of 60 mL ethanol solution for hydroxylation. The solution was stirred for 30 min at 25 °C for complete hydrolysis. Then, the aqueous solution (60 mL) of iron nitrate (0.05 wt %) with double distilled water was mixed into the above TTIP solution. Afterwards, the ACFs (0.2g) were used as the substrate for the deposition of Fe₂O₃/TiO₂ nanoparticles. Then ACFs substrate was dipped in the afterwards above homogeneous solution for 120 min, then ACFs substrate was taken out and washed with ethanol to remove the excess of TTIP precursor between the fibers and then dried at 75 °C for 12 h. In order to promote Fe₂O₃/TiO₂ to get better crystallization, the Fe₂O₃/TiO₂ immobilized ACFs was calcined at 450 °C in nitrogen atmosphere for 1.5 h, obtaining the sample Fe₂O₃/TiO₂/ACF.

2.2 Growth of Fe₂O₃/TiO₂ nanorod on ACF

Sample pieces of Fe₂O₃/TiO₂/ACF were put into 75 mL of 10 M NaOH aqueous solution, then transferred into a 100 mL Teflon-lined stainless steel autoclave, and sealed. The autoclave was put into an oven, heated at 150 °C for 18 h, cooled naturally in air and washed with deionized water several times until the sample pH reached 7. The morphological structure of Fe₂O₃/TiO₂ nanorod (NT-Fe₂O₃/TiO₂) on the ACFs surface (NT-Fe₂O₃/TiO₂/ACF) was determined by surface morphology analysis.

3 Result and Discussion

3.1 SEM morphology

The morphology of ACF, Fe₂O₃/TiO₂/ACF and NT-Fe₂O₃/TiO₂/ACF were analyzed by SEM analysis (Fig. 1). As shown in Fig. 1(a), the ACFs surface was almost clean after pre-treatment with many micropores that can function as active sites for adsorption. Fig. 1(b) shows SEM images of the Fe₂O₃/TiO₂/ACF composite prepared by the sol gel process. The nanoparticles (NPs) of Fe₂O₃/TiO₂ were uniformly deposited on the ACFs surface. As shown in Fig. 1(c), the growth of Fe₂O₃/TiO₂ nanorod (Fe₂O₃/TiO₂-NR) on the ACFs surface is in three-dimensional direction to a complex structure was produced. The nanorod structures of NT-Fe₂O₃/TiO₂ on the ACFs surface with an average length of 50-200 nm were confirmed in the SEM image (Fig. 1c). The highly uniform Fe₂O₃/TiO₂ nanorod structures were deposited on the ACFs surface with high crystallinity. The nanorod structures of NT-Fe₂O₃/TiO₂ on the ACFs surface exhibited great adsorption capacity and photocatalytic activity for complete CO₂ reduction for conversion into methanol.

3.2 Optical absorption

The optical absorption of the synthesized NT-Fe₂O₃/TiO₂/ACF displayed enhancement of the absorption at wavelengths in the region of 410-590 nm (Fig. 2). The significant enhancement of optical absorption in the visible region of NT-Fe₂O₃/TiO₂/ACF was due to a contribution of the plasmon resonance of the iron particles dispersed onto the TiO₂ surface. The plasmon resonance of Fe₂O₃ particles excited electrons of the valence band of TiO₂ and transferred the excited electrons from the valence band to the conduction band of TiO₂. The light absorption enhancement of NT-Fe₂O₃/TiO₂/ACF was also due to the role of the incorporated Fe₂O₃ nanoparticles particles, which bonded to TiO₂ via Fe-O-Ti bonding, leading to oxygen vacancies and the formation of Ti³⁺ in the TiO₂ lattice. Therefore, the formed Ti³⁺ also acted as an intermediate agent to enhance the transfer of electrons from the valence band to the conduction band of TiO₂, contributing to the enhancement of the optical absorption of the synthesized Fe₂O₃/TiO₂ nanorod (NT-Fe₂O₃/TiO₂) on the ACFs surface (NT-Fe₂O₃/TiO₂/ACF).

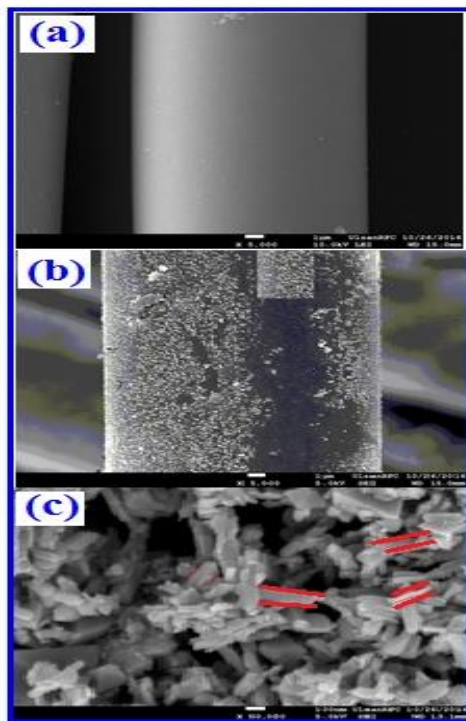


Fig. 1 SEM image of ACF (a), Fe₂O₃-TiO₂ nanoparticle on ACF Surface (b) and Fe₂O₃/TiO₂ nanorod on the ACFs surface (c)

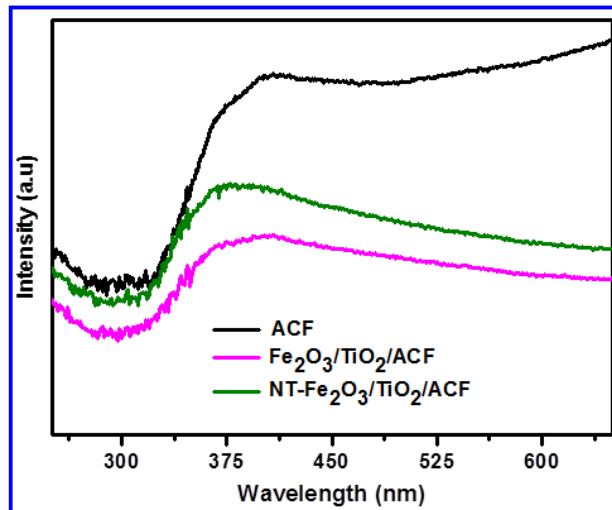


Fig. 2 UV-Vis spectra of composites

3.3 Reduction of CO₂ for CH₃OH production

Fig. 3 shows the methanol yield after the reduction of CO₂ under visible light irradiation by Fe₂O₃/TiO₂/ACF and NT-Fe₂O₃/TiO₂/ACF. The gross yield of methanol increased with increasing photo-reduction time. Under visible light irradiation, the Fe₂O₃/TiO₂ nanorod immobilized on ACFs increased the CO₂ conversion into methanol because the nanorod structure of Fe₂O₃/TiO₂ dopant greatly enhanced the separation of electron-hole pairs of the doped TiO₂ [5-6]. Thus, even under visible light irradiation the NT-Fe₂O₃/TiO₂/ACF generated electron-hole pairs that reacted with H₂O and CO₂ to produce methanol [7]. Moreover, Fe₂O₃/TiO₂ nanorod immobilized on ACFs not only possessed a large surface area, which is beneficial for the diffusion and mass transportation of CO₂ molecules and H⁺ ions, but also increased the solar energy harvest due to the efficient light scattering in the photochemical reduction [6, 8]. The visible light may have experienced multiple scattering between the NT-Fe₂O₃/TiO₂ and the porous ACF carbon substrate when visible light passed through the free space between Fe₂O₃/TiO₂ nanorod growths on ACF surface, thereby affording efficient light harvesting. The introduction of ACFs as a substrate with large surface area also increased the amount of exposed photocatalytic active sites, and hence enhanced the yield of methanol with Fe₂O₃/TiO₂/ACF and NT-Fe₂O₃/TiO₂/ACF to 628.3 and 1103 μmol/g, respectively, at 120 min.

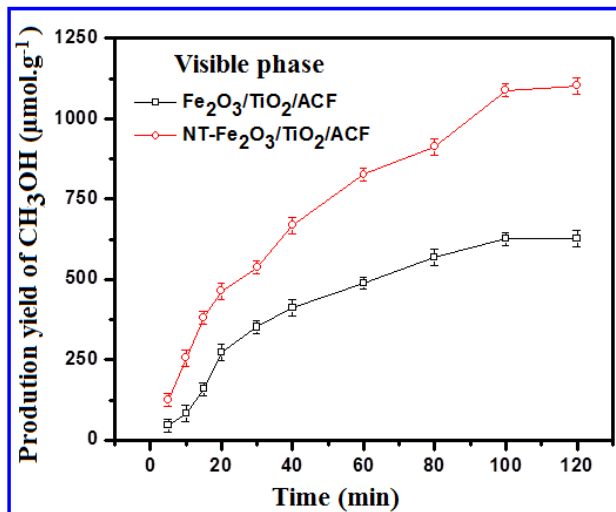


Fig. 3 Conversion of CO₂ into methanol under the presence and visible light irradiation

4 Conclusion

A stable Fe₂O₃/TiO₂ nanorod on the ACFs surface (NT-Fe₂O₃/TiO₂/ACF) was uniformly grown by hydrothermal process. The hierarchical porous structure and large surface area of ACFs provided a better sorption of CO₂ and the immobilized Fe₂O₃/TiO₂ nanorod provided a catalytic surface for CO₂ photo-reduction for conversion into methanol under visible light irradiation. In order to facilitate methanol formation, photo-generated carriers (electron-hole pairs) migrated to the surface of Fe₂O₃/TiO₂ nanorod and participated in the reduction and oxidation processes. The CO₂ photo-reduction by NT-Fe₂O₃/TiO₂/ACF demonstrated that the methanol yield over NT-Fe₂O₃/TiO₂/ACF in 120 min was 1103 μmol.g⁻¹ under visible light irradiation.

Acknowledgements

This work was supported by the Korea Research Fellowship Program through the National Research Foundation of Korea (NRF) funded by the Ministry of Science, ICT and Future Planning (2015H1D3A1066572)

Reference

- [1] S.Wang, Q. Li, C. Fang, C. Zhou, The relationship between economic growth, energy consumption, and CO₂ emissions: Empirical evidence from China. *Sci. Total Environ.* 542 (2016) 360–371.
- [2] D. Flórez-Orrego, J.A.M. Silva, S.D. Oliveira Jr., Renewable and non-renewable exergy cost and specific CO₂ emission of electricity generation: The Brazilian case, *Energ. Convers. Manage.* 85 (2014) 619–629.

- [3] J. Sheng, U.A. Ozturk, S. Zhang, Effects of asymmetric information and reference emission levels on the emissions from deforestation and degradation, *J. Clean. Prod.* 133 (2016) 1118-1127.
- [4] T.D. Pham, B.K. Lee, Novel capture and photocatalytic conversion of CO₂ into solar fuels by metals co-doped TiO₂ deposited on PU under visible light, *Appl. Catal. A-Gen.* 529 (2017) 40–48.
- [5] A. Nikokavoura, C. Trapalis, Alternative photocatalysts to TiO₂ for the photocatalytic reduction of CO₂, *Applied Surface Science* 391 (2017) 149–174.
- [6] H. Kloust, R. Zierold, J. Merkl, C. Schmidtke, A. Feld, E. Pösel, A. Kornowski, K. Nielsch, H. Weller, Synthesis of Iron Oxide Nanorods Using a Template Mediated Approach, *Chem. Mater.* 2015, 27, 4914–4917.
- [7] Zhongxue Yang , Huying Wang , Weijie Song , Wei Wei , Qingping Mu, Bo Kong , Peiqiang Li, Hongzong Yin, One dimensional SnO₂ NRs/Fe₂O₃ NTs with dual synergistic effects for photoelectrocatalytic reduction CO₂ into methanol, *Journal of Colloid and Interface Science* 486 (2017) 232–240.
- [8] S. Mansingh, D.K. Padhi, K.M. Parida, Enhanced photocatalytic activity of nanostructured Fe doped CeO₂ for hydrogen production under visible light irradiation, *International Journal of Hydrogen Energy* 41 (2016) 141 33 -14146,
- [9] Shengjie Xia, Yue Menga, Xiaobo Zhou, Jilong Xue, Guoxiang Pan, Zheming Ni, Ti/ZnO–Fe₂O₃ composite: Synthesis, characterization and application as a highly efficient photoelectrocatalyst for methanol from CO₂ reduction, *Applied Catalysis B: Environmental* 187 (2016) 122–133
- [10] A. Sharma, B.K. Lee, Energy savings and reduction of CO₂ emission using Ca(OH)₂ incorporated zeolite as an additive for warm and hot mix asphalt production, *Energy xxx* (2016) 1-9.
- [11] K. Kořcí, L. Matějová, M. Reli, L. Čapek, V. Matějk, Z. Lacný, P. Kustrowski, L. Obalová, Sol–gel derived Pd supported TiO₂-ZrO₂ and TiO₂ photocatalysts; their examination in photocatalytic reduction of carbon dioxide, *Catalysis Today* 230 (2014) 20–26.
- [12] L. Li, D. Mao, J. Xiao, L. Li, X. Guo, J. Yu, Facile preparation of highly efficient CuO–ZnO–ZrO₂/HZSM-5 bifunctional catalyst for one-step CO₂ hydrogenation to dimethyl ether: Influence of calcination temperature, *Chemical Engineering Research and Design* 111 (2016) 100–108.

Energy Efficient Poly(Lactide) Obtaining by Microwave Synthesis

IVAN RISTIĆ, MILOVAN JOTANOVIĆ, TAMARA ERCEG, LJUBIŠA NIKOLIĆ, SUZANA ČAKIĆ, VLADAN MIĆIĆ & STEFAN PAVLOVIĆ

Abstract The world is faced with the consequences of drastic reduction in fossil fuel reserves, because of their widespread use, not only as an energy source, but also as a feedstock for monomers obtaining. In order to solve this problem, the scientific community has focused on finding the new ways to exploit renewable resources and optimize the process of polymer materials production. The aim is to obtain applicable polymer whose complete life cycle is put in ecological framework. Poly(lactide) (PLA) meets these requirements as biodegradable polyester whose monomer is derived from plant feedstock containing carbohydrates. Different methods can be applied for PLA synthesis, but from the point of energy saving, as well as environmental protection, the microwave synthesis of PLA is the best solution. The use of microwaves enables homogenous heating of reaction mixture, lower consumption of organic solvent and drastic reduction in polymerization time, obtaining, in the same time, high molecular weight polymers.

Keywords: • poly(lactide) • microwave synthesis • energy efficiency • bandgap engineering • 3D •

CORRESPONDENCE ADDRESS: Ivan Ristić, assistant professor, University of Novi Sad, Faculty of Technology, Bulevar cara Lazara 1, 21000 Novi Sad, Serbia, e-mail: ivan.ristic@uns.ac.rs. Milovan Jotanović, full professor, University of East Sarajevo, Faculty of Technology Zvornik, Karakaj bb, 75400 Zvornik, Republic of Srpska, BiH, e-mail: jotanovicm@mail.ru. Tamara Erceg, research trainee, University of Novi Sad, Faculty of Technology, Bulevar cara Lazara 1, 21000 Novi Sad, Serbia, e-mail: tamara.erceg@uns.ac.rs. Ljubiša Nikolić, full professor, University of Niš, Faculty of Technology Leskovac, Bulevar Oslobođenja 124, 16000 Leskovac, Serbia, e-mail: nljubisa@yahoo.com. Suzana Čakić, full professor, University of Niš, Faculty of Technology Leskovac, Bulevar Oslobođenja 124, 16000 Leskovac, Serbia, e-mail: suzana_cakic@yahoo.com. Vladan Mićić, associate professor, University of East Sarajevo, Faculty of Technology Zvornik, Karakaj bb, 75400 Zvornik, Republic of Srpska, BiH, Karakaj 75400, e-mail: micicvladan@yahoo.com. Stefan Pavlović, assistant, University of East Sarajevo, Faculty of Technology Zvornik, Karakaj bb, 75400 Zvornik, Republic of Srpska, BiH, e-mail: stefan.pavlovi504@gmail.com.

1 Introduction

From the 19th century fossil fuels have been the primary energy source and the source for production of polymer materials. Excessive exploitation of fossil fuels has resulted in drastic reduction of their reserves as well as in economical and environmental pollution issues. Synergism of these factors has initiated the development and implementation the principles of the concept of energy saving. The concept of energy saving has several items including replacing fossil fuels by alternative energy resources and the use of renewable raw materials as feedstock for polymer synthesis. The interest in sustainable product was the driving force for the development of methods for obtaining, modifying and applying of biopolymers. Complete life cycle of such materials is fit into environmental framework, starting from their preparation to the final application and disposal. Biopolymers are biodegradable polymers extracted from the biomass or synthesized from the monomers obtained from the renewable resources. Natural resource origin and biodegradability of biopolymers make them more suitable for obtaining and using in comparison with conventional plastic. Those materials can be appropriate replacement for polymers derived from fossil fuels if they possess certain functional properties. Poly(lactide) (PLA) meets these requirements as biodegradable polyester whose monomer is derived from the plant feedstock containing carbohydrates. The main building block of PLA is lactic acid (2-hydroxypropanoic acid), that can be obtained either by fermentation of carbohydrates or chemical synthesis, but fermentation is the most common procedure for lactic acid obtaining [1, 2]. Waste products of the food industry and agriculture, rich in carbohydrates, can be used for the preparation of lactic acid by fermentation, which not only decreases the cost of polymer manufacture, but also solves the problem of waste disposal.

PLA is also important because of its biocompatibility; subjected to hydrolysis it gives a lactic acid that can be metabolised in human body as well as in natural environment.

Two optically active enantiomers of lactic acid (L and D) can give three forms of cyclic diester of lactic acid: L-lactide, D-lactide and D,L-lactide. Poly(lactic acid) is obtained by polymerization of lactic acid and the poly(lactide) is the product of polymerisation of lactide [2]. Depending on the ratio of enantiomers, it is possible to obtain PLA polymers with different properties [3].

Direct polycondensation of lactic acid gives only the low molecular weight polymer – poly (lactic acid). It is equilibrium reaction, with water as by-product, that should be removed during the synthesis, in order to get higher conversions. Removing of water during the synthesis as well as using a coupling agent to obtain higher molecular weights makes this process longer, more complicated and more expensive. For the preparation of high molecular weight polymer, cyclic lactide is used as monomer for the ring opening polymerisation (ROP) [4] (Figure 1). This process can be carried out via cationic, anionic and non-ionic insertion mechanism [2]. ROP process demands high purity of the monomer, specific catalyst and solvent. Depending on methods, it requires high temperature, high pressure or vacuum. Cationic polymerization is efficiently initiated by

trifluoromethanesulfonic acid (as a catalyst) in organic solvent such as dichloromethane [5]. The reaction takes place for at least four hours. Various metallic alkoxides are employed as initiator in anionic ROP polymerization of lactide in some organic solvent as reaction medium [6]. Tin (II) 2-ethylhexanoate SnOct_2 is one of the commonly used catalyst for the synthesis of poly(lactide). Two mechanisms are suggested for synthesis of PLA initiated by this catalyst. The first proposed mechanism is an activated monomer mechanism in which the monomer coordinate with SnOct_2 [7]. In the second proposed mechanism SnOct_2 reacts with compounds containing OH groups giving an initiator such as tin (II) alkoxide or hydroxide. Chain growth is achieved via inserting a monomer [8]. Therefore, different mechanisms are proposed for polymerization of lactide in solution. These traditional methods of synthesis require large consumption of energy, time and reagents. Polymerization in organic solvent takes place from 4 to 50 hours depending on applied mechanism, temperature, catalyst and solvent. The applied temperature ranges from 40 to even 280 °C. Long polymerization time and high temperature require significant quantities of energy.

Difficulties that occur during the traditional methods of PLA synthesis can be overcome using a microwave heating. This procedure simplifies and accelerates the reaction of polymerization of lactide that lasts only 5-30 minutes. Sensitivity of the reaction to impurities and moisture from the air is significantly reduced due to the fact that the reaction takes place very quickly, so there is no need for recrystallization of monomers or carrying out of reaction under the vacuum [2, 9]. Homogenous heating of the whole reaction mixture and high transfer energy per unit of time result in faster polymerization rate [9, 10]. Microwave synthesis allows obtaining a high molecular weight polymer in a short time in improved yield [9].

This paper gives a comparison of traditional and microwave method of PLA synthesis, emphasising the aspects of saving energy and resources accomplished by using a synthesis in microwave reactor.

2 Results and Discussion

The group of authors compared the parameters of different method for synthesis of PLA as well as properties of obtained polymers. They carried out synthesis in vacuum sealed vessels, synthesis in high pressure reactor, in dichloromethane and in microwave reactor [3, 9]. Synthesis in vacuum sealed vessels has taken 110-150 minutes, in high pressure reactor 4-8 hours, as well as in solution. Microwave synthesis has been lasted just for 0.17-0.5 hours. The consequence is reduced energy consumption followed by improved yield. Poly(lactide) samples synthesized in microwave reactor have high molecular weights, higher than ones synthesized by traditional methods [9].

Lactide absorbs the microwaves, so the temperature increases rapidly in the first 200 s (Figure 2). Exothermic effect of the polymerization reaction additionally leads to the temperature increasing.

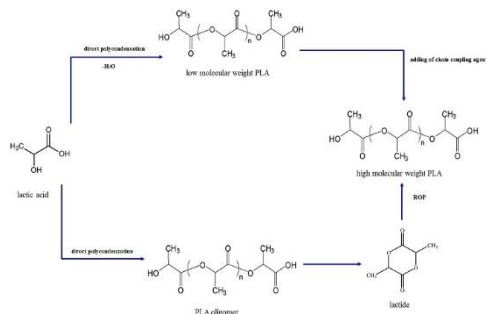


Figure 1. Synthesis of PLA via direct polycondensation and via ROP method.

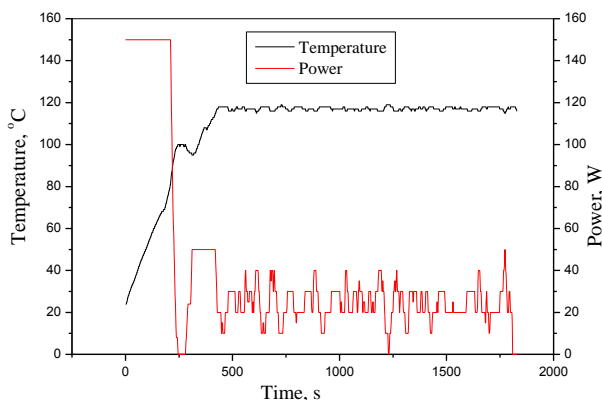


Figure 2. Temperature and microwave radiation power dependence on reaction time.

Loop on the upward curve comes from the presence of polymer and monomer in the reaction mixture, which have different abilities to absorb microwaves. Monomer shows greater ability to absorb microwaves than synthesized polymer. Between 8 and 9 minutes, temperature maintained on the same value of about 120 °C. This implies that conversion of monomer into polymer is almost complete. After reaching the value of 120 °C, temperature does not change.

Therefore, overheating does not occur during the microwave synthesis as it occurs during the bulk polymerization in vacuum sealed vessels. The applied power of 150 W at the beginning of reaction is reduced on 0 W after reaching the temperature value of 100 °C. Power of 40 W in pulses applied in the continuation of the reaction is enough for the maintaining the constant temperature.

The molecular structure of polymer synthesized by microwave polymerization was confirmed by FTIR analyses (Figures 3 and 4). Broad peak at 3465.22 cm^{-1} is due to the

O-H stretching. Weak peak at 2995.56, indicates the presence of C-H stretching and peaks at 2879.76 and 2831.19 cm^{-1} indicate the presence of C-CH₃ bond. CH₂ bending vibrations are confirmed by weak peak at 1453.55 cm^{-1} . Sharp peak at 1757.55 cm^{-1} implies the C=O stretching vibrations. In lactide FTIR spectrum (Figure 3), this peak is appeared at 1770.44 cm^{-1} . In FTIR spectrum of lactide C-O-C stretching vibrations are detected at 1267.28 and 1099,83 cm^{-1} (Figure 3). The asymmetrical valence vibrations of C-O-C of the aliphatic chain were shifted at 1188.76 cm^{-1} and symmetrical valence vibrations of C-O-C at 1090.69 cm^{-1} (Figure 4).

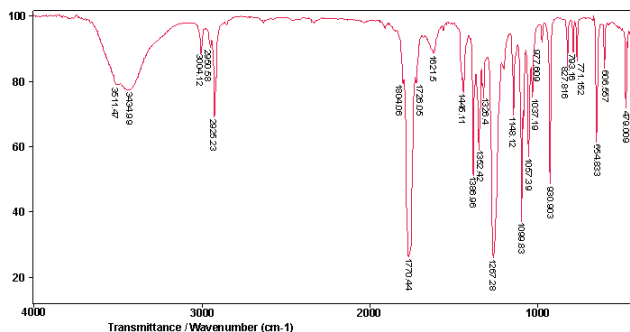


Figure 3. FTIR spectrum of monomer lactide.

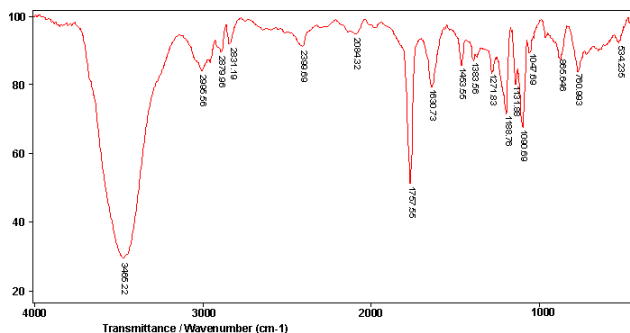


Figure 4. FTIR spectrum of poly(lactide).

Thermal properties of prepared poly(lactide) samples were investigated by differential scanning calorimetry (DSC). The comparative DSC curves are given in the Figure 5. The sample synthesized by traditional method has glass transition temperature (T_g) at 40.32 °C. Crystallization and melting behaviour was not observed. Endothermic and the exothermic peaks at DSC curve for PLA synthesized by microwave polymerization indicate presence of ordered structure. At temperature of 89.49 °C there is a maximum of the exothermic peak corresponding to the “cold” crystallisation of the amorphous region. Melting point is occurred at 135.45 °C, as minimum of endothermic peak. Based on the size of the area of endothermic and exothermic peaks, it can be estimated that enthalpy of crystallisation has higher absolute value than enthalpy of melting, because the melting

corresponding to initial crystalline fraction and newly crystalline regions developed by “cold” crystallisation.

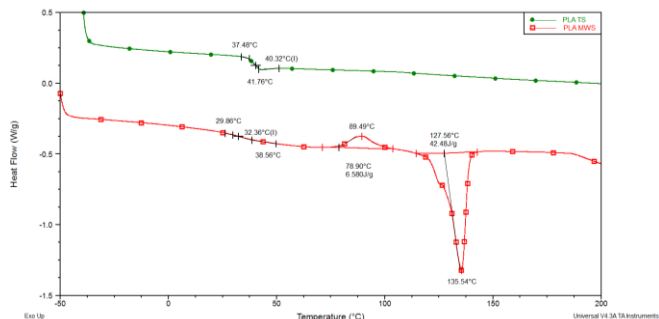


Figure 5. DSC curves for polymer synthesized by traditional method (PLA TS) and by microwave (PLA MW).

3 Conclusions

Reduced reserves of fossil fuels and problems with non-degradable waste have faced scientific community with necessity for investigation of renewable feedstock for production of polymer materials as well as development energy efficient process for their obtaining. Considering the process of obtaining and functional properties of poly(lactide), it was emerged as the great solution. Therefore, in accordance with the concept of energy saving, microwave synthesis of this polymer has been developed. Microwave synthesis gives high molar weight PLA with quite regular structure in improved yield. Shorter polymerization time and reduced consumption of energy and resources accompanied with desired properties of polymer, make microwave synthesis applicable to contemporary requirements.

Acknowledgements

This paper were supported by Ministry of Science and Technological Development, Republic Serbia; contract grant number: III 45022 and Ministry of Science and Technologia Republic of Srpska; number 19/6-020/961-83/15.

References

- [1] Benninga H. (Ed.) A History of Lactic Acid Making, Kluwer Academic Publishing, Boston, London, Dordrecht, 1990.
- [2] I. Ristić, Lj. Nikolić, S. Cakić, R. Radičević, B. Pilić and J. Budinski-Simendić, "Poli(laktid)- dostignuća i perspektive, Savremene tehnologije, vol. 1(1), pp. 67-77, June 2012.
- [3] I. Ristić, Lj. Tanasić, Lj., Nikolić, S. Cakić, O. Ilić, R. Radičević and J. Budinski-Simendić, "The Properties of Poly(L-Lactide) Prepared by Different Synthesis Procedure", Journal of Polymers and the Environment, vol. 19, pp. 419-430, March 2011.

- [4] G.W. Nice, T. Gluaser, E.F. Connor, A. Mork, R.M. Waymouth, J.L. Hedrick, "In Situ Generation of Carbenes: A General and Versatile Platform for Organocatalytic Living Polymerization", *Journal of the American Chemical Society*, vol. 125, pp. 3046-3056, 2003.
- [5] D. Bourissou, B. Martin-Vaca, A. Dumitrescu, M. Graullier and F. Lacombe, "Controlled Cationic Polymerization of Lactide", *Macromolecules*, vol. 38 (24), pp. 9993–9998, 2005.
- [6] Z. Zhu, X. Deng and C. Xiong, "Anionic ring-opening polymerization", *Indian Journal of Chemistry*, vol. 40B, pp. 108-112, June 2001.
- [7] J.P. Runt, I.R. Harisson, E. Manias, S.P. Siedlecki, G.L. Mesing, Solid-state structure and dynamics of lactide copolymers and blends, The Pennsylvania State University The Graduate School Department of Materials Science and Engineering, 2004.
- [8] A. Kowalski, A. Duda, S. Penczek, "Kinetics and mechanism of cyclic esters polymerization initiated with tin(II) octoate", *Macromolecular Rapid Communication*, vol. 19, pp. 567-572, 1998.
- [9] Lj. Nikolic, I. Ristic, B. Adnadjevic, V. Nikolic, J. Jovanovic and M. Stankovic, "Novel Microwave-Assisted Synthesis of Poly(D,L-lactide): The Influence of Monomer/Initiator Molar Ratio on the Product Properties", *Sensors*, vol. 10 (5), pp. 5063-5073, 2010.
- [10] P. Singla, P. Kaur, R. Mehta, D. Berek, S.N. Upadhyay, "Ring-Opening Polymerization of Lactide Using Microwave and Conventional Heating", *Procedia Chemistry*, vol. 4, pp. 179-185, 2012.

A Candidate Material for Mercury Control in Energy Production Processes: Carbon Foams Loaded with Gold

CRISTINA ANTUÑA-NIETO, ELENA RODRÍGUEZ, M. ANTONIA LÓPEZ-ANTÓN, ROBERTO GARCÍA & M. ROSA MARTÍNEZ-TARAZONA

Abstract Coal combustion power plants are among the main anthropogenic sources of mercury to the environment. It represents the first emission source of mercury in Europe and the second in the world. Among the different possibilities that can be posed to reduce these emissions, this work focuses on the use of regenerable sorbents to capture gaseous mercury species present in flue gases. The use of regenerable sorbents in coal power plants would not only allow the objective of reducing mercury emissions, but also recovering the mercury without producing any toxic wastes. Regenerable sorbents were designed for use at the end of the cycle where most oxidized mercury species have been already captured and the main remaining species would be gaseous elemental mercury. The sorbents were prepared by impregnation of activated carbon foams with different amounts of gold nanoparticles. The sorbent and the process should facilitate gold recovery when the sorbent is exhausted. Mercury retention capacity was evaluated in a laboratory scale device. The results showed high mercury retention over several cycles of regeneration of the sorbent.

Keywords: • mercury • carbon foam • regeneration • gold • PLA •

CORRESPONDENCE ADDRESS: Cristina Antuña-Nieto, Schlp., Instituto Nacional del Carbón (CSIC), C/Francisco Pintado Fe 26, 33011 Oviedo, Spain, e-mail: cristina.a.n@incar.csic.es. Elena Rodríguez, Ph.D., Researcher, Instituto Nacional del Carbón (CSIC), C/Francisco Pintado Fe 26, 33011 Oviedo, Spain, e-mail: elena@incar.csic.es. M. Antonia López-Antón, Ph.D., Researcher, Instituto Nacional del Carbón (CSIC), C/Francisco Pintado Fe 26, 33011 Oviedo, Spain, e-mail: marian@incar.csic.es. Roberto García, Ph.D., Researcher, Instituto Nacional del Carbón (CSIC), C/Francisco Pintado Fe 26, 33011 Oviedo, Spain, e-mail: robo@incar.csic.es. M. Rosa Martínez-Tarazona, Ph.D., Researcher, Instituto Nacional del Carbón (CSIC), C/Francisco Pintado Fe 26, 33011 Oviedo, Spain, e-mail: rmtarazona@incar.csic.es.

1 Introduction

The high toxicity of mercury to humankind and ecosystems is well known. Moreover, once mercury is emitted into the atmosphere, it can travel thousands of miles, causing global contamination of plants, animals and humans. Coal combustion contributes to 85% of total gaseous mercury emissions into the air [1], as both elemental mercury (Hg^0) and oxidized mercury species (Hg^{2+}). These species are not only toxic by themselves but can also be transformed into methyl mercury (MeHg). Among all mercury compounds MeHg is the most dangerous. The highest concentrations of MeHg are detected in fish, which is one of the main sources of human exposure.

Although different compounds of mercury are formed during coal combustion, the most difficult species to be captured is Hg^0 , while Hg^{2+} is easier to be retained in the different gas cleaning systems already working in most coal combustion plants [2].

Mercury emissions from coal combustion could be controlled by pre-combustion and post-combustion strategies. The first one would involve preparing and cleaning the coal to reduce the amount of mercury while post-combustion technologies are mainly based on the capture of gaseous mercury species present in flue gases on solid sorbents [2].

Of the different possible sorbents already tested, zeolites and activated carbons are the most employed for mercury retention. They have been mainly designed for use by injection before the particle control systems. Zeolites display an excellent stability at high temperatures and in acid environments. However, activated carbons are the only materials that have already been tested at industrial scale. The drawback of activated carbon injection is the generation of a mixture of carbon sorbent and fly ash waste that is disposed on landfills, because its recovery for fly ash reuse is very limited by the presence of carbon particles.

Due to this problem, an attractive alternative to the injection of conventional solid sorbents is the use of regenerable sorbents, and those impregnated with noble metals, which can amalgamate with Hg^0 , increasingly attract more interest [3]. Remarkable features of these sorbents are the possibility of regeneration, achieving a cost-effective cyclic operation [4]. The drawback to this technology is the large amounts of gold needed to coat the support.

The objective of this study is to obtain a sorbent doped with the minimum amount of gold to avoid price escalation. Coal-based carbon foam which has relatively good thermal, mechanical and electrical properties was used as the gold support.

2 Experimental Section

2.1 Activated foam preparation and characterization

The methodology followed to prepare the activated coal foam is described elsewhere [5]. A bituminous coal (Pondfork), grounded to $<212 \mu\text{m}$, was used as precursor, and chemical activation was carried out with ZnCl_2 . The coal was added to a solution of the chemical activator in ethanol and the suspension was stirred and heated at $60\text{--}75 \text{ }^\circ\text{C}$ for 2 h. Afterwards, the solvent was removed by heating at $105 \text{ }^\circ\text{C}$ for 2 days. The resultant mixture was loaded into a cone-trunk-shaped stainless steel reactor coated with aluminum foil. The loaded reactor was purged with argon to obtain an inert atmosphere, and subsequently the valves were closed to prevent the volatile matter from leaving the reactor during carbonization. The foaming process was carried out in a fluidized sand bed oven at the temperature of coal maximum fluidity ($450 \text{ }^\circ\text{C}$), for 2 h. The “green” foam thus obtained was carbonized in a horizontal tubular furnace by heating under argon flow at 5°C min^{-1} up to $500 \text{ }^\circ\text{C}$, keeping this temperature for 2 hours. In another experiment, an additional 20 hour-heat treatment step at $800 \text{ }^\circ\text{C}$ under CO_2 flow, was carried out.

After carbonization, the samples were washed with a 0.5 M HCl solution to eliminate any ZnCl_2 residue. Subsequent washing in Soxhlet extractors with Milli-Q water was carried out for 5 days to remove the chloride ions. Finally, the cleaned samples were dried at $110 \text{ }^\circ\text{C}$ overnight. The products were labeled as CF500 and CF800, respectively.

The resultant coal foams were ground to a size of $0.2\text{--}0.5 \text{ mm}$, and the porous texture was determined at 77 K by N_2 and CO_2 adsorption isotherms, respectively.

2.2 Method of Au impregnation

Au-loaded coal foam sorbents were prepared by a method based on the formation of Au colloids: the THPC/NaOH method. 0.8 mL of a tetrakis-(hydroxymethyl)phosphonium chloride (THPC) solution was added under stirring to a solution of 4 mL of H_2O with 0.6 mL of NaOH (0.2 M). Next, different volumes of $\text{HAuCl}_4\cdot 3\text{H}_2\text{O}$ (0.127 M) were added, to form an Au sol turning the solution brown. A suspension of 150 mg of foam in 8 mL of H_2O (treated for 15 min in an ultrasonic bath) was then added to the Au sol and stirred for 2 h. The resultant sorbent was filtered, washed, and dried. The THPC was removed by 3-hour heat treatment at $350 \text{ }^\circ\text{C}$, under argon flow (100 ml min^{-1}). [6]

2.3 Characterization of the coal foams impregnated with Au Nanoparticles

Temperature Programmed Desorption (TPD) was used for the identification of functionalized groups on the carbon surface, and volumetric adsorption of nitrogen at 77 K for the determination of surface area and porosity, using the Brunauer-Emmett-Teller (BET) method. The quantity of Au retained in the sorbent was determined by analyzing the Au that remains in the solution after impregnation, by inductively coupled plasma-

mass spectrometry (ICP-MS). The Au distribution and particle size of the Au impregnated activated carbon surface were analyzed by scanning electron microscopy (SEM-EDX). Speciation on Au on the surface was identified by X-ray photoelectron spectroscopy (XPS).

2.4 Experimental device for mercury retention

The laboratory device used for Hg retention is shown in Figure 1. It consists of a glass reactor heated by a furnace. In a typical experiment, 100-150 mg of sorbent was placed inside the reactor. Hg⁰ in gas phase, obtained from a permeation tube, was passed through the sorbent bed in a CO₂+N₂ (0.2 0.5 L min⁻¹ of N₂ and 0.3 0.5L min⁻¹ of CO₂) stream. The temperature of the reactor was kept at 40 °C and the gas lines at 70 °C to avoid condensation of the mercury. The stream out was analyzed by a continuous Hg⁰ monitor (VM3000) to obtain the Hg⁰ adsorption curves. A sorbent Dowex ion exchange resin bed, is placed before the Hg⁰ monitor to retain the oxidized mercury (Hg²⁺) that was analyzed afterwards.

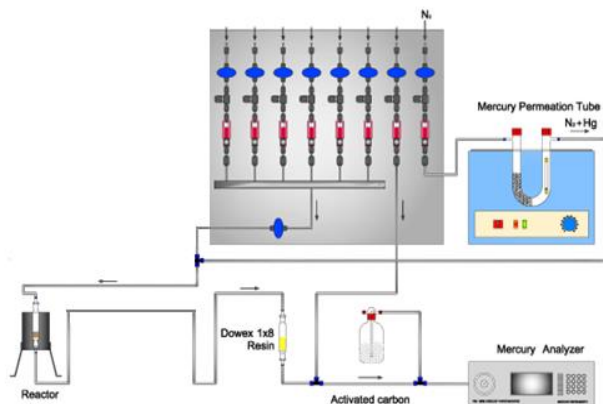


Figure 1. Experimental device for Hg capture experiments.

3 Results and Discussion

3.1 Characterization of the activated carbon foam

Treatment at 800 °C in a CO₂ atmosphere of the foam obtained at 500 °C slightly modifies the textural properties of the material (Table1), but mainly alters the surface chemistry. The analysis by TPD indicates that the activated coal foam CF500 possesses a high proportion of phenolic groups on its surface. In contrast, the one subjected to the treatment at 800 °C (CF800) mainly displays carboxyl and quinone groups.

Table 1. Surface area and micropore volume of the activated coal foam supports

Sorbent	Surface area (cm ² g ⁻¹)	Micropore vol. (cm ³ g ⁻¹)
CF500	880	0.36
CF800	738	0.28

3.2 Au Deposition on the supports

Sorbents with contents of Au of 1 and to 5% were prepared.

According to SEM analysis, the average size of Au particles increases with the quantity of Au added (Table 2). Figures 2 and 3 show the SEM micrographs of CF800-1 and CF800-5 samples. In these micrographs, it can be observed that the distribution of Au particles is more homogeneous in the sample with the lowest Au content. An increase in the concentration of Au widens the range of particle sizes.

Table 2. Content and particle size of gold

Sorbent	Au (wt %)	Au size (nm)
CF500-1	1	5
CF500-5	5	55
CF800-1	1	10
CF800-5	5	80

3.3 Hg retention on sorbents impregnated with Au nanoparticles

The Hg⁰ adsorption curves and Hg retention capacities for the raw sorbents and the Au-coated sorbents are given in Figure 4 and Table 3, respectively. The curves represent the outlet/inlet Hg⁰ concentration ratio (C_{out}/C_{in}) versus time. The Hg retention capacities were calculated at the breakthrough time (t_b), which is defined as the time at which a sample retains Hg with 100% efficiency. Moreover, results of mercury oxidation after 1000 min of retention are also given in Table 3. After 1000 min, at least for CF500 samples, saturation was already reached. Apparently, insignificant heterogeneous mercury oxidation takes place on sorbents CF500 after the breakthrough time, but it is slightly higher for sorbents CF800.

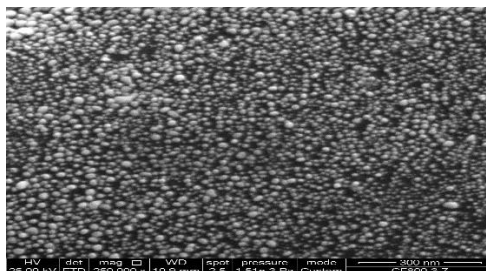


Figure 2. SEM micrograph of CF800-1

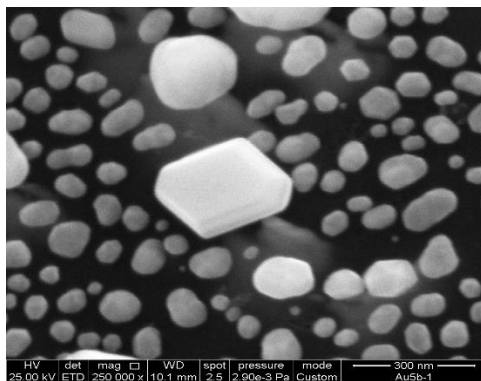


Figure 3. SEM micrograph of CF800-5

The retention capacity of Hg^0 on the activated carbon foam before being loaded with Au is as low as $17 \mu\text{g g}^{-1}$, significantly increasing in the impregnated carbon foams. The Au-loaded foams exhibited retention values around $100 \mu\text{g g}^{-1}$, with 100% efficiency (Table 3). However, the results show that an increase in Au content does not necessarily favour the retention of mercury. In both CF500 and CF800, Hg retention decreases when Au content increased from 1 to 5%. This behaviour can be explained with the distribution of gold on the surface observed by the SEM analysis. SEM micrographs revealed that Hg retention improves when the particle diameters are lower and when the gold distribution is more homogeneous, even with low Au concentrations. On the other hand, the formation of gold aggregates, which might reduce the accessibility of Hg [7, 8], corresponds to the highest Au concentration.

Table 3. Mercury retention capacity and efficiency

Sorbent	100% efficiency		t = 1000 min
	Hg retention ($\mu\text{g g}^{-1}$)	tb (min g^{-1})	Hg oxidized (%)
CF500-1	102	1521	0,6
CF500-5	70	1455	0,6
CF800-1	119	1865	8,8
CF800-5	98	1840	4,2

According to the results obtained (Table 3), it is observed that the carbon foams treated at 800°C show greater breakthrough time (tb) than the ones treated at 500°C .

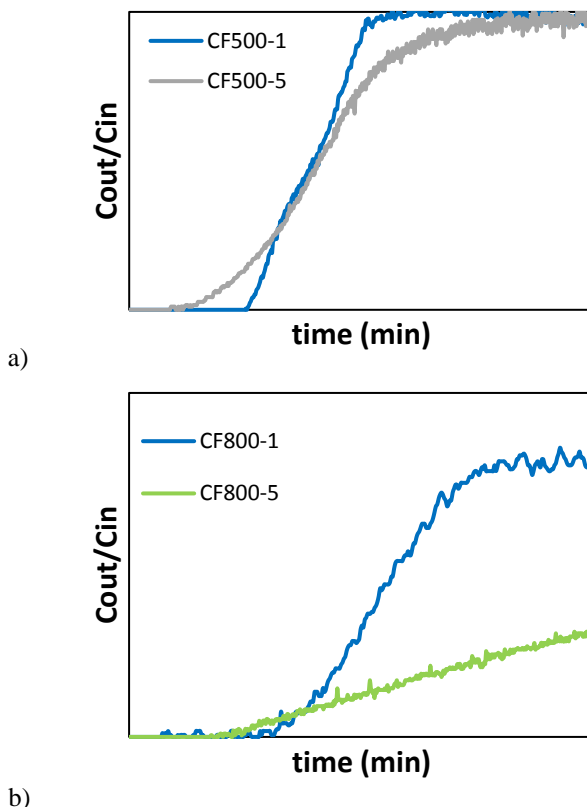


Figure 4. Curves of mercury adsorption in (a) CF500 samples and (b) CF800 samples

4 Conclusion

The evaluation of the performance of nanodispersed Au-loaded coal foam sorbents in an atmosphere containing CO₂ and N₂ demonstrates the different behaviour of sorbents prepared with different concentrations of gold. Hg retention is mainly controlled by the homogeneity and deposition of the Au particles on the carbonaceous support rather than the amount of Au. The distribution of Au particles and its accessibility affect the efficiency of Hg capture. Moreover, and although these results need to be confirmed, carboxylic and phenolic groups and microporosity may also have an influence on mercury capture on the support

However, the quantity of mercury increases with the quantity of Au. In the search for a suitable balance between the amount of Au employed and the amount of Hg retained, it can be concluded that the best samples for this application are CF800-1. In future works,

the sorbents with the best efficiency and Hg retention capacity will be tested in different atmospheres and evaluated for several cycles.

Acknowledgements

The authors acknowledge financial support, through research projects CTQ2014-58110-R and GRUPIN14-031.

References

- [1] G.Q. Chen, J.S. Li, B. Chen, C. Wen, Q. Yang, A. Alsaedi and T. Hayat, “An overview of mercury emissions by global fuel combustion: The impact of international trade”, *Renewable and Sustainable Energy Reviews*, vol. 65, pp. 345–355, Nov. 2016.
- [2] J. Rodríguez-Pérez, M. A. López-Antón, M. Díaz-Somoano, R. García and M. R. Martínez-Tarazona, “Regenerable sorbents for mercury capture in simulated coal combustion flue gas”, *Journal of Hazardous Materials*, vol. 260, pp. 869–877, Sept. 2013.
- [3] M. A. López-Antón, N. Fernández-Miranda and M. R. Martínez-Tarazona, “The application of regenerable sorbents for mercury capture in gas phase”, *Environmental Science and Pollution Research*, vol. 23, pp. 24495–24503, Dec. 2016.
- [4] F. Scala, C. Anaclella and S. Cimino, “Characterization of a regenerable sorbent for high temperature elemental mercury capture from flue gas”, *Fuel*, vol. 108, pp. 13–18, Jan. 2011.
- [5] E. Rodríguez and R. García, “Microporosity Development in Coal-Based Carbon Foams”, *Energy & Fuels*, vol. 26, pp. 3703–3710, May 2012.
- [6] J. Rodríguez-Pérez, M. A. López-Antón, M. Díaz-Somoano, R. García and M. R. Martínez-Tarazona, “Development of gold nanoparticle-doped activated carbon sorbent for elemental mercury”, *Energy & Fuels*, vol. 25, pp. 2022–2027, April 2011.
- [7] M. Levlin, E. Ikävalko and T. Laitinen, “Adsorption of Mercury on Gold and Silver Surfaces”, *Fresenius' Journal of Analytical Chemistry*, vol. 365, pp. 577–586, 1999.
- [8] M. Levlin, H.M. Niemi, P. Hautojärvi, E. Ikävalko and T. Laitinen, “Mercury Adsorption on Gold Surface Employed in the Sampling and Determination of Vaporous Mercury: A Scanning Tunneling Microscopy Study”. *Fresenius' Journal of Analytical Chemistry*, vol. 355, pp 2–9, 1996.

Carbon-Based Sorbents Impregnated with Iron Oxides for Removing Mercury in Energy Generation Processes

JAIME TROBAJO, ELENA RODRÍGUEZ, ROBERTO GARCÍA, M. ANTONIA LÓPEZ-ANTÓN & M. ROSA MARTÍNEZ-TARAZONA

Abstract Gas-phase mercury emissions into the atmosphere through fossil fuel combustion, is a matter of important environmental concern. Several technologies have been studied and proposed to tackle this problem but none of them is mature enough from a commercial point of view. Carbon-based sorbents impregnated with sulphur or halogens, have demonstrated good performance for mercury capture by injection. However, they are not regenerable. The purpose of this work is to evaluate the performance of carbon-based sorbents impregnated with different iron oxides, at different concentrations, to capture elemental mercury in gas phase. These sorbents were prepared by several procedures and tested for their mercury removal capacity in a laboratory scale reactor at several temperatures and under different atmospheres. According to the results, there is reliance between the concentration of Fe in the sorbents and their adsorption capacity. It has been proved that a high surface area of the carbon support is a necessary but not sufficient condition. Among iron oxides, magnetite/maghemite shows a higher benefit for mercury removal capacity than goetite/hematite. Low temperatures (40-70 °C) give rise to a decrease of the mercury retention.

Keywords: • mercury • gas streams • iron • sorbents • energy generation processes •

CORRESPONDENCE ADDRESS: Jaime Trobajo, Schlp., Instituto Nacional del Carbón (CSIC), C/Francisco Pintado Fe 26, 33011 Oviedo, Spain, e-mail: jaime.rt@incar.csic.es. Elena Rodríguez, Ph.D., Researcher, Instituto Nacional del Carbón (CSIC), C/Francisco Pintado Fe 26, 33011 Oviedo, Spain, e-mail: elena@incar.csic.es. Roberto García, Ph.D., Researcher, Instituto Nacional del Carbón (CSIC), C/Francisco Pintado Fe 26, 33011 Oviedo, Spain, e-mail: robo@incar.csic.es. M. Antonia López-Antón, Ph.D., Researcher, Instituto Nacional del Carbón (CSIC), C/Francisco Pintado Fe 26, 33011 Oviedo, Spain, e-mail: marian@incar.csic.es. M. Rosa Martínez-Tarazona, Ph.D., Researcher, Instituto Nacional del Carbón (CSIC), C/Francisco Pintado Fe 26, 33011 Oviedo, Spain, e-mail: rmtarazona@incar.csic.es.

1 Introduction

Mercury is a well-known heavy metal toxic to humankind and ecosystems. In Europe, the major anthropogenic contribution of mercury into the environment is the release from coal-fired power plants. It is estimated that 7.5 Ton per year of mercury are emitted this way [1].

Mercury exists in three forms, namely, elemental mercury (Hg^0), oxidized mercury (Hg^{2+}), and particulate-bound mercury (Hg_p). The speciation of the mercury emitted dictates its subsequent lifetime and destiny in the atmosphere. For instance, Hg^{2+} is water-soluble and can easily enter water sources, in which is converted into methyl mercury (MeHg) by anaerobic bacteria. Of all mercury species MeHg is the most dangerous. Higher concentrations are detected in fish which is one of the main sources of human exposure. On the other hand, elemental mercury can be transported long distances in the atmosphere, where its toxic effects have global-scale impact [2].

Understanding the speciation of mercury throughout the combustion process is crucial to the design of effective mercury removal technologies. Another important point is the configuration of the facility, since the existent air pollution control devices (APCDs) can also influence the removal of mercury species. Thus, electrostatic precipitators (ESPs) are able to retain Hg_p share, whereas, 70-90% of oxidized mercury is removed through WFGD (wet flue gas desulfurization) units. Therefore, the most difficult specie to retain is elemental mercury [3][4]. From now on we will refer to Hg^0 simply as Hg.

Nowadays, there are several possibilities to address the problem of Hg adsorption, with a state-of-the-art overview having been already published [5][6]. Of all the different possibilities, activated carbons are the most employed for mercury retention. In particular, activated carbons impregnated with sulphur or halogens have proved very successful [7]. However, although highly effective, these sorbents are not regenerable.

It is widely known that Hg amalgamates with all the metals except iron. However, some studies show that iron-based sorbents could effectively remove Hg from a gas stream [8][9]. Although the exact mechanism under which the Hg is adsorbed in these materials is not fully understood [6], they represent an interesting alternative way to solve the Hg problem.

The aim of this research is to study the capacity of carbon based sorbents impregnated with iron oxides for Hg removal under different atmospheres and temperatures.

2 Experimental Section

The support used to prepare the sorbent was the commercial activated carbon Norit RB3. The extruded activated carbon as marketed was grounded between 0.2 and 0.5 mm for its impregnation and evaluation.

2.1 Impregnation and preparation

The impregnation with iron was performed according to a previously developed procedure [10]. This method consists on wetting the solid with a dissolution of $\text{Fe}(\text{NO}_3)_3 \cdot 9\text{H}_2\text{O}$ followed by a thermal treatment, which gives rise to the formation of iron oxides hematite ($\alpha\text{-Fe}_2\text{O}_3$) and goethite ($\alpha\text{-FeO}(\text{OH})$) on the surface .

Three techniques (namely A, C and D), were used searching for the best dispersion of the iron species on the surface. They were all performed by the same method [10], the difference being the way of addition of the Fe compound. “A” consists of the ultrasonic treatment of a suspension of the activated carbon in a solution of $\text{Fe}(\text{NO}_3)_3 \cdot 9\text{H}_2\text{O}$. “C” is based on an incipient impregnation of the activated carbon with $\text{Fe}(\text{NO}_3)_3 \cdot 9\text{H}_2\text{O}$ dissolved on ethanol. “D” is the same as “C”, but heating the activated carbon under vacuum between each incipient impregnation.

Finally, to transform the iron oxide species of hematite/goethite, obtained by this impregnation, to magnetite/maghemite, the sorbent was heated at 800 °C for an hour in an inert atmosphere.

2.2 Characterization

The homogeneity of iron distribution on the surface of the activated carbon was evaluated by Scanning Electron Microscopy (SEM). To calculate the BET area a nitrogen adsorption-desorption method at 77 K was used. The iron oxides were identified by X-ray diffraction (XRD) using Cu K α radiation as X-ray source. In magnetite ($\text{FeO} \cdot \text{Fe}_2\text{O}$ or Fe_3O_4), iron is in +2 and +3 oxidation states, whereas in hematite (Fe_2O_3), it is in +3. Magnetite has higher iron content and commonly shows an octrahedral crystal structure, while hematite has a rhombododecahedral crystal structure.

2.3 Experimental device for mercury retention

The laboratory device used for Hg retention is shown in Figure 1.

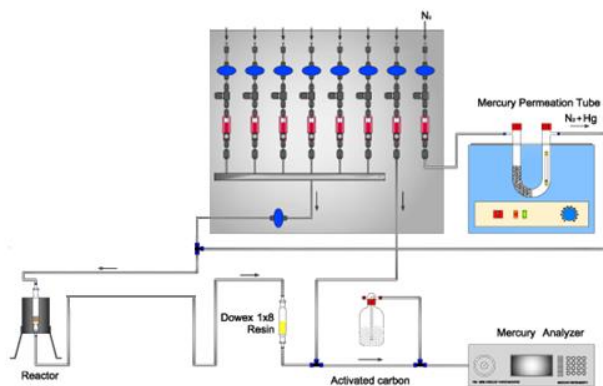


Figure 1. Experimental device for mercury adsorption evaluation

It consists of a glass reactor heated by a furnace. In a typical experiment, ~200 mg of sorbent was placed inside the reactor. The gas phase Hg^0 is obtained from a permeation tube, carried with a N_2 stream of $200 \text{ ml} \cdot \text{min}^{-1}$. In addition, more N_2 , air or O_2 (if not specified the experiments are performed on an air atmosphere) was added to the system, up to $500 \text{ ml} \cdot \text{min}^{-1}$, before reaching the sorbent. The temperature of the reactor was kept at $140 \text{ }^\circ\text{C}$, except in the experiments conducted to study the influence of temperature. All the gas lines were heated to avoid mercury condensation. At the exit of the reactor a bed of Dowex ion exchange resin was placed. The exit stream is analyzed by a continuous Hg^0 emission monitor (VM3000) that was also used to obtain the Hg adsorption curves. The mercury analyzer needs at least $2.5 \text{ l} \cdot \text{min}^{-1}$ of gas, so a stream of $2.0 \text{ l} \cdot \text{min}^{-1}$ of air was added to the reactor stream at the entrance of the detection system. The duration of all the experiments was approximately 24 hours.

3 Results and Discussion

The identification of samples and the conditions considered in each sub-section are shown in Table 1.

As identified by SEM, the most homogenous sorbent is the one obtained by treatment D.

Table 1. Samples used for the different experiments.

Section	Samples treatment	Variable of study
3.1	D	Conc. of Fe
3.2	D with a 10% of iron oxides.	Behaviour with different oxides
3.3	D with a 10% of magnetite/maghemite species	Temperature
3.4	D with a 10% of magnetite/maghemite species	Influence of O ₂

The sorbents can capture Hg⁰ in two main ways, by straight absorbance, or after oxidation. In the experiments of this study, oxidized mercury was never identified in the resin at the outlet of the reactor. Consequently, if oxidation occurred, all oxidised mercury would have been retained in the sorbent. For this reason in the Hg balances we will refer only to total Hg adsorbed by the sorbents.

3.1 Influence of iron concentration

In order to elucidate the influence of iron content on Hg retention capacity, the activated carbon impregnated with 12% and 35% of Fe was compared with the original RB3. The results are shown in Figure 2.

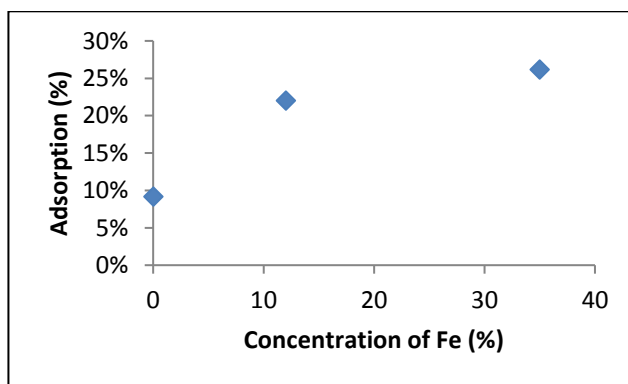


Figure 2. Hg removal in sorbents with different Fe content.

The Hg removal capacity or adsorption increases in a non-linear way with the concentration of Fe present on the sorbent.

The activated carbon RB3 has a BET surface of 1183 m²·g⁻¹. When iron impregnated sorbents were prepared using activated carbons with lower BET area (from 50 to 400

$\text{m}^2 \cdot \text{g}^{-1}$) the adsorption capacity was insignificant in all cases, suggesting that a high surface area is a necessary but not enough condition for Hg removal capacity

3.2 Influence of iron oxide

As mentioned in section 2.1, the sorbents impregnated with Fe were subjected to a heat treatment to transform goethite/hematite to magnetite/maghemite. In previous research [11], it was unclear if the magnetic behavior could have an impact on Hg removal capacity. The magnetic behavior varies from goethite/hematite (weakly ferromagnetic or antiferromagnetic) to magnetite/maghemite (ferromagnetic). From the results of this work it cannot be inferred if the magnetic behavior of the oxides has an influence on the retention of mercury. However, the results (Figure 3) indicate that Hg retention is significantly higher with magnetite/maghemite.

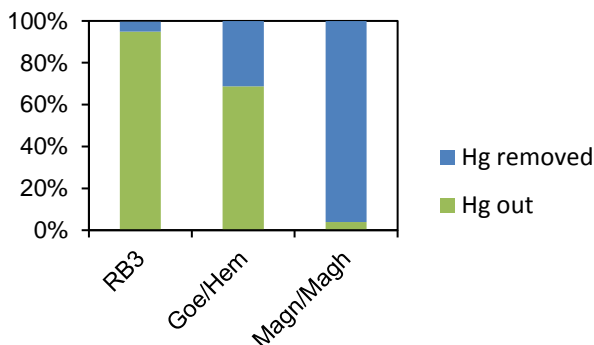


Figure 3. Hg removal balances in sorbents having different iron oxides.

Clearly the heat-treated sorbent is much more efficient on removing Hg from the stream (up to 95%). However, the exact mechanism under which this adsorption takes place is not yet fully understood [6]. These results suggest a new promising line of investigation in relation to iron oxides behavior and its influence on Hg removal capacity.

3.3 Influence of temperature

In previous works [12], other authors have evaluated the influence of temperature and the mechanism of Hg adsorption (physisorption or chemisorption), and concluded that below 75 °C the dominant mechanism is physisorption while above 75 °C chemisorption is dominant.

In this study, the removal capacity at several temperatures, 40 °C, 90 °C and 140 °C was evaluated in order to clarify this point, and the results are shown in Figure 4.

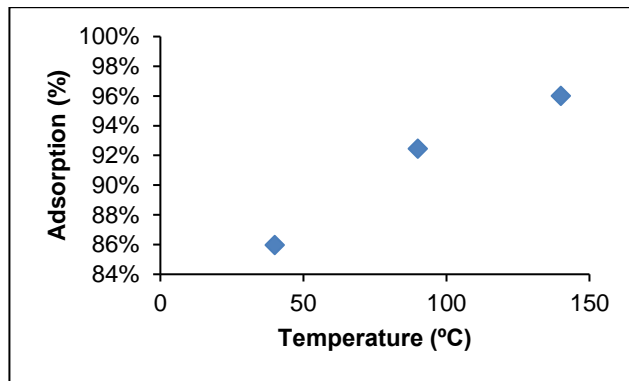


Figure 4. Influence of temperature on Hg removal capacity.

As we can see, higher temperatures favor Hg adsorption. This could indicate that the main mechanism behind this iron impregnated sorbent is chemisorption [12]. However, even at lower temperatures the sorbent keep a high Hg removal capacity.

3.4 Influence of gas composition

The percentage of Hg removal in different atmospheres -air (as in all previous experiments), inert (N_2) and O_2 - are shown in Figure 5.

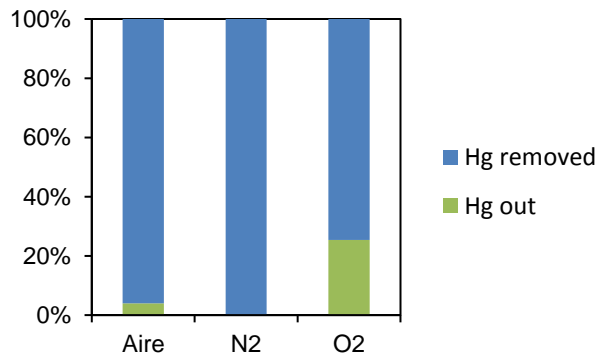


Figure 5. Hg retention balances in different atmospheres.

According to previous studies, O_2 should improve Hg removal capacity at least above 100 °C on the chemisorption region [12][13][14]. These experiments were performed at 140 °C and, then, an increase of the Hg removed with O_2 and a decrease with N_2 should be expected. However, we have found the opposite. The higher the O_2 concentration in the gas stream, the lower the adsorption of Hg (Figure 6).

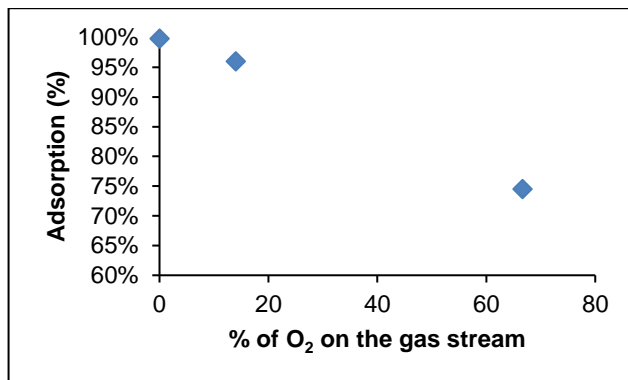


Figure 6. Influence of O₂ concentration on Hg removal capacity.

It is well known that the specific mechanism under which activated carbons adsorb Hg [6] is not yet understood, and neither is the effect of iron on its surface. The fact that O₂ is counterproductive to Hg removal in the iron oxides impregnated could indicate that the mechanism of mercury retention in these sorbents is not exclusively chemical nor physical: reactions in the presence of iron and subsequent adsorption in the carbon could be taking place.

4 Conclusions

The retention of mercury on activated carbons impregnated with iron oxides was satisfactory: Hg removal capacities higher than 90% were achieved with sorbents without sulfur. Reliance between Fe concentration and Hg removal capacity was found, although this reliance is non-linear and has decreasing efficiency. It was proven that a high surface area is a necessary but not sufficient condition. Among the two species of iron oxides tested, magnetite/maghemite displays much higher Hg removal capacity: 90% against a 30% obtained with goethite/hematite.

While temperature experiments seem to indicate that a chemisorption process is predominant, the O₂ concentration studies do not provide conclusive results.

Acknowledgements

The authors acknowledge financial support, through research projects CTQ2014-58110-R and GRUPIN14-031.

References

- [1] UNEP, "The Global Mercury Assessment," 2013.
- [2] D. Wentz, M. Brigham, L. Chasar, M. Lutz, and D. Krabbenhoft, *Mercury in the Nation's Streams — Levels, Trends, and Implications Circular 1395*. 2014.

- [3] J. Rodríguez-Pérez, M. A. López-Antón, M. Díaz-Somoano, R. García, and M. R. Martínez-Tarazona, “Regenerable sorbents for mercury capture in simulated coal combustion flue gas,” *J. Hazard. Mater.*, vol. 260, pp. 869–877, 2013.
- [4] C. Acuña-Caro, K. Brechtel, G. Scheffknecht, and M. Braß, “The effect of chlorine and oxygen concentrations on the removal of mercury at an FGD-batch reactor,” *Fuel*, vol. 88, no. 12, pp. 2489–2494, 2009.
- [5] T. Abbas, M. I. Abdul Mutalib, and M. Azmi Bustam, “Developments in Mercury Removal from Natural Gas - A Short Review,” *Appl. Mech. Mater.*, vol. 625, pp. 223–228, 2014.
- [6] J. Wilcox *et al.*, “Mercury adsorption and oxidation in coal combustion and gasification processes,” *Int. J. Coal Geol.*, vol. 90–91, pp. 4–20, 2012.
- [7] W. Liu, R. D. Vidić, and T. D. Brown, “Optimization of sulfur impregnation protocol for fixed-bed application of activated carbon-based sorbents for gas-phase mercury removal,” *Environ. Sci. Technol.*, vol. 32, no. 4, pp. 531–538, 1998.
- [8] J. Wang, Y. Zhang, L. Han, L. Chang, and W. Bao, “Simultaneous removal of hydrogen sulfide and mercury from simulated syngas by iron-based sorbents,” *Fuel*, vol. 103, pp. 73–79, 2013.
- [9] S. Wu, M. Azhar Uddin, and E. Sasaoka, “Characteristics of the removal of mercury vapor in coal derived fuel gas over iron oxide sorbents,” *Fuel*, vol. 85, no. 2, pp. 213–218, 2006.
- [10] R. Dobrowolski and M. Otto, “Preparation and evaluation of Fe-loaded activated carbon for enrichment of selenium for analytical and environmental purposes,” *Chemosphere*, vol. 90, no. 2, pp. 683–690, 2013.
- [11] G. A. Norton, H. Yang, R. C. Brown, D. L. Laudal, G. E. Dunham, and J. Erjavec, “Heterogeneous oxidation of mercury in simulated post combustion conditions,” *Fuel*, vol. 82, no. 2, pp. 107–116, 2003.
- [12] S. Kwon, E. Borguet, and R. D. Vidić, “Impact of surface heterogeneity on mercury uptake by carbonaceous sorbents under UHV and atmospheric pressure,” *Environ. Sci. Technol.*, vol. 36, no. 19, pp. 4162–4169, 2002.
- [13] T. Liu, L. Xue, X. Guo, and C. G. Zheng, “DFT study of mercury adsorption on α -Fe₂O₃ surface: Role of oxygen,” *Fuel*, vol. 115, pp. 179–185, 2014.
- [14] B. Hall, P. Schager, and J. Weesmaa, “The homogeneous gas phase reaction of mercury with oxygen, and the corresponding heterogeneous reactions in the presence of activated carbon and fly ash,” *Chemosphere*, vol. 30, no. 4, pp. 611–627, 1995.

Facile Fabrication of a Mesoporous Iridium Oxide Film for Efficient Electrocatalytic Water Oxidation

DEBRAJ CHANDRA, TSUBASA SATO, RYOUCHI TAKEUCHI, DONG LI, KENJI SAITO, TATSUTO YUI & MASAYUKI YAGI

Abstract A new transparent IrO_x catalyst film for water oxidation was fabricated on a FTO electrode by a simple drop-cast technique employing an Ir-precursor complex solution containing a triblock copolymer, “Pluronic F127” as a surfactant template. The IrO_x film was composed of finely distributed and well-connected nanoparticles (*ca.* 2-5 nm) assembly, comprising the disordered mesoporous nanostructure. Surface area (75 m² g⁻¹) of the mesoporous IrO_x film calcined at 400 °C was 3.6 times higher than the untemplated IrO_x film of discrete nanoparticles. The mesoporous IrO_x electrode affords 1.9 times higher O₂ evolution during the electrocatalytic water oxidation relative to an untemplated IrO_x film. The higher water oxidation activity of the mesoporous IrO_x electrode is ascribed to the large surface-to-mass ratio to provide the increased number of active Ir-sites at the electrolyte-IrO_x interface and to the matrix of interconnected nanoparticles to afford fast electron transport in the film, as well as to the increased intrinsic catalytic activity of the Ir-sites.

Keywords: • iridium oxide • nanostructure engineering • mesoporous • electrocatalysis • water oxidation •

CORRESPONDENCE ADDRESS: Debraj Chandra, Ph.D., Postdoctoral Researcher, Niigata University, Faculty of Engineering, 8050 Ikarashi-2, Niigata, 950-2181, Japan, e-mail: debraj.chandra@gs.niigata-u.ac.jp. Tsubasa Sato, MS, Student, Niigata University, Faculty of Engineering, 8050 Ikarashi-2, Niigata, 950-2181, Japan, e-mail: f15b019e@mail.cc.niigata-u.ac.jp. Ryouchi Takeuchi, MS, Student, Niigata University, Faculty of Engineering, 8050 Ikarashi-2, Niigata, 950-2181, Japan, e-mail: f16b016e@mail.cc.niigata-u.ac.jp. Dong Li, Ph.D., Postdoctoral Researcher, Niigata University, Faculty of Engineering, 8050 Ikarashi-2, Niigata, 950-2181, Japan, e-mail: ldagcy@126.com. Kenji Saito, Ph.D., Assistant Professor, Niigata University, Faculty of Engineering, 8050 Ikarashi-2, Niigata, 950-2181, Japan, e-mail: ksaito@eng.niigata-u.ac.jp. Tatsuto Yui, Ph.D., Associate Professor, Niigata University, Faculty of Engineering, 8050 Ikarashi-2, Niigata, 950-2181, Japan, e-mail: yui.t@eng.niigata-u.ac.jp. Masayuki Yagi, Ph.D., Professor, Niigata University, Faculty of Engineering, 8050 Ikarashi-2, Niigata, 950-2181, Japan, yagi@eng.niigata-u.ac.jp.

1 Introduction

In the quest for development of artificial photosynthesis to provide renewable and clean energy systems for the future, water oxidation catalysis has been intensively studied.[1-4] The critical challenge of water oxidation catalysis is to negotiate its sluggish kinetics for oxygen evolution. In pursuit of this, molecular complexes of precious metals such as ruthenium and iridium and their oxides along with inorganic materials derived from other transition metals have been investigated in electrocatalytic water oxidation.[5-9] So far, iridium oxide (IrO_x)-based nanomaterials have been extensively studied in both electrochemical[9-14] and photoelectrochemical[15, 16] systems for water oxidation. Enormous efforts have been devoted to enhance the catalytic performance by increasing its accessible surface and controlling phase/composition of the nanostructures.[13, 14]

IrO_x nanoparticle films have been predominantly utilized for electrocatalytic water oxidation because of their ease of fabrication as electrodes on various electro-conducting substrates.[9-13] However, in most of the instances IrO_x nanoparticle films are associated with low/moderate surface area. Recently, mesoporous IrO_x nanostructures as electrocatalyst films gain significant attention owing to their large internal surface area.[14, 17-19] The surfactant-templated strategy has provided one of the suitable ways for fabrication of mesoporous metal oxides.[20, 21] However, the surfactant-templated IrO_x nanostructures are restricted in only two examples of spherical[19] and 2D-hexagonal[14] mesoporous structure formed by block copolymer templates. Our aim is to develop a simple technique for fabrication of an efficient electrocatalyst film of IrO_x nanostructures. Herein, we report facile fabrication of a new mesoporous IrO_x film formed by assembly of nanoparticles (ca. 2-5 nm) to provide high surface area. A transparent IrO_x-coated layer was obtained by simple drop-cast of very low concentration solution of Ir-precursor complex and a triblock copolymer template, “Pluronic F127” (EO₁₀₆PO₇₀EO₁₀₆; EO and PO represents poly(ethylene oxide) and poly(propylene oxide) units, respectively); then followed by calcination at 400 °C. The mesoporous IrO_x film improves performance for electrocatalytic water oxidation relative to a conventional nanoparticulate structure.

2 Experimental Section

2.1 Preparation of IrO_x Electrodes

In a typical synthesis, 0.4 g of Pluronic F127 (Sigma-Aldrich) was dissolved in 4 mL of a 0.1 M aqueous NaOH solution, and then to the solution 0.1 g (0.2 mmol) of K₂IrCl₆ (Wako Chemical Co.) was added under stirring at 40 °C. After stirring for 15 min, the resultant solution (pH ≈ 7) was diluted 100 times by water. 10 μL of this solution (corresponding to 5.2 nmol of Ir) was drop-casted on a FTO substrate (Asahi Glass Co.) with coated area of 0.8×1.25 cm and allowed to dry completely. The electrode was heated at 400 °C (1 °C min⁻¹) in flowing N₂ and maintained for 1 h, followed by calcination for 3 h in flowing O₂. The resultant sample was denoted as IrO_x-F127. The control sample

was prepared under the identical synthesis procedures except the addition of Pluronic F127, denoted as IrO_x-untemplate.

2.2 Structural characterization

Powder XRD patterns were recorded in a Rigaku MiniFlexII diffractometer using Cu K α ($\lambda = 1.54 \text{ \AA}$) radiation. Nitrogen sorption isotherms were measured using BELSORP-miniII. SEM and TEM images were recorded on JEOL, JSM-6500F and JEOL, JEM 2100F microscopes, respectively. The XRD, N₂ sorption and TEM data were taken of powders scratched off from the annealed films. Raman and FTIR spectra were recorded using a Horiba-Jobin-Yvon LabRAM HR and Jasco FT/IR-4200 spectrophotometer, respectively.

2.3 Electrochemical measurements

Electrochemical measurements were carried out by an electrochemical analyzer (Hokutodenkou HZ-7000). A two-compartment electrochemical cell with three-electrode-type system has been employed by using an IrO_x/FTO electrode as a working electrode and an Ag/AgCl reference electrode in one compartment and a Pt wire counter electrode in the other compartment. The potentials were expressed as the values versus Ag/AgCl unless otherwise noted. An aqueous 0.1 M phosphate solution (pH = 6.8) was used as an electrolyte. Cyclic voltammograms (CVs) were recorded at a scan rate of 50 mV s⁻¹ between the ranges of -0.4 V and 1.5 V. Tafel plots were derived using a linear sweep voltammogram (LSV) measured at a scan rate of 0.5 mV s⁻¹ between the ranges of 0.8 V and 1.1 V. Electrocatalytic water oxidation was conducted at 1.2 V of applied potential for 1 h. The amounts of H₂ and O₂ evolved during electrocatalysis were analyzed in the gas phases (headspace regions) of the counter and working electrode compartments, respectively on a Shimadzu, GC-8A gas chromatograph.

3 Results and Discussion

3.1 Characterization of Nanostructure

The small-angle XRD patterns (Fig. 1) of IrO_x-F127 sample calcined at 400 °C showed single diffraction peak, suggesting the formation of nanostructure IrO_x materials with no long range mesoscopic ordering. However, the XRD peak is disappeared above 450 °C, depicting degradation of the mesostructure. The *d*-spacing value calculated from XRD maxima is 10.5 nm. The IrO_x-untemplate film shows no detectable XRD peak, signifying any mesostructure was not yielded without Pluronic F127 in the precursor solution. The wide angle XRD patterns and Raman spectra of IrO_x-F127 film revealed an amorphous phase of oxide framework up to 400 °C, which is crystallized to tetragonal phase of the IrO₂ (JCPDS: 150870) after calcination over 450°C.

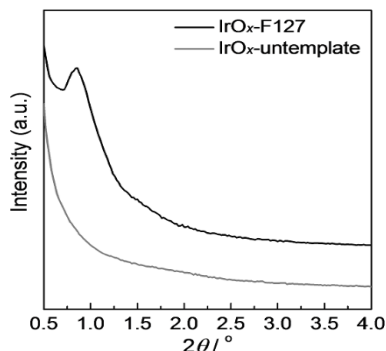


Figure 1. Small-angle XRD patterns of IrO_x samples calcined at 400 °C

The SEM image (Fig. 2a) of the IrO_x-F127 film revealed a large domain of the FTO surface is covered by a uniform and thin coating layer of deposited IrO_x over several micrometer scales. However, a significant fraction on the FTO surface shows no observable coating layer except a few discrete depositions, which is primarily attributed to the lower Γ_{cov} (5.2 nmol cm⁻²) of Ir-species compared to our prior report of 2D-hexagonal mesoporous IrO₂ film (Γ_{cov} , ~30 nmol cm⁻²) by spin coating method.[14] More uniformly deposited IrO_x layer was observed with gradual increase of Γ_{cov} by repeated coating. TEM image (Fig. 2b) of the calcined film at 400 °C showed disordered arrangement of mesopores of ≤ 5 nm, which agrees well with the pore diameter obtained from N₂ sorption analysis. A close look into the image revealed that assembly of finely distributed and well-connected nanoparticles (*ca.* 2-5 nm) compose the framework of the mesoporous nanostructure. In a contrast, the TEM image of the untemplated film revealed discrete nanoparticles (*ca.* 2-5 nm). Moreover, a large part of nanoparticles became aggregated to form big secondary particles (≥ 15 nm). The BET surface area of the IrO_x-F127 sample was observed to be 75 m² g⁻¹ (pore volume, 0.25 cm³ g⁻¹), which is comparable with mesoporous silica prepared by block copolymer template,[22] considering the high density of the IrO₂ (11.66 g cm⁻³; tetragonal phase). This is in contrast to the low BET surface area of 21 m² g⁻¹ of IrO_x-untemplate.

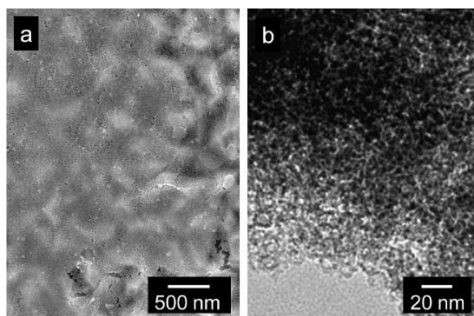


Figure 2. (a) SEM and (b) TEM images of IrO_x-F127 film calcined at 400 °C

3.2 Electrocatalytic properties

Electrocatalytic water oxidation were examined employing neutral conditions (0.1 M phosphate solution; pH = 6.8) considering application to artificial photosynthesis. CV in the potential window of 0 to 0.9 V showed the broad anodic peak at ≈ 0.25 V and ≈ 0.55 V (Fig. 3a), assigned to oxidation of Ir^{III}/Ir^{IV} and Ir^{IV}/Ir^V redox pairs of the IrO_x, respectively according to literature.[10, 12] It is difficult to reliably analyze the amount of electroactive Ir-sites because of the fused Ir^{III}/Ir^{IV} and Ir^{IV}/Ir^V redox pairs. However, the relative amounts (Γ_{ea}) of electroactive Ir-sites were estimated from the entire anodic current area from 0.09 to 0.80 V.[13] The Γ_{ea} for IrO_x-F127 (1.0) is a little higher relative to IrO_x-untemplate (0.96). This suggests that the electroactivity of the Ir-sites is a little enhanced by the mesoporous structure of interconnected nanoparticles of IrO_x-F127 film compared with the IrO_x-untemplate film having discrete nanoparticles of similar dimension (ca. 2-5 nm).

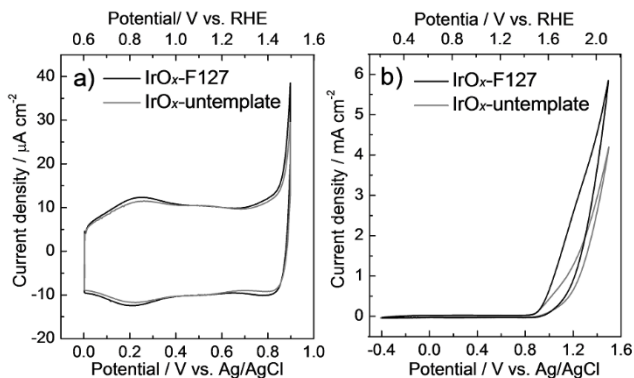


Figure 3. CVs of IrO_x electrodes calcined at 400 °C in potential windows between (a) 0 and 0.9 V and (b) -0.4 and 1.5 V vs Ag/AgCl

In Fig. 3b, CV in the wide potential range window of -0.4 to 1.5 V concomitantly exhibited anodic current due to water oxidation over ≈ 0.88 V (pH = 6.8). The catalytic current density ($I_{\text{cat}} / \text{mA cm}^{-2}$) at 1.5 V for the IrO_x-F127 (5.9 mA cm⁻²) is 1.4 times higher than that for the IrO_x-untemplate (4.2 mA cm⁻²), suggesting the increased intrinsic catalytic activity of the Ir-sites as well as the increased amount of Ir-sites for the IrO_x-F127. The onset potentials were defined as the potential for the catalytic current generation at 200 $\mu\text{A cm}^{-2}$, and the overpotentials (η / V) were calculated from the onset potential to be 0.30 V for IrO_x-F127, being relatively close to some most efficient IrO_x-based electrocatalysts ($\eta = 0.20$ -0.25 V).[10, 13, 17] The Tafel plots for water oxidation also revealed the significantly lower Tafel slope (45 mV dec⁻¹) for the IrO_x-F127 film than that (51 mV dec⁻¹) for the IrO_x-untemplate film, which is consistent with the observed I_{cat} data. The Tafel slope for the mesoporous IrO_x electrode is comparable with those (≈ 40 -50 mV dec⁻¹) of some most efficient electrocatalysts reported previously for

IrO_x nanoparticle films[10, 13] and distinctly lower than other reports (60-130 mV dec⁻¹) of nanostructured IrO_x. [23, 24]

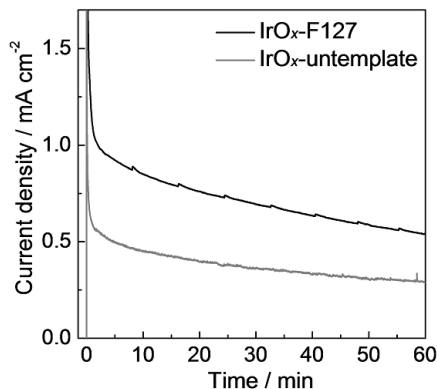


Figure 4. Current-time profiles during electrocatalysis at 1.2 V vs Ag/AgCl using of IrO_x electrodes calcined at 400 °C

The current-time profiles during potential-controlled bulk electrolysis are displayed in Fig. 4. After an initial spike in a current density (related to the capacitance component at the electrode-liquid interface) an anodic current due to electrocatalytic water oxidation was observed for respective IrO_x electrodes. The charge amount passed and the amount (n_{O_2}) of O₂ evolved during the 1h electrocatalysis for IrO_x-F127 are 2.61 C and 6.7 μmol (100% Faradaic efficiency), respectively. The n_{O_2} value is ~1.9 times higher than that (3.6 μmol, 100% Faradaic efficiency) of the IrO_x-untemplate. The higher performance of IrO_x-F127 for electrocatalytic water oxidation is ascribed to the large surface-to-mass ratio (75 m² g⁻¹) of the mesoporous structure to provide increased number of active Ir-sites at the interface between the film and the electrolyte solution, and to the matrix of interconnected nanoparticles to afford fast electron transport in the film, as well as to the increased intrinsic catalytic activity of the Ir-sites.[14, 25] The fast electron transport was suggested by the impedance spectra measured at 1.0 V. The charge transfer resistance (R_{ct}) for IrO_x-F127 (576 Ωcm²) is significantly lower than that of IrO_x-untemplate (700 Ωcm²), which is attributed to the efficient electron transfer in the boundaries between well-connected nanoparticles of mesoporous matrix.

4 Conclusions

We successfully developed a simple and facile one-pot strategy for fabrication of a new mesoporous IrO_x film formed by assembly of interconnected nanoparticles. The Ir-precursor complex solution derived by a polymer surfactant Pluronic F127 was drop-casted over FTO electrodes and then annealed at 400 °C to yield a transparent and stably adherent IrO_x film that work efficiently for electrocatalytic water oxidation. The

mesoporous IrO_x electrode is expected to be widely applicable to artificial photosynthesis technology because the highly active film is easily prepared without any complicated procedure.

Acknowledgements

This work was supported by the JST PRESTO program, JSPS KAKENHI Grant Number 24107003, 24350028. DC thanks JSPS for providing postdoctoral fellowship.

References

- [1] T. R. Cook, D. K. Dogutan, S. Y. Reece, Y. Surendranath, T. S. Teets, and D. G. Nocera, "Solar Energy Supply and Storage for the Legacy and Nonlegacy Worlds," *Chemical Reviews*, vol. 110, pp. 6474-6502, 2010.
- [2] H. S. Ahn and T. D. Tilley, "Electrocatalytic Water Oxidation at Neutral pH by a Nanostructured Co(PO₃)₂ Anode," *Advanced Functional Materials*, vol. 23, pp. 227-233, 2013.
- [3] M. W. Kanan and D. G. Nocera, "In Situ Formation of an Oxygen-Evolving Catalyst in Neutral Water Containing Phosphate and Co²⁺," *Science*, vol. 321, pp. 1072-1075, 2008.
- [4] D. Chandra, K. Saito, T. Yui, and M. Yagi, "Crystallization of Tungsten Trioxide Having Small Mesopores: Highly Efficient Photoanode for Visible-Light-Driven Water Oxidation," *Angewandte Chemie International Edition*, vol. 52, pp. 12606-12609, 2013.
- [5] X. Sala, I. Romero, M. Rodríguez, L. Escriche, and A. Llobet, "Molecular Catalysts that Oxidize Water to Dioxide," *Angewandte Chemie International Edition*, vol. 48, pp. 2842-2852, 2009.
- [6] M. M. Najafpour, T. Ehrenberg, M. Wiechen, and P. Kurz, "Calcium Manganese(III) Oxides (CaMn₂O₄·xH₂O) as Biomimetic Oxygen-Evolving Catalysts," *Angewandte Chemie International Edition*, vol. 49, pp. 2233-2237, 2010.
- [7] Y. Gorlin and T. F. Jaramillo, "A Bifunctional Nonprecious Metal Catalyst for Oxygen Reduction and Water Oxidation," *Journal of the American Chemical Society*, vol. 132, pp. 13612-13614, 2010.
- [8] K. Aiso, R. Takeuchi, T. Masaki, D. Chandra, K. Saito, T. Yui, and M. Yagi, "Carbonate Ions Induce Highly Efficient Electrocatalytic Water Oxidation by Cobalt Oxyhydroxide Nanoparticles," *ChemSusChem*, vol. 10, pp. 687-692, 2017.
- [9] T. Nakagawa, N. S. Bjorge, and R. W. Murray, "Electrogenerated IrO_x Nanoparticles as Dissolved Redox Catalysts for Water Oxidation," *Journal of the American Chemical Society*, vol. 131, pp. 15578-15579, 2009.
- [10] Y. Zhao, N. M. Vargas-Barbosa, E. A. Hernandez-Pagan, and T. E. Mallouk, "Anodic Deposition of Colloidal Iridium Oxide Thin Films from Hexahydroxyiridate(IV) Solutions," *Small*, vol. 7, pp. 2087-2093, 2011.
- [11] T. Kuwabara, E. Tomita, S. Sakita, D. Hasegawa, K. Sone, and M. Yagi, "Characterization and Analysis of Self-Assembly of a Highly Active Colloidal Catalyst for Water Oxidation onto Transparent Conducting Oxide Substrates," *The Journal of Physical Chemistry C*, vol. 112, pp. 3774-3779, 2008.
- [12] M. Yagi, E. Tomita, S. Sakita, T. Kuwabara, and K. Nagai, "Self-Assembly of Active IrO₂ Colloid Catalyst on an ITO Electrode for Efficient Electrochemical Water Oxidation," *The Journal of Physical Chemistry B*, vol. 109, pp. 21489-21491, 2005.

- [13] D. Chandra, D. Takama, T. Masaki, T. Sato, N. Abe, T. Togashi, M. Kurihara, K. Saito, T. Yui, and M. Yagi, "Highly Efficient Electrocatalysis and Mechanistic Investigation of Intermediate $\text{IrO}_x(\text{OH})_y$ Nanoparticle Films for Water Oxidation," *ACS Catalysis*, vol. 6, pp. 3946-3954, 2016.
- [14] D. Chandra, N. Abe, D. Takama, K. Saito, T. Yui, and M. Yagi, "Open Pore Architecture of an Ordered Mesoporous IrO_2 Thin Film for Highly Efficient Electrocatalytic Water Oxidation," *ChemSusChem*, vol. 8, pp. 795-799, 2015.
- [15] W. J. Youngblood, S.-H. A. Lee, Y. Kobayashi, E. A. Hernandez-Pagan, P. G. Hoertz, T. A. Moore, A. L. Moore, D. Gust, and T. E. Mallouk, "Photoassisted Overall Water Splitting in a Visible Light-Absorbing Dye-Sensitized Photoelectrochemical Cell," *Journal of the American Chemical Society*, vol. 131, pp. 926-927, 2009.
- [16] S. D. Tilley, M. Cornuz, K. Sivula, and M. Grätzel, "Light-Induced Water Splitting with Hematite: Improved Nanostructure and Iridium Oxide Catalysis," *Angewandte Chemie International Edition*, vol. 49, pp. 6405-6408, 2010.
- [17] T. Nakagawa, C. A. Beasley, and R. W. Murray, "Efficient Electro-Oxidation of Water near Its Reversible Potential by a Mesoporous IrO_x Nanoparticle Film," *The Journal of Physical Chemistry C*, vol. 113, pp. 12958-12961, 2009/07/30 2009.
- [18] E. N. El Sawy and V. I. Birss, "Nano-porous iridium and iridium oxide thin films formed by high efficiency electrodeposition," *Journal of Materials Chemistry*, vol. 19, pp. 8244-8252, 2009.
- [19] E. Ortel, T. Reier, P. Strasser, and R. Kraehnert, "Mesoporous IrO_2 Films Templated by PEO-PB-PEO Block-Copolymers: Self-Assembly, Crystallization Behavior, and Electrocatalytic Performance," *Chemistry of Materials*, vol. 23, pp. 3201-3209, 2011.
- [20] C. Sanchez, C. Boissière, D. Grosso, C. Laberty, and L. Nicole, "Design, Synthesis, and Properties of Inorganic and Hybrid Thin Films Having Periodically Organized Nanoporosity," *Chemistry of Materials*, vol. 20, pp. 682-737, 2008.
- [21] D. Chandra, T. Ohji, K. Kato, and T. Kimura, "Ligand-Assisted Fabrication of Small Mesopores in Semi-Crystalline Titanium Oxide Films for High Loading of Ru(II) Dyes," *Langmuir*, vol. 27, pp. 11436-11443, 2011.
- [22] D. Zhao, P. Yang, N. Melosh, J. Feng, B. F. Chmelka, and G. D. Stucky, "Continuous Mesoporous Silica Films with Highly Ordered Large Pore Structures," *Advanced Materials*, vol. 10, pp. 1380-1385, 1998.
- [23] J.-M. Hu, J.-Q. Zhang, and C.-N. Cao, "Oxygen evolution reaction on IrO_2 -based DSA[®] type electrodes: kinetics analysis of Tafel lines and EIS," *International Journal of Hydrogen Energy*, vol. 29, pp. 791-797, 2004.
- [24] M. Yagi, E. Tomita, and T. Kuwabara, "Remarkably high activity of electrodeposited IrO_2 film for electrocatalytic water oxidation," *Journal of Electroanalytical Chemistry*, vol. 579, pp. 83-88, 2005.
- [25] E. A. Meulenkaamp, "Electron Transport in Nanoparticulate ZnO Films," *The Journal of Physical Chemistry B*, vol. 103, pp. 7831-7838, 1999.

Spray Pyrolysis Synthesis of Mesoporous γ -Alumina Supported Metal and Metal Phosphide Catalysts and Their Catalytic Activity

JINSOO KIM, KYUNGMIN IM, JAE HYUNG CHOI, HOANG VU LY, SEUNG-SOO KIM, CHUL-WOO NAM, SUNG-DON KIM & HYUNG-KYU PARK

Abstract In this study, spherical γ -Al₂O₃ supported metal and metal phosphide catalysts were successfully prepared by spray pyrolysis of boehmite sol or slurry. First boehmite sol was prepared based on the Yoldas process and boehmite slurry was prepared by peptizing the commercial boehmite particles. Then the corresponding metal salts were added to the sol/slurry at the desired concentration, followed by spray pyrolysis of the mixed solution. As the well-mixed solution was transformed to spherical γ -Al₂O₃ supported metal and metal phosphide catalysts during spray pyrolysis process, the metal species were uniformly distributed in the mesoporous γ -Al₂O₃ supports. The product catalysts were investigated under different conditions for hydrodeoxygenation (HDO) of bio-oil model compound, 2-furyl methyl ketone (FMK), which is the main component of the bio-oil product from pyrolysis of *Saccharina japonica*.

Keywords: • guide • format • figures • tables • references •

CORRESPONDENCE ADDRESS: Jinsoo Kim, Ph.D., Professor, Kyung Hee University, Department of Chemical Engineering, Yongin-si, Gyeonggi-do 17104, Korea, e-mail: jkim21@khu.ac.kr. Kyungmin Im, M.S. student, Kyung Hee University, Department of Chemical Engineering, Yongin-si, Gyeonggi-do 17104, Korea, e-mail: catt917@naver.com. Jae Hyung Choi, M.S. student, Kyung Hee University, Department of Chemical Engineering, Yongin-si, Gyeonggi-do 17104, Korea, e-mail: jaehc@khu.ac.kr. Hong Vu Ly, Ph.D., Research Associate, Kangwon National University, Department of Chemical Engineering, Samcheok, Gangwon-do, Korea, e-mail: lyhoangvu87@gamil.com. Seung-Soo Kim, Ph.D., Professor, Kangwon National University, Department of Chemical Engineering, Samcheok, Gangwon-do, Korea, e-mail: sskim2008@kangwon.ac.kr. Chul-Woo Nam, Ph.D., Principal Researcher, Mineral Resources Research Division, Korea Institute of Geoscience and Mineral Resources, Daejeon, Korea, e-mail: baram@kigam.re.kr. Sung-Don Kim, Ph.D., Principal Researcher, Mineral Resources Research Division, Korea Institute of Geoscience and Mineral Resources, Daejeon, Korea, e-mail: sdkim@kigam.re.kr. Hyung-Kyu Park, Ph.D., Principal Researcher, Mineral Resources Research Division, Korea Institute of Geoscience and Mineral Resources, Daejeon, Korea, e-mail: parkhk@kigam.re.kr.

1 Introduction

Many researchers have investigated the deoxygenation under hydrotreating using different catalysts (catalytic hydrodeoxygenation (HDO)) on various supports such as zeolite, silica, alumina, and activated carbon. Among various catalysts, metal phosphide catalysts, especially transition metal phosphide catalysts, have attracted tremendous attention because they showed excellent properties in HDO with the presence of phosphorus [1-3]. These reports suggest that catalytic HDO has been accepted as a potential method for removal of oxygen in bio-oil.

Before these catalysts are used for upgrading bio-oil, their catalytic activity should be studied first via HDO of model compounds that were main compositions in the bio-oil derived from pyrolysis of various biomass resources. It was reported that 2-furyl methyl ketone (FMK) was one of the major compositions in bio-oil derived from thermochemical processes [4,5]. In this study, we investigated the HDO of FMK over metal (Ni, Co) and metal phosphide (Ni₂P, CoP) catalysts to investigate the feasibility of these catalysts for bio-oil upgrading and catalytic pyrolysis of *S. japonica* alga in large-scale system. In particular, γ -Al₂O₃ supported metal and metal phosphide catalysts were prepared by spray pyrolysis of boehmite sol/slurry mixed with metal salts. As the mixed solution, consisting of boehmite sol/slurry and metal salts, was transformed to spherical γ -Al₂O₃ supported metal and metal phosphide catalysts during spray pyrolysis process, the metal species were uniformly distributed in the mesoporous γ -Al₂O₃ supports.

2 Experimental

2.1 Catalyst preparation

Spherical γ -Al₂O₃ supported metal and metal phosphide (Ni, Co, Ni₂P and CoP) catalysts were synthesized by spray pyrolysis of boehmite sol or slurry mixed with metal salts. First, boehmite sol was prepared by hydrolysis and condensation of aluminum isopropoxide (AIP; Al(OC₃H₇)₃, 98%, Aldrich), using the modified Yoldas process [6]. The AIP was hydrolyzed in an excess amount of distilled water at 80-85 °C. After stirring for 1 h, the resulting slurry (with AlOOH precipitates) was peptized with 1 M HNO₃ at the molar ratio of [H⁺]/[Al³⁺] = 0.07. The sol was refluxed at 95-100 °C for 12 h. For boehmite slurry, commercial boehmite particles were peptized with 1 M HNO₃ at the various molar ratio of [H⁺]/[Al³⁺] = 0.06, 0.12, and 0.24.

To synthesize Ni, Co, Ni₂P or CoP catalysts, the calculated amount of cobalt nitrate hexahydrate (98%, Aldrich), nickel nitrate hexahydrate (98% Aldrich), and ammonium phosphate dibasic (98%, Aldrich) were added to 150 ml of boehmite sol or slurry, and stirred for 30 minutes, followed by ultrasonic spray pyrolysis as reported in our previous work [7]. In brief, the precursor solution was nebulized by a 1.7 MHz ultrasonic spray generator with six vibrators. The generated droplets were carried into a quartz reactor

heated at 800 °C by a constant flow of N₂ gas. The produced particles were collected in a Teflon bag installed at the bottom of the spray pyrolysis unit.

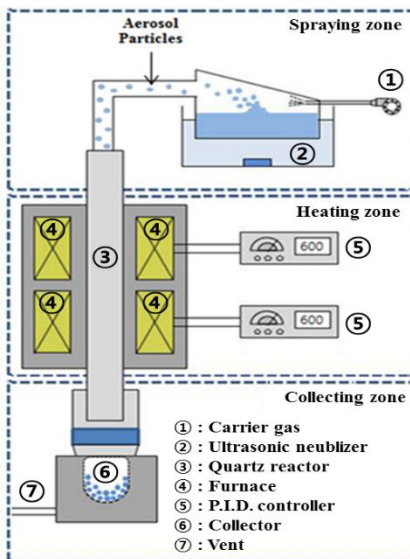


Figure 1. Schematic diagram of spray pyrolysis

2.2 Catalyst characterization

The catalysts were characterized by TPR, XRD and BET methods. For TPR analysis, the catalyst samples were reduced in H₂ environment at atmospheric pressure. During TPR process, the temperature of reactor was continuously heated up to 850 °C with a heating rate of 2 °C/min. The H₂ consumption was measured by GC. The surface area, pore volume and average pore size distribution of the catalyst sample were determined using N₂ porosimetry (ASAP 2020, Micromeritics) employing BET method. The crystallographic structure of catalysts was determined by XRD (MAC-18XHF, Rigaku). The morphology of catalyst was analyzed using FE-SEM (Leo-Supra 55, Genesis 2000, Carl Zeiss).

As shown in Fig. 2, a fixed-bed reactor made of Quartz glass with an internal diameter of 5 mm and a length of 550 mm was used for HDO experiment at atmospheric pressure [8,9]. A pre-heater was used to heat the gas flow up to 120 °C and evaporate FMK solution before entering the reactor. For each experiment, 0.2 g of catalyst was loaded into the fixed-bed reactor. The oxide catalysts were reduced to metal or metal phosphide catalysts at 720 °C for 2 h in H₂/Ar gas mixture with a flow ratio of 1:4, followed by cooling in Ar environment prior to catalytic deoxygenation [10]. The reaction temperatures of 300 °C, 350 °C and 400 °C were selected in the experiment. An amount

of 1.1 g FMK (99.0%, Aldrich) was dissolved in 50 ml n-heptane and this solution was continuously injected using a liquid pump with flow rate of 0.2 mL/min, together with H₂/Ar mixture. Finally, the liquid products were collected and then analyzed by GC-MS (Agilent 7890A) equipped with capillary column of HP-5MS. The compositions of gas products were determined by using GC. The activity of the catalyst was based on the FMK conversion (C_{FMK}) and products selectivity (S_p), defined as follows:

$$C_{FMK} = \left(1 - \frac{n_{FMK}}{n_{FMK}^o} \right) \times 100\% \quad (1)$$

$$S_p = \left(\frac{n_p}{n_{FMK}^o - n_{FMK}} \right) \times 100\% \quad (2)$$

where n_{FMK}^o and n_{FMK} denote the molar FMK of the initial input and the remaining output, respectively, while n_p is the molar product p.

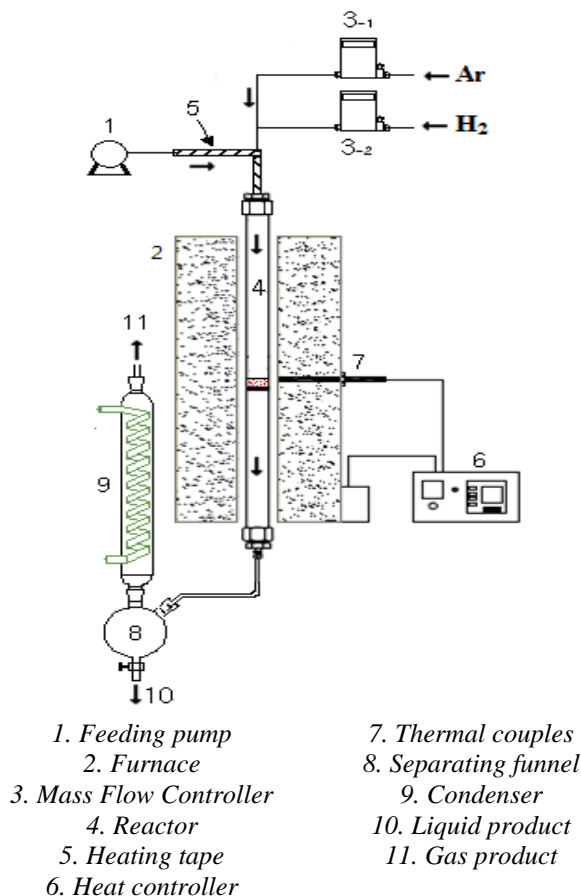


Figure 2. Schematic diagram of fixed-bed reactor for hydrodeoxygenation experiment

3 Results

One of advantages of the ultrasonic spray pyrolysis is to produce spherical particles. The produced catalysts showed similar sized spherical particles in the size range of 0.5~2.0 μm regardless of the added catalyst species. Also, EDX dot mapping showed that catalyst species were well-distributed throughout the $\gamma\text{-Al}_2\text{O}_3$ supports.

The textural properties of spray pyrolysis-derived (Ni, Co, Ni_2P , CoP)/ $\gamma\text{-Al}_2\text{O}_3$ catalysts were determined by N_2 adsorption-desorption isotherms at 77 K. The $\gamma\text{-Al}_2\text{O}_3$ support without any catalysts has the specific surface area (S_{BET}) of 162.78 m^2/g , the pore volume of 0.15 cm^3/g , and the average pore size of 3.36 nm. When 10 wt% of metal (Co, Ni) or

metal phosphide (Ni_2P , CoP) was added, the (Ni , Co , Ni_2P , CoP)/ γ - Al_2O_3 catalysts showed the specific surface area in the range of 132.73~198.42 m^2/g , the pore volume in the range of 0.16~0.23 cm^3/g and the average pore size in the range of 3.29~4.01 nm, respectively, depending on catalyst species and calcination temperature (Table 1).

Table 1. Pore structure data of various catalysts

Catalyst	Surface area (m^2/g)	Pore volume (cm^3/g)	Average pore size (nm)
10wt% Ni/ γ -alumina	155.31	0.2	3.92
10wt% Co/ γ -alumina	132.73	0.16	3.8
10wt% Ni_2P / γ -alumina	172.88	0.19	3.61
10wt% CoP / γ -alumina	138.41	0.16	3.87
γ -alumina	162.78	0.15	3.36

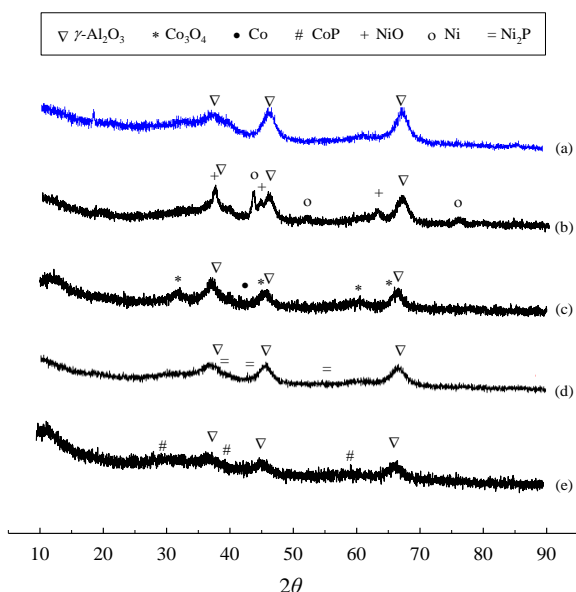


Figure 3. XRD patterns of γ - Al_2O_3 -supported catalysts: (a) γ - Al_2O_3 , (b) 10wt% Ni/ γ - Al_2O_3 , (c) 10wt% Co/ γ - Al_2O_3 , (d) 10wt% Ni_2P / γ - Al_2O_3 , and (e) 10wt% CoP / γ - Al_2O_3 .

The XRD patterns of 10 wt% (Ni, Co, Ni₂P, CoP)/ γ -Al₂O₃ catalysts after calcination at 800 °C were illustrated in Fig. 3. The diffraction peaks of the 10 wt% Ni-SP800 catalyst at $2\theta = 37.1^\circ, 43.5^\circ, 62.8^\circ$ are the characteristics of NiO phase [11]. The Ni peaks appeared at 2θ values of $44.5^\circ, 52.07^\circ$ and 75.4° [12]. In XRD patterns of Co-containing catalysts, the peaks of CoP phase appeared at $2\theta = 31.6^\circ, 48.1^\circ, \text{ and } 56.7^\circ$ [10], whereas the peak signal of Co was observed at $2\theta = 42.39^\circ$ and the peaks of spinel Co₃O₄ were pointed out at $31.9^\circ, 37.2^\circ, 45.23^\circ, \text{ and } 59.6^\circ$ [5]. The 10 wt% Ni₂P-SP800 displayed peaks at $38.6^\circ, 44.7^\circ, \text{ and } 54.2^\circ$, which correspond to Ni₂P. These results were similar to those reported by Bui *et al.* [3].

The typical temperature-programmed reduction (TPR) profiles reflect the reduction process of metal oxides or metal/metal-oxide phosphate to metal or metal phosphide via the interaction between these species and the support [11]. Based on TPR profile, the optimum reduction temperature for catalysts can be determined before using them in HDO. The TPR profiles of different catalysts used in this study presented peaks in the range of 400~750 °C. The curves that appeared at temperature lower than 650 °C were attributed to the reduction of metal oxide to metal. The metal phase in this region was highly dispersed and strongly bonded with the support [13]. Meanwhile, the reduction of metal oxide phosphate or metal phosphate to metal phosphide was performed in range of 650~750 °C [3,13]. It was observed that the reduction temperature at maximum shifted to low value with the presence of phosphorus content in precursor composition. This trend might be attributed to the decrease of interaction between metal and catalyst support that related to formation of large clusters of metal oxide in catalyst [13].

The influence of phosphorus addition on FMK conversion was also studied. As shown in Table 2, the addition of P to Co catalyst increased the FMK conversion slightly, while the addition of P to Ni catalyst decreased the FMK conversion substantially. The activity of Co catalyst was stable when P was incorporated or combined with Co. Furthermore, the presence of phosphorus also improved the activity of catalyst due to increasing metal-phosphide interaction on support [14]. However, adding P into Ni catalyst showed the opposite results. Leiva *et al.* [2] and Oyama [15] also reported that increasing phosphorus content could reduce active sites, resulting in a decrease in catalyst activity. This might be due to higher interaction of P with γ -Al₂O₃ support than metal-support interaction. Moreover, this interaction was known to hinder reduction that resulted in decreasing the active site occupancy for the incoming FMK deoxygenation, thus lowering FMK conversion.

Table 2. Liquid phase product selectivity in HDO of FMK over various catalyst at 400°C

Catalyst	Conversion C_{FMK}	Products selectivity (S_p)	
		2-Allyl furan	Methyl cyclohexane
10wt% Ni / \square -alumina	83.02	90.20	9.80
10wt% Co / \square -alumina	72.87	80.16	19.84
10wt% Ni ₂ P / \square -alumina	69.93	92.25	7.75
10wt% CoP / \square -alumina	75.57	86.33	13.67

The HDO of FMK was performed with 10 wt% (Ni, Co, Ni₂P, CoP)/ γ -Al₂O₃ catalysts at reaction temperature of 400 °C under atmospheric pressure. Table 2 shows the effects of catalyst species on FMK conversion and product distributions. The initial conversions of FMK over 10 wt% (Ni, Co, Ni₂P, CoP)/ γ -Al₂O₃ catalysts were 83.02 %, 72.87%, 69.93%, and 75.57%, respectively. However, the catalysts prepared by spray pyrolysis method showed better catalytic activity than those prepared by incipient wetness impregnation method. The highest FMK conversion of 83.02 % was obtained using 10 wt% Ni/ γ -Al₂O₃ catalysts. This might be due to the high catalytic active sites in terms of the metal dispersion, leading to high activity of catalyst.

From Table 2, it can be observed that the liquid phase products were composed of two components: 2-allyl furan and methyl cyclohexane. The selectivities of 2-allyl furan and methyl cyclohexane were in the range of 80.16~92.25 and 7.75~19.84, respectively. The product yields of 2-allyl furan and methyl cyclohexane were affected by catalyst species. Among the investigated catalysts, 10 wt% Ni/ γ -Al₂O₃ catalysts showed the highest FMK conversion of 83.02% and the highest 2-allyl furan yield of 74.89%.

The gas phase product distribution obtained from HDO of FMK over various catalysts were analysed by GC. CO, CO₂ and CH₄ were main compositions in the gaseous products during HDO. The gas products obtained using the various catalysts showed more or less similar gas compositions, consisting of CO₂ (96.23-99.17 %), CO (0.81-3.04 %), and CH₄ (0.01-0.73 %).

4 Conclusions

Mesoporous γ -Al₂O₃ supported metal and metal phosphide catalysts were successfully prepared by spray pyrolysis of boehmite sol/slurry mixed with metal salts. The pore structure of the product catalysts could be controlled depending on precursor solution and

spray pyrolysis conditions. The product 10 wt% (Ni, Co, Ni₂P, CoP)/ γ -Al₂O₃ catalysts were utilized for HDO of FMK at 400 °C. The liquid phase of FMK was successfully converted into 2-allyl furan and methyl cyclohexane, whereas the gas phase was mainly CO₂. The catalysts prepared by spray pyrolysis method showed better catalytic activity in HDO than those prepared by the conventional incipient wetness impregnation method. This suggests the spray pyrolysis might be a potential approach for catalyst synthesis.

Acknowledgements

This research was supported by the Basic Research Project ‘Technical Development for Producing AlN from the Bauxite Smelting Product through Reduction-Nitrizing Process’ of the Korea Institute of Geoscience and Mineral Resources (KIGAM) funded by the Ministry of Science, ICT and Future Planning of Korea.

References

- [1] H.V. Ly, S.S. Kim, J. Kim, J.H. Choi, and H.C. Woo, “Effect of acid washing on pyrolysis of *Cladophora socialis* alga in microtubing reactor,” *Energ Convers Manage*, vol.106, pp.260-267, 2015.
- [2] K. Leiva, C. Sepúlveda, R. García, J.L.G. Fierro, G. Águila, P. Baeza, M. Villarroel, and N. Escalona, “Effect of P content in the conversion of guaiacol over Mo/ γ -Al₂O₃ catalysts,” *Appl Catal, A*, vol.467, pp.568-574, 2013.
- [3] P. Bui, J.A. Cecilia, S.T. Oyama, A. Takagaki, A. Infantes-Molina, H. Zhao, D. Li, E. Rodríguez-Castellón, and A. Jiménez López, “Studies of the synthesis of transition metal phosphides and their activity in the hydrodeoxygenation of a biofuel model compound,” *J Catal*, vol.294, pp.184-198, 2012.
- [4] S.S. Kim, H.V. Ly, G. Choi, J. Kim, and H.C. Woo, “Pyrolysis characteristics and kinetics of the alga *Saccharina japonica*,” *Bioresour Technol*, vol.123, pp.445-451, 2012.
- [5] T.A. Le, H.V. Ly, and J. Kim, “Catalytic Pyrolysis of Alga *Saccharina japonica* Using Co/ γ -Al₂O₃ and Ni/ γ -Al₂O₃ Catalyst,” *Energ Source Part A*, vol.36(21), pp.2392-2400, 2014.
- [6] H.T. Kwon, J. Kim, and M.R. Othman, “Characteristics of alumina membranes prepared from different metal-organic compounds,” *Synth React Inorg Mat*, vol.42(7), pp.928-934, 2012.
- [7] P. Palmero, “Structural Ceramic Nanocomposites: A Review of Properties and Powders’ Synthesis Methods,” *Nanomaterials*, vol.5, pp.656-696, 2015.
- [8] S. Sithisa, and D. Resasco, “Hydrodeoxygenation of furfural over supported metal catalysts: a comparative study of Cu, Pd and Ni,” *Catal Lett*, vol.141, pp.784-791, 2011.
- [9] X. Zhu, L.L. Lobban, R.G. Mallinson, and D.E. Resasco, “Bifunctional transalkylation and hydrodeoxygenation of anisole over a Pt/HBeta catalyst,” *J Catal*, vol.281, pp.21-29, 2011.
- [10] T.A. Le, H.V. Ly, J. Kim, S.S. Kim, J.H. Choi, H.C. Woo, “Hydrodeoxygenation of 2-furyl methyl ketone as a model compound in bio-oil from pyrolysis of *Saccharina japonica* alga in fixe-bed reactor,” *Chem Eng J*, vol.105, pp.157-163, 2014.
- [11] A. Bshish, Z. Yaakob, A. Ebshish, and F.H. Alhasan, “Hydrogen production via ethanol steam reforming over Ni/Al₂O₃ catalysts: effect of Ni loading,” *J. Energy Resour Technol*, vol.136(1), pp.012601-13, 2013.

- [12] L. Xua, H. Song, and L. Choua, "Carbon dioxide reforming of methane over ordered mesoporous NiO–MgO–Al₂O₃ composite oxides," *Appl Catal, B*, vol.108-109, pp.177-190, 2011.
- [13] B. Valle, B. Aramburu, A. Remino, J. Bilbao, and A.G. Gayubo, "Effect of calcination/reduction conditions of Ni/La₂O₃- α Al₂O₃ catalyst on its activity and stability for hydrogen production by steam reforming of raw bio-oil/ethanol," *Appl Catal, B*, vol.147, pp.402-410, 2014.
- [14] M.W.J. Crajé, V.H.J. De Beer, and A.M. van der Kraan, "Mössbauer emission study on 57 Co doped carbon-supported Ni and Ni-Mo sulfide hydrotreating catalysts. The influence of phosphorus on the structure," *Catal Today*, vol.10(3), pp.337-344, 1991.
- [15] S.T. Oyama, "Novel catalysts for advanced hydroprocessing: transition metal phosphides," *J Catal*, vol.216, pp.343-352, 2003.

Gear Body Structure Design to Lower Vibration Emission

RIAD RAMADANI, ALEŠ BELŠAK, MARKO KEGL, JOŽEF PREDAN & STANISLAV PEHAN

Abstract A new approach to gear body modification is presented. The subject of the study is a spur gear with reference points that are intended for observing the vibration emission and that are located on the ring and on the hub. The primary objective is to reduce noise emission and vibration in general. The second objective is to rise the torsional elasticity of the gear body. The problem of the design is dealt with numerically. The solid gear body is replaced with some kind of a cellular structure. The cellular structure is designed and optimized with a noncommercial software that is based on the strain energy control. To increase the vibration damping of the structure the polymer matrix is provided. The basic properties of the gear structure are verified numerically. The whole gear is made by 3D printing of titanium. Finally, the tooth flanks are grinded. The modified gear is tested on the test rig. The damping properties of the modified gear with and without a polymer insert are measured in order to confirm the predictions.

Keywords: • gear vibration • gear body structure • lattice structure • finite element analysis • topology optimization •

CORRESPONDENCE ADDRESS: Riad Ramadani, Assistant, University of Prishtina, Faculty of Mechanical Engineering, Bregu i diellit, p.n. 10000 Prishtina, Kosovo, e-mail: riad.ramadani@uni-pr.edu. Ph.D. student, University of Maribor, Faculty of Mechanical Engineering, Smetanova ulica 17, 2000 Maribor, Slovenia, Aleš Belšak, Ph.D., Assistant Professor, University of Maribor, Faculty of Mechanical Engineering, Smetanova ulica 17, 2000 Maribor, Slovenia, e-mail: ales.belsak@um.si. Marko Kegl, Ph.D., Associate Professor, University of Maribor, Faculty of Mechanical Engineering, Smetanova ulica 17, 2000 Maribor, Slovenia, e-mail: marko.kegl@um.si. Jožef Predan, Ph.D., Associate Professor, University of Maribor, Faculty of Mechanical Engineering, Smetanova ulica 17, 2000 Maribor, Slovenia, e-mail: jozef.predan@um.si. Stanislav Pehan, Ph.D., Associate Professor, University of Maribor, Faculty of Mechanical Engineering, Smetanova ulica 17, 2000 Maribor, Slovenia, e-mail: stanislav.pehan@um.si.

1 Introduction

Gears are mechanical parts and are widely used in industry, such as automobile, aerospace and wind industry. With the increasing demands concerning lightweight, high speed and quiet running of gear transmissions, the reduction of noise and vibrations is becoming more and more important. Gear vibrations are caused mainly by tooth meshing [1]; during the mesh of the gear teeth, the meshing stiffness changes and causes gear vibration. A lot of research has been reported on gear noise and vibration reduction, mainly by tooth profile modification [2–5] and profile optimization [6, 7], but even if the tooth profile is modified, the change in the meshing stiffness during the gear mesh is still present and causes vibration. It is attempted to reduce gear vibration by introducing powder material in some holes drilled in the gear body [8, 9]. The powder material has an effect on the damping properties of gear vibrations.

In this paper, the reduction of the vibration through gear body modification is reported. The body structure is designed with some kind of a cellular structure. The cellular structure used to the gear body is a lattice structure. Topology optimization is used to optimize the lattice structure. Topology optimization is a method that optimizes material layout within a given space under boundary condition [10]. There are different topology optimization methods, such as Evolutionary Structural Optimization (ESO) method [11], Solid Isotropic Material with Penalization (SIMP) method [12], Bidirectional Evolutionary Structural Optimization (BESO) method [13, 14] and the new BESO method [15, 16]. All these methods are based on finite element analysis where each element is assigned as design variable. The objective function in topology optimization can be minimization of mean compliance in static problems, maximization of natural frequency in dynamic problems.

A gear with an optimized lattice structure is produced using Selective Laser Melting (SLM). SLM allows a part to be built additively, layer by layer, from the powder metal to a solid structure [17]. A completely new test rig is designed and developed for gear vibration and sound pressure measurement. The sound pressure of the gear with a lattice structure is measured and compared with that of the gear with a full solid body used as the reference gear.

2 Topology Optimization Problem

Topology optimization problem for stiffness maximization or mean compliance minimization with the volume constrain can be stated as [10, 18]:

$$\text{Minimize } C = \frac{1}{2} \mathbf{f}^T \mathbf{u} \quad (1)$$

$$\text{Subjected to: } V^* - \sum_{i=1}^N V_i x_i = 0 \quad (2)$$

$$x_i = 0 \text{ or } 1$$

where C is the mean compliance whereas \mathbf{f} and \mathbf{u} are the load and displacement vectors. V_i is the volume of an individual element and V^* is the total structural volume. N indicates the total number of elements, the binary design variable x_i declares the void (0) and the solid (1) element.

3 Design and Optimization of the gear body structure

3.1 Design of the gear body structure

A spur gear with involute profile with the data shown in Table 1 is designed. The numerical model of the gear is prepared in Abaqus/CAE 6.14.

Table 1. Basic data of a spur gear

Magnitude	Value
Number of teeth	34
Normal module (mm)	2.5
Pressure angle (°)	20
Facewidth, (mm)	10
Reference diameter (mm)	85
Base diameter (mm)	79.874
Root diameter (mm)	78.558
Tip diameter (mm)	85
Young`s modulus (MPa)	206000
Poisson`s ratio	0.3

The gear model is partitioned to clearly define the gear body that should be optimized; the gear hub diameter is 35 mm and the gear ring diameter is 68.750 mm. The whole gear is meshed with linear Hexahedral elements of type C3D8, which are the Eight-node linear brick element. Hexahedral elements are used in three-dimensional analysis because they give the best results at minimum costs [19]. The gear body is meshed with the structured mesh technique. The hub and the ring together with the teeth of the gear are meshed with

the sweep mesh technique. The Advancing front algorithm is used to create the mesh. The total number of the elements to mesh the gear is 2918412 hexahedral elements. The number of elements is large because topology optimization requires very fine mesh. In a step module, 68 general, static analysis steps and load cases are created for the model, in which a pressure load of 618 MPa is applied on both sides of the gear teeth. Each load case is valid in one step. A boundary condition constraining the inner surface of the gear hub is applied in the initial step. Finally, when the analysis is configured, a job associated with the model is created and an input file is written. Afterwards the input file is used in ProTOp to design and optimize the gear body structure. A spur gear is shown in Figure 1.

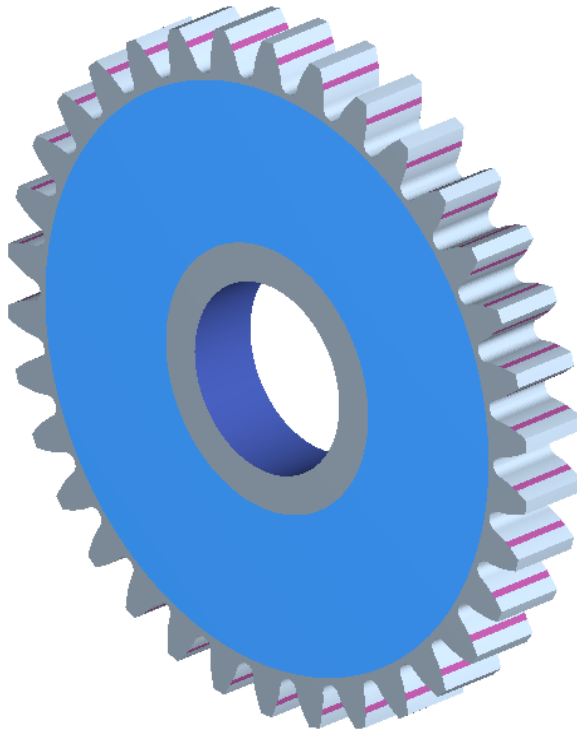


Figure 1. Free and fixed part of the gear

In order to achieve various optimization goals, the whole design domain has to be partitioned into sub domains. The hub and the ring together with the gear teeth will be the fixed domain, which means that they will stay unchanged during the optimization process, whereas the gear body will be the design domain, which is free for optimization. A cube diagonal lattice structure and a diagonal lattice in the cylindrical coordinate system is used to configure the model. The cylindrical coordinate system is defined by radius and angle, the radius of the first cube diagonal lattice cell is chosen to be 6 and the

angle is 10.59° . The width of the cube diagonal lattice cell is 7. The thickness of the diameter is from 0.8 to 2 mm. The configuration tool for the cube diagonal lattice structure is shown in Figure 2.

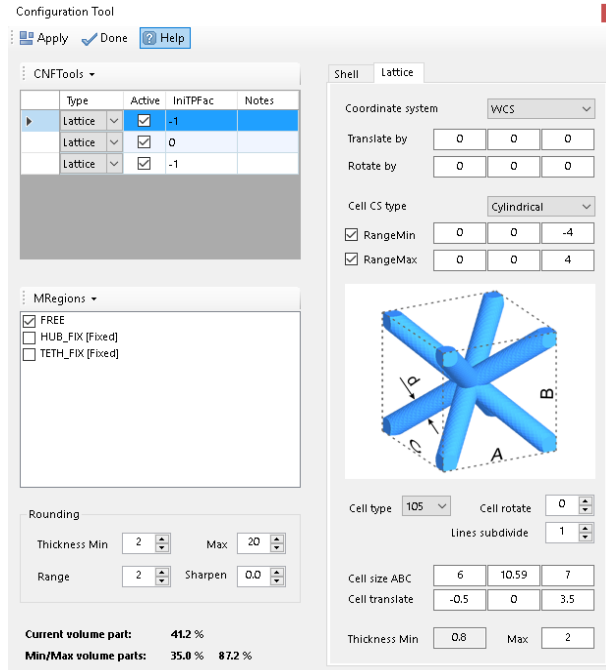


Figure 2. Configuration tool for the cube diagonal lattice structure

The radius of the second diagonal lattice cell is chosen to be 6 and the angle is 10.59° . The width of the cube diagonal lattice cell is 3.75. The thickness of the diameter can vary from 0.7 to 2 mm. The configuration tool for the diagonal lattice structure is shown in Figure 3.

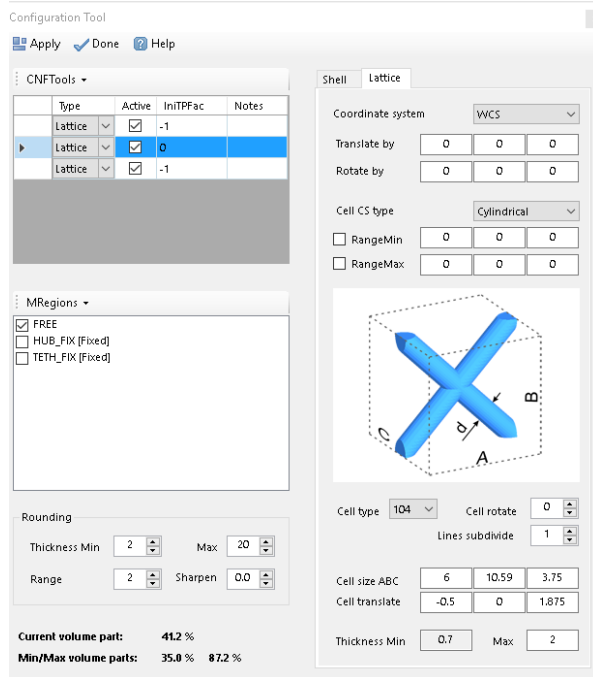


Figure 3. Configuration tool for the diagonal lattice structure

Another lattice structure is added in order to increase the width of the gear ring. The inner radius of the lattice is 34.375 mm and the gear ring is 5 mm.

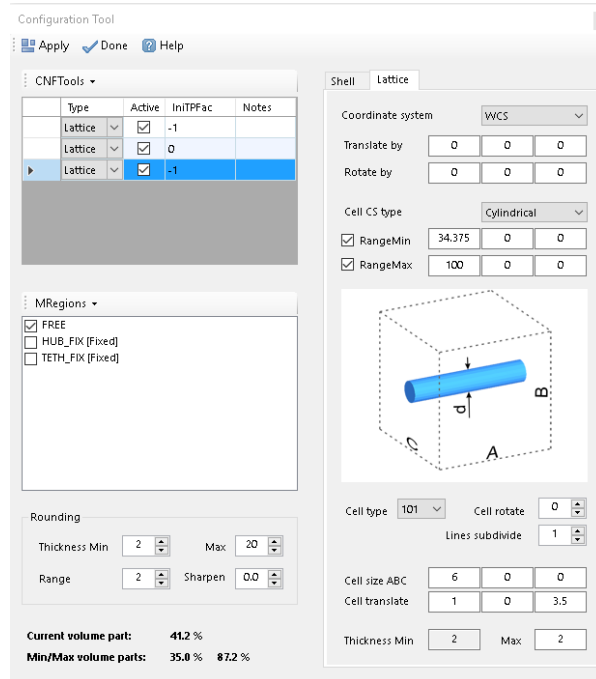


Figure 4. Configuration tool for the lattice structure

Finally, after adding the lattice structure, the current volume part is 41.2% and the final configuration of the gear body structure looks as shown in Figure 5.

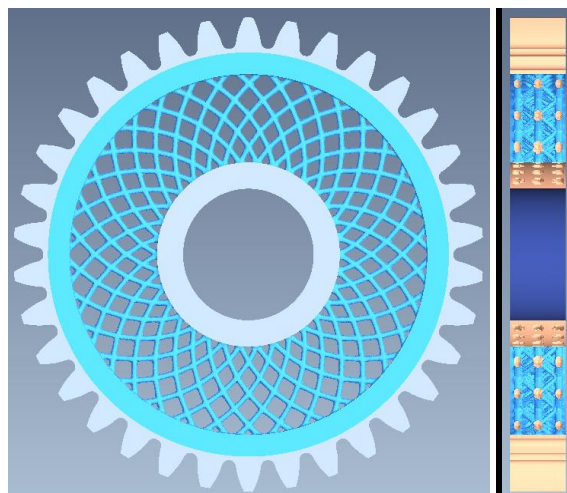


Figure 5. Design of the cube diagonal lattice and the diagonal lattice structure

3.2 Optimization of the gear body structure

The optimization procedure is an iterative process done by ProTop. Each iteration requires one finite element analysis and one computation of topology parameters. ProTop performs structural topology optimization by implementing an efficient evolutionary method based on heuristic principles and structural strain energy density [20].

After running the ProTop initialization step, the stress state is obtained. It is shown in Figure 6 that the initial stress of the gear with the lattice structure is 592.53 MPa.

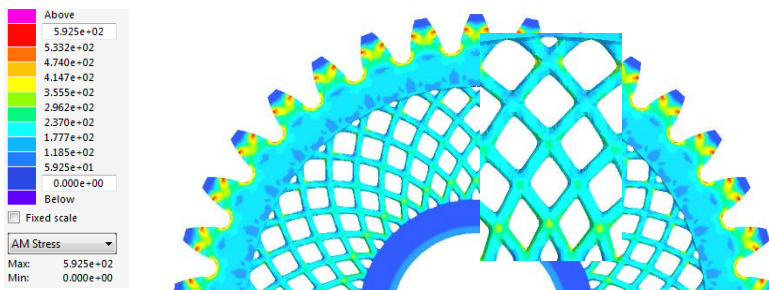


Figure 6. Initial stress of the lattice structure in the scale 552.9 MPa

In order to reduce the stress level of the lattice structure, topology optimization is performed. Based on the result of topology optimization, it is shown that stresses are reduced to around 552.9 MPa for the volume part 49.3%. Optimization results are presented in Figure 7. Based on the optimization results it is evident that the maximum stress is on the gear tooth. The stress level is approximately the same as in the gear with a full solid body. The lattice structure is changed by optimization process.

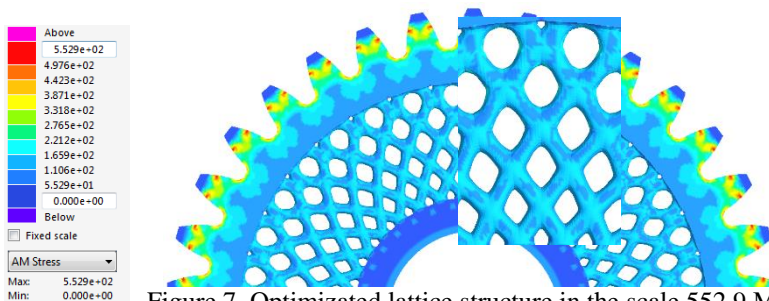


Figure 7. Optimized lattice structure in the scale 552.9 MPa

The comparison of the lattice structure before and after optimization is shown in Figure 8.

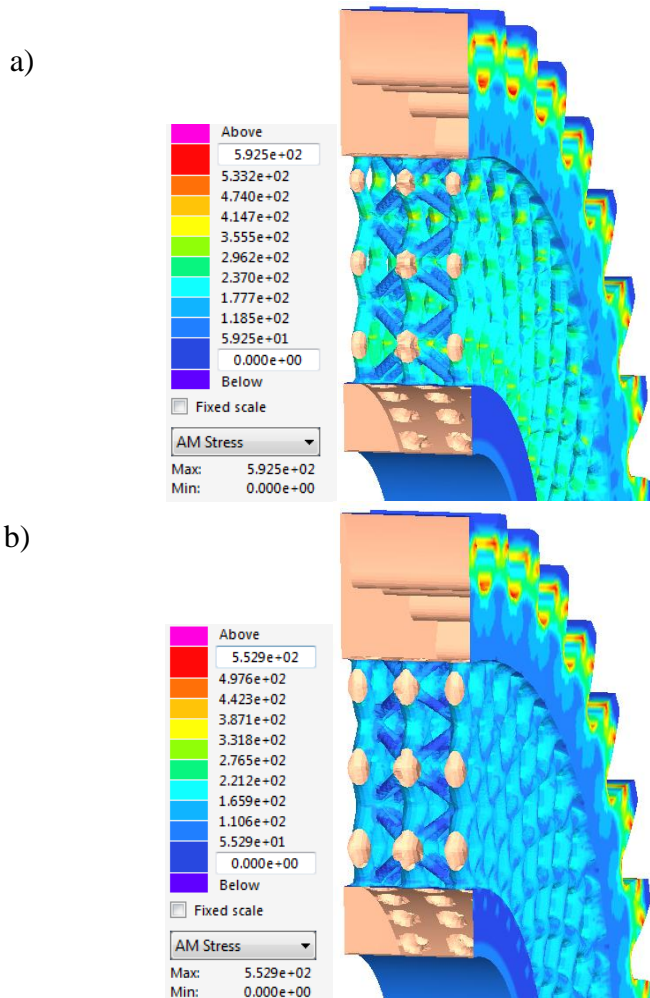


Figure 8. Comparison of lattice stresses,
 a) initial lattice stress, b) optimized lattice stress, in the scale 552.9 MPa

The volume of the gear with a full solid body is $V = 51130 \text{ mm}^3$, and the volume of the gear with the optimized lattice structure is $V_{opt} = 32570 \text{ mm}^3$. On the basis of volume comparison, it is shown that the gear with the lattice structure is lighter by 36.299 % than the gear with a full solid body.

The titanium gear with the optimized lattice structure is produced using Selective Laser Melting (SLM), and it is shown in Figure 9.



Figure 9. Photo of printed gear

4 Sound Pressure

To confirm the predictions concerning the gear vibration reduction, the sound pressure of the gear with a full solid body and the gear with the lattice structure is measured and compared. The center distance of the gear pair is $a = 90 \text{ mm}$, the number of rotation is $n = 310 \text{ min}^{-1}$ and the torque $T = 60 \text{ N} \cdot \text{m}$. The time signal of the sound pressure for the gear with a full solid body is presented in Figure 10.

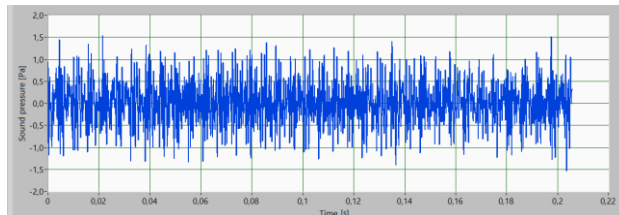


Figure 10. Time signal of sound pressure

The time signal is converted to the frequency spectrum, which is presented in Figure 11.

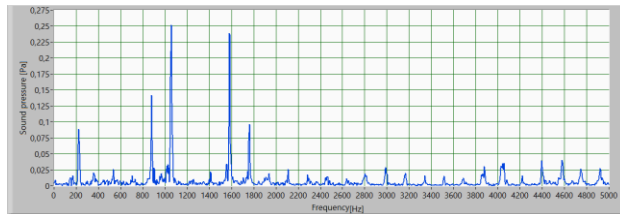


Figure 11. Frequency spectrum of sound pressure for the gear with a full solid body

The time signal of the sound pressure for the gear with the lattice structure is presented in Figure 12.

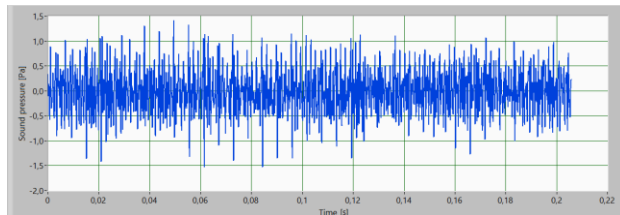


Figure 12. Time signal of sound pressure

The frequency spectrum for the gear with the lattice structure is presented in Figure 13.

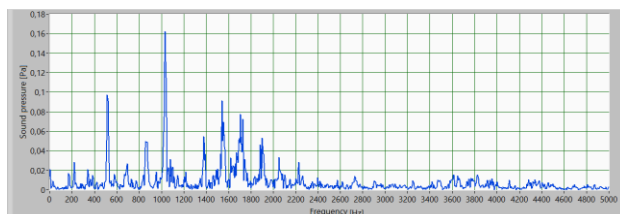


Figure 13. Frequency spectrum of sound pressure for the gear with the lattice structure

When comparing the frequency spectrum of sound pressure of the gear with a full solid body presented in Figure 11 and that of the gear with the lattice structure presented in Figure 13, it is shown that the lower amplitude with the distribution of components is evident in the frequency spectrum of the gear with the lattice structure.

5 Conclusion

A way of gear vibration reduction has been established, based on the gear body structure modification. The influence of the gear body structure on damping performance in gear vibration has been established. Experimental results have verified that a gear with the lattice structure effectively reduces the vibration. The initial stresses of the lattice structure of 592.5 MPa were reduced to 552.9 MPa, using topology optimization. Based

on the volume comparison, it is shown that the titanium printed gear with the lattice structure is lighter by 36.299 % than the gear with a full solid body.

References

- [1] J. D. Smith, *Gear Noise and Vibration*. New York, United States: CRC Press, 2003.
- [2] A. Kahraman and G. W. Blankenship, "Effect of Involute Tip Relief on Dynamic Response of Spur Gear Pairs," *Journal of Mechanical Design*, vol. 121, pp. 313–315, 1999.
- [3] G. Liu and R. G. Parker, "Dynamic Modeling and Analysis of Tooth Profile Modification for Multimesh Gear Vibration," *Journal of Mechanical Design*, vol. 130, pp. 121402–13, 2008.
- [4] H. Ma, X. Pang, R. Feng, and B. Wen, "Evaluation of optimum profile modification curves of profile shifted spur gears based on vibration responses," *Mechanical Systems and Signal Processing*, vol. 70–71, pp. 1131–1149, 3// 2016.
- [5] S. S. Ghosh and G. Chakraborty, "On optimal tooth profile modification for reduction of vibration and noise in spur gear pairs," *Mechanism and Machine Theory*, vol. 105, pp. 145–163, 11// 2016.
- [6] G. Bonori, M. Barbieri, and F. Pellicano, "Optimum profile modifications of spur gears by means of genetic algorithms," *Journal of Sound and Vibration*, vol. 313, pp. 603–616, 6/17/ 2008.
- [7] M. Faggioni, F. S. Samani, G. Bertacchi, and F. Pellicano, "Dynamic optimization of spur gears," *Mechanism and Machine Theory*, vol. 46, pp. 544–557, 4// 2011.
- [8] W. Xiao, J. Li, S. Wang, and X. Fang, "Study on vibration suppression based on particle damping in centrifugal field of gear transmission," *Journal of Sound and Vibration*, vol. 366, pp. 62–80, 3/31/ 2016.
- [9] W. Xiao, Y. Huang, H. Jiang, and L. Jin, "Effect of powder material on vibration reduction of gear system in centrifugal field," *Powder Technology*, vol. 294, pp. 146–158, 6// 2016.
- [10] D. W. Huang, Xie, Y.M., *Evolutionary topology optimization of continuum structures*. UK: John Wiley & Sons, 2010.
- [11] Y. M. Xie and G. P. Steven, "A simple evolutionary procedure for structural optimization," *Computers and Structures*, vol. 49, pp. 885–896, 1993.
- [12] M. P. Bendsøe, "Optimal shape design as a material distribution problem," *Structural Optimization*, vol. 1, pp. 193–202, 1989.
- [13] X. Y. Yang, Y. M. Xie, G. P. Steven, and O. M. Querin, "Bidirectional evolutionary method for stiffness optimization," *Aiaa Journal*, vol. 37, pp. 1483–1488, Nov 1999.
- [14] O. M. Querin, V. Young, G. P. Steven, and Y. M. Xie, "Computational efficiency and validation of bi-directional evolutionary structural optimization," *Computer Methods in Applied Mechanics and Engineering*, vol. 189, pp. 559–573, 2000.
- [15] X. Huang and Y. M. Xie, "Convergent and mesh-independent solutions for the bi-directional evolutionary structural optimization method," *Finite Elements in Analysis and Design*, vol. 43, pp. 1039–1049, 2007.
- [16] X. Huang, Y. M. Xie, and M. C. Burry, "A New Algorithm for Bi-Directional Evolutionary Structural Optimization," *JSME international journal. Series C, Mechanical systems, machine elements and manufacturing*, vol. 49, pp. 1091–1099, 12/15/ 2006.
- [17] C. Yan, L. Hao, A. Hussein, P. Young, J. Huang, and W. Zhu, "Microstructure and mechanical properties of aluminium alloy cellular lattice structures manufactured by direct metal laser sintering," *Materials Science and Engineering: A*, vol. 628, pp. 238–246, 3/25/

- 2015.
- [18] M. P. Bondsoe, Sigmund, O., *Topology optimization, theory, methods and applications*. Berling: Springer-Verlag, 2003.
 - [19] *Abaqus/CAE 6.14 User's guide*: Dassault Systèmes Corp., Providence, 2014.
 - [20] CAESS ProTOp Documentation [Online].

Energy Saving Novel Lubricants

DARKO LOVREC & VITO TIČ

Abstract The paper presents the latest findings linked to excellent lubrication properties of some ionic liquids, appropriate for use as a green lubricant within gear transmissions, hydraulic system, compressors etc. Their excellent features are presented on the basis of the results of various measurements and standard tests. In comparison to mineral based oils or synthetic lubricants, the results regarding friction and wear are more than 5 times better.

Keywords: • lubricants • ionic liquids • low friction • energy saving • novel lubricants •

CORRESPONDENCE ADDRESS: Darko Lovrec, Ph.D., Associate Professor, University of Maribor, Faculty of Mechanical Engineering, Smetanova ulica 17, 2000 Maribor, Slovenia, e-mail: darko.lovrec@um.si. Vito Tič, Ph.D., Assistant Professor, University of Maribor, Faculty of Mechanical Engineering, Smetanova ulica 17, 2000 Maribor, Slovenia, e-mail: vito.tic@um.si.

1 Introduction

The lubricants are today still selected in regard to their primary mission: to have appropriate lubricating properties, providing good corrosion protection and cooling of components and in case when used within hydraulic system, to transfer the power and signals.

When it comes to energy conservation this is not nearly enough. In view of today's growing pressure to reduce demand on non-renewable energy resources and increase operating profits, we are increasingly then ever looking for new types of lubricants that would not merely satisfy the mentioned basic needs, but would be fully consistent to *New Lubrication Commandments*: Conserve energy and protect the environment. The solution in this regard offers ionic liquids, as novel lubricants.

Ionic liquids (ILs) were first reported as very promising high-performance lubricants in 2001 and have attracted considerable attention within the field of tribology, due to their remarkable lubrication and anti-wear capabilities as compared to lubrication oils in general use.

Ionic liquids have many of good features as described in different literature. Therefore they should be the ideal candidates for new lubricants, suitable for use under harsh conditions, where conventional oils and greases or solid lubricants fail [1]. A large number of studies have already been carried out in this area so far but only a few with ionic liquids suitable for use within eg. hydraulic system.

The selection of cation and anion in an ionic liquid, as well as the design of ion side chains determine, the fundamental properties of ILs, which permits the creating of tailor-made lubricants and lubricant additives. [2] to [3]

2 Ionic Liquids as Lubricants

Ionic liquids are defined as molten salts with a melting temperature below 100 °C or lower. They are in the liquid state - so called "room temperature molten salts". Some characteristic properties: melting point ≤ 100 °C down to approx. -60 °C; mild chemical reactivity, low corrosion; virtually no vapour pressure; organic cations; weakly coordinating ions.

ILs are combinations of cations and anions and typically consists of an organic cation and an inorganic or organic anion. Ionic liquids with melting point at ambient temperature consist of extensive and asymmetrical organic cations, such as 1-alkyl-3-methylimidazolium, 1-alkyl pyridine, 1-methyl-1-alkyl pyrrolydine or ammonium salts. The anions used range from simple halides, reducing the high temperatures of the melting point, to inorganic anions such as tetrafluoroborates and hexafluorophosphates and to extensive organic anions such as bis(trifluorosulphony)amides, triflates or tosylates. [1]

However, when combined with certain specified cation and anion, you will obtain another salt – which if it does not work by trial and error but intentionally, can be synthesised into a completely new material with entirely new properties. In our case, we are looking for liquid salts, which would have the characteristics of a perfect lubricant.

However, the cations and anions present in ionic liquids are so formulated that the resulting salts hardly crystallise. Therefore the ionic liquid is liquid within a wide temperature range. An important feature of ionic liquids is the possibility of adapting these physical-chemical properties through changing the natures of the anions and cations – Figure 1.

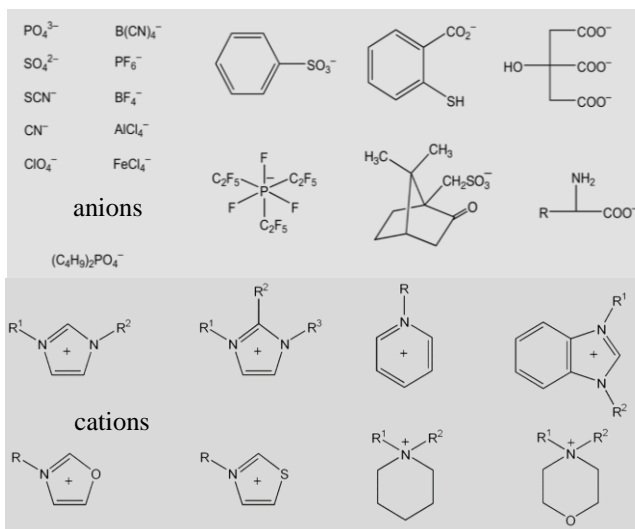


Figure 1. Typical ILs anions and cations

The number of possible combinations is extremely high, that is why the best ionic liquid is supposed to be adapted for different usage: $1 \cdot 10^{18}$ combinations. In our case, for the use as lubricant, in the forefront are following properties: good lubricity, low friction coefficient, high welding point, resistance to wear - small wear diameter, high viscosity index (a minor change the viscosity with temperature) ... and to be harmless to the environment.

3 Lubrication Properties Test

Most tribological systems include lubricant for reducing friction and wear. The easiest approach to presenting the quality of lubrication is to do it with the so-called Stribeck's curve (Figure 2), representing the friction coefficient depending on the Stribeck's parameter including viscosity, relative surface velocity, and loading.

Basically, the qualities of lubrications improve when moving along the horizontal axis of the Stribeck's curve to the right. The combination of low velocity, low viscosity and high

loading will cause the boundary lubrication characterised by a small quantity of lubricant in the space between the two surfaces and a greater surface of direct contact. On the Stribeck's curve it can be seen, that this is expressed by very high friction, which leads not only to increased wear caused by friction, but also to a greater consumption of energy (heat generation).

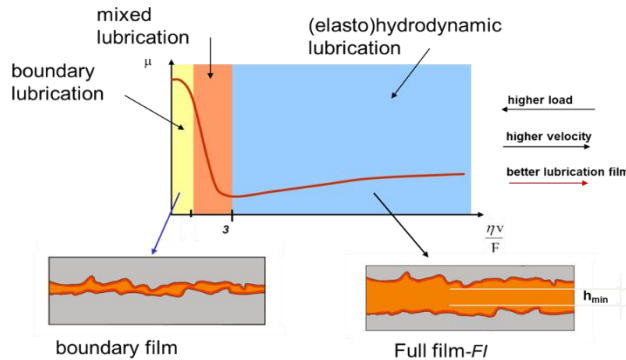


Figure 2. Stribeck's curve

The measurements of Stribeck's curve for the ILs, compared to classical mineral based oil, were performed on the MTM device (Mini Traction Machine). MTM is a device for measuring friction and lubricating film thickness with ball-disc configurations. A diagram of the device is shown in Figure 3.

The ball of 19.05 mm (3/4 inch) diameter with roughness $R_a < 0.02 \mu\text{m}$ and hardness 800HV-929HV under loading sits on a disc of 46 mm diameter with roughness $R_a < 0.01 \mu\text{m}$ and hardness 720 HV-780HV. Both are from the identical material DIN 100Cr6. The disc is completely dipped into the tested liquid the quantity of which amounts to about 35 ml. The ball and disc are driven independently of each other so that the test can be performed with different slide-to-roll ratios. The friction force between the ball and disc is measured by a force transducer.

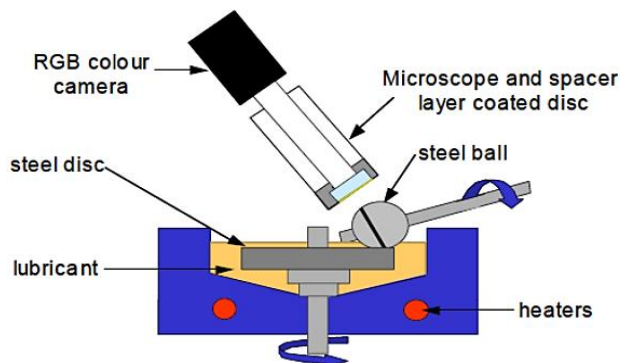


Figure 3. MTM device for measuring of Stribeck's curve

During the Stribeck test the velocity was changed with a constant slide-to-roll ratio. In 20 logarithmic decrements the velocity was reduced from 2 m/s to 0.01 m/s with a slide-to-roll ratio of 50 %. In that way, different lubrication modes were reached. The pressing force amounted to 35 N, giving the Hertzian contact pressure of 1 GPa with given ball and disc geometry.

The slide-to-roll ratio is defined by equation (1). For a specific ratio, the device during the measurement when once faster rotates the disc, the next time it rotates the ball faster.

$$SRR = \frac{U_{slid}}{U_{av}} = \frac{|U_{ball} - U_{pl}|}{(U_{ball} + U_{pl})/2} \cdot 100 \quad (1)$$

where U_{slid} [m/s] is the sliding velocity of ball and disc, U_{av} [m/s] is the average sliding velocity of the ball and disc, U_{ball} [m/s] is ball velocity and U_{pl} [m/s] is plate velocity.

Ionic liquid lubricating properties, especial for using as a hydraulic fluid or gear transmission lubricant, can be tested by the welding-point determination and wear test, according to standardised procedure (eg. IP 239-85). This method is based on load application to four standardised steel balls of 12.7 mm diameter. The top rotating ball slips onto the lower three fixed balls at constant loading and at constant rotating velocity of 1440 min⁻¹ (Figure 4). The welding- point measurement and the wear test of lubricating oils, emulsions and greases can be performed on the same apparatus.

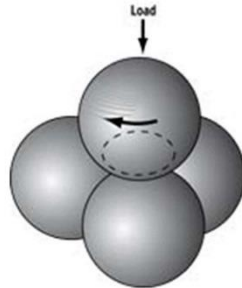


Figure 4. Principle of welding-point measurement

The welding-point is measured at specific loading and/or to ball pressure for 10 seconds. The top ball rotates and presses with the test loading against the lower three immovable balls dipped into the tested liquid. The measurement result is given in kg and comprises two numbers (eg. 140/160). The first number indicates the maximum loading at which ball welding did not occur during the test (10 s). The second number indicates the minimum loading at which complete steel ball welding and/or automatic deactivation of the device occurred during the test.

The wear test lasts much longer, namely for 60 min ±1 min at constant temperature and loading, depending on the tested liquid. The ball wear depends on the loading, velocity,

duration of the test and the properties of the lubricant tested. As all parameters, except the lubricating properties are constant, the result and/or the ball wear depends only on the lubricating properties of the liquid tested.

After completion of the test, the wear test result is obtained by measuring the wear of the lower three steel balls under a microscope, where the diameters of the wear cavities are measured on the three immovable balls. The wear extent is defined as the average diameter of ball wear under known conditions.

Welding-point determination and wear test were performed according to the standardised procedure IP 239-85.

4 Lubrication Properties of ils

The lubricating properties of some tested ionic liquid samples are considerably better than those of the classical mineral based oil. Figure 5 shows the comparison between the welding points and wear diameters for different samples of ionic liquids compared to mineral based oil ISO VG 46 (green).

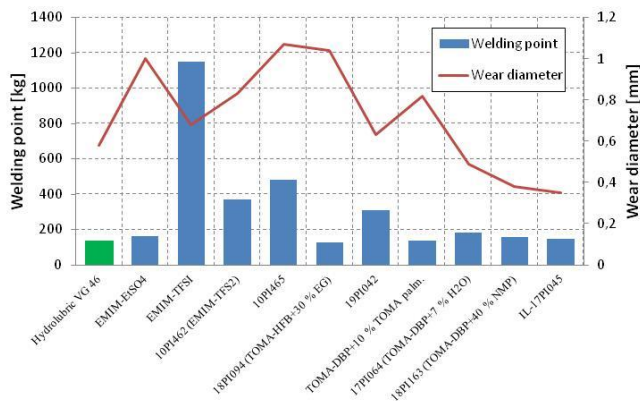


Figure 5. Ionic liquid lubrication properties in comparison with mineral based oil

Some samples had an exceptionally high welding point, for example EMIM-TFSI had as much as 1150 kg, which pointed out exceptional properties at extreme pressures but, interestingly, the wear diameter was even greater than that of the mineral oil, implying that the anti-wear properties were worse. As in the case of hydraulic oils the anti-wear properties are more important that liquid would be potentially more suitable for use in gearings, maybe even as metalworking fluid during metal machining. In regard to other liquids with high welding points the limitation was worse corrosive protection in the presence of moisture or in proper viscosity for the use in hydraulic systems.

The additional measurements of Stribeck's curve for the classical mineral based hydraulic oil Hydrolubric VG 46 and for the ionic liquids IL 17PI045 and EMIM-EtSO₄ were

performed. The measured Stribeck's curves for all three liquids at ambient temperature T_0 and 60 °C are shown in Figure 6.

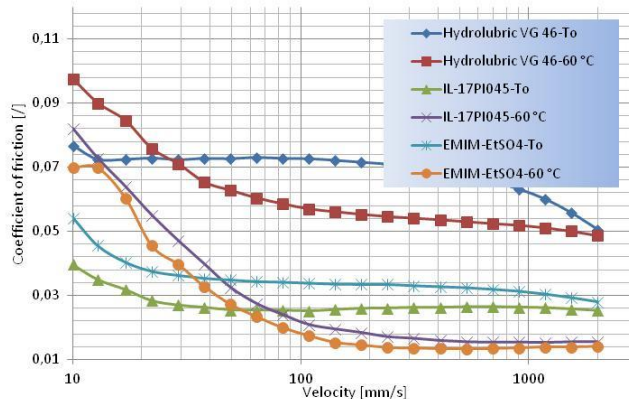


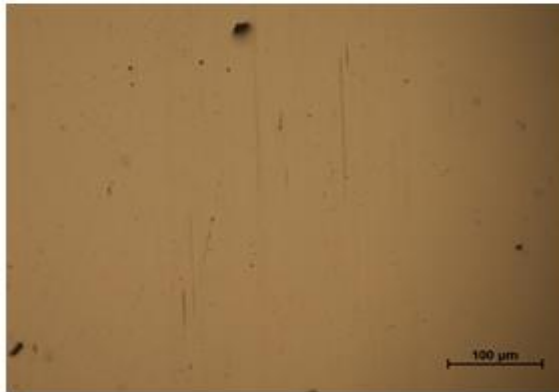
Figure 6. Measured Stribeck's curves

It can be seen that the friction coefficient of the mineral hydraulic oil within the entire range is considerably higher than that of both ionic liquids. The two ionic liquids have a very similar friction coefficient within the entire range, the IL-17PI045 having a slightly lower friction coefficient at room temperature and the EMIM-EtSO₄ at 60 °C (and therefore smaller wear and consequently energy consumption).

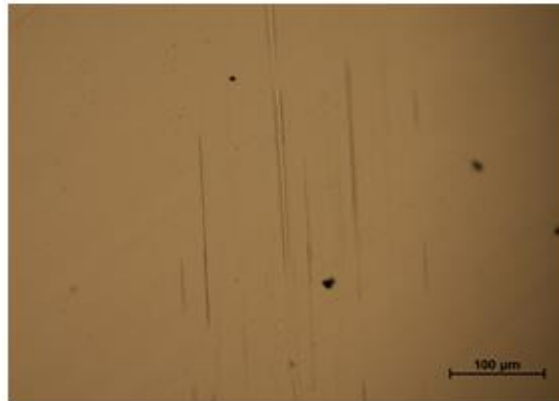
All three liquids showed much bigger differences between the lowest and highest measured values at 60 °C than at room temperature. Furthermore, at higher temperature the friction coefficient was higher within the range of boundary and mixed lubrications and lower within the range of elasto-hydrodynamic lubrication. That is probably caused by smaller lubricating film thickness at higher temperatures, resulting in more direct contacts of the ball and disc surfaces within the range of boundary and mixed lubrications.

After completion of Stribeck's curve measurements, photos of the disc surface were also taken. Detailed examination revealed that Hydrolubric VG 46 and IL-17PI045 showed more damaged surfaces after the Stribeck's curve measurements at 60 °C – a normal operating temperature of lubricant.

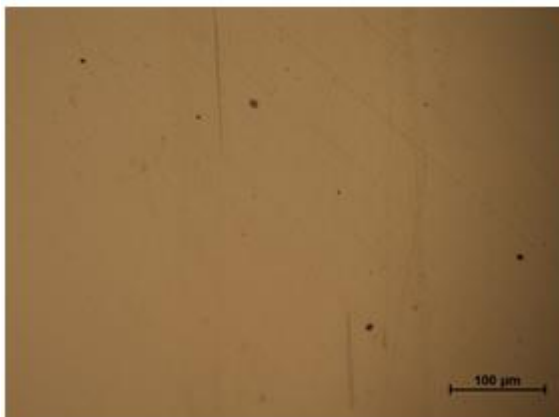
Figure 7 shows the comparisons between the discs' surfaces after completion the measurements of the Stribeck's curve for all three liquids at operating temperature. Pictures were taken by an optical microscope with 200-times magnification.



Hydrolubric VG 46; temperature: 60 °C



IL-17PI045; temperature: 60 °C



EMIM-EtSO4; temperature: 60 °C

Figure 7. Discs' surfaces after Stribeck's curve measurements

It can be concluded that, from the point of view of the friction coefficient, the lubricating properties of both ionic liquids were considerably better than those of the mineral hydraulic oil.

5 Other Requirements

In addition to the good lubricating properties, the ionic liquids as a medium appropriate for use in the gear transmissions and especially within high-pressure hydraulic systems must also have other good/excellent properties.

For a wide commercial use they must meet numerous special requirements, eg. harmless to human health, good thermal and chemical stabilities and low corrosiveness for the usually used materials of industrial components, low tendency to foaming... For use within high-pressure applications they additionally must feature low compressibility and adaptable solubility regarding gases. Chemical and thermal stability and non-flammability are the key requirements for liquids in processing devices in general and particularly in high-pressure hydraulic machines.

Further important parameter for the lubricants is a viscosity index - VI. The viscosity indexes of the more refined mineral oils on the market are about 100, while the multi-grade and synthetic oils have a higher viscosity index, ie. around 150. The ionic liquid viscosity indexes are, in general, much higher than those of mineral oils – see Table 1.

Table 1. Viscosity index and lubricating properties of ILs

Sample	Viscosity index ASTM D 2270	Welding point [kg]	Wear diameter [mm]
Mineral oil VG 46	119	130/140	0.58
EMIM-EtSO ₄	168	140/180	1,0
EMIM-TFSI	132	1100/1200	0.68
19PI042	116	300/320	0.63
17PI064	105	180/190	0.49
18PI163	155	150/160	0.38
IL-17PI045	155	140/150	0.35

Many machines use a common lubricant across numerous frictional zones and have varying loads, speeds and temperatures. Outdoor mobile equipment typically works under these challenging conditions. For such machines and operating conditions, the uses of a high viscosity index of lubricant definitely a huge advantage.

Synthetic lubricants with high VI, can help operators in many industries protect their equipment from a wide range of operating environments and conditions. Using high VI lubricants, which is characteristic for ionic liquids, can deliver superior equipment protection across a wider operating temperature range as in case of conventional, mineral-based lubricants that have a lower VI. In this way, there are helping to improve equipment reliability and performance to advance plant productivity.

If a lubricant's viscosity is too low, the lubricant will not be able to keep moving parts separated. This may lead to problems such as increased friction and wear, as well as increased heat and oxidation – and consequently to increased energy consumption.

If viscosity is too high, the lubricant won't flow adequately. This can lead to increased drag and friction, and in turn higher operating temperatures and energy consumption as well.

6 Conclusion

In modern tribological (eg. hydraulic) systems the lubricating properties are very important due to increasing pressures, as they guarantee long useful lifetimes of used components. Some ionic liquids proved to have excellent lubricating properties at high pressures. By measuring the welding point and the wear diameter on a four-ball apparatus and the friction coefficient (Stribeck's curve) it was discovered that the ionic liquids eg. IL-17PI045 and EMIM-EtSO₄ had much better lubricating properties than the classical mineral based oil. Consequently the wear and the energy consumption are lower.

The IL-17PI045 had the more properties within the range of the mineral hydraulic oil, namely viscosity, viscosity index, corrosion properties, good foaming properties and compatibility with hydraulic system components (not presented in this paper), lubricating properties (higher welding point and smaller wear diameter than in the case of mineral oil).

References

- [1] M. Kambič, and R. Kalb, "Comparison of ionic liquids with conventional mineral oils"; International Fluid Power conference 2013, proceedings; Maribor; pp 61-70, 2013.
- [2] A. S. Pensado, M. J. P. Comunas, and J. Fernandez, "The pressure-viscosity coefficient of several ionic liquids", *Tribology Letters*, vol. 31, no. 2, pp 107-118, 2008.
- [3] Z. Feng., L. Yongmin, and L. Weimin, "Ionic liquid lubricants: designed chemistry for engineering applications", *Chemical Society Reviews*, vol. 9, no. 38, pp 2590-2599, 2009.
- [4] K. Yuriko, Y. Sotaro, K. Takahiro, T. Ryo, and S. Sasaki, "Lubricity and corrosiveness of ionic liquids for steel-on steel sliding contacts", *Journal of Engineering Tribology*, vol. 226, no. 11, pp 991-1006, 2012.
- [5] J. Dong, H. Litian, and F. Dapeng, "Crown-type ionic liquids as lubricants for steel-on-steel system", *Tribology Letters*, vol. 41, no. 2, pp 417-424.

- [6] Z. Liu, F. Dapeng, and X. Bin, “Tribological characteristics of alkyylimidazolium diethyl phosphates ionic liquids as lubricants for steel-steel contact” *Tribology Letters*, vol. 34, no. 2, pp 95-101, 2009.
- [7] A. Somers, P. Howlet, J. Sun, D. MacFarlane, and M. Forsyth, “Transition in wear performance for ionic liquid lubricants under increasing load”, *Tribology Letters*, vol. 40, no. 2, page 279-284, 2010.
- [8] V. Totolin, I. Minami, C. Gabler, and N. Doerr, “Halogen-free borate ionic liquids as novel lubricants for tribological applications”, *Tribology International*, vol. 67, no. 11, pp 191-198, 2013.
- [9] L. Zhu, L. Chen, S. Xiang, G. Chen, and X. Yang Xin, “Tribological properties of functionalized ionic liquids containing ester-group as lubricants for steel-steel system”, *China Petroleum Processing and Petrochemical Technology*, vol. 14, no. 2, pp 60-65, 2012.
- [10] D. Li, M. Cai, D. Feng, F. Zhou, and W. Liu, “Excellent lubrication performance and superior corrosion resistance of vinyl functionalized ionic liquid lubricants at elevated temperature” *Tribology International*, vol. 44, no. 10, pp 1111-1117, 2011.



 **energetika** *ljubljana*



 **energetika** *ljubljana*



 **energetika** *ljubljana*



 **energetika** *ljubljana*



 **energetika** *ljubljana*



 **energetika** *ljubljana*



 **energetika** *ljubljana*



 **energetika** *ljubljana*



 **energetika** *ljubljana*



 **energetika** *ljubljana*